Application of PEPT to track a single labelled red blood cell in vitro

by

Ching-Wang Chou

A thesis submitted for
the degree of Master of Philosophy

Nuclear Physics Group
School of Physics and Astronomy
University of Birmingham

Abstract

Positron Emission Particle Tracking (PEPT) was invented and developed at Birmingham. This technique is a variant of the medical imaging technique of positron emission tomography (PET). The tracking technique enables a single positron-emitting tracer particle to be tracked accurately inside an opaque vessel, which is within the field of view of the PET camera. The basis of PEPT is to detect coincidentally a pair of opposite annihilation photons. This will define a line on which the annihilation is assumed to occur. The tracer moving at 1 m/s can be located to within 0.5 mm 250 times per second in 3D by triangulation of a number of detected annihilation events. PEPT has proved to be a very powerful tool for studying the fundamental physics of particulate systems or systems of industrial interest. Apart from these applications, we explored the possibility that PEPT could also be applied to the tracking of a red blood cell.

As the progress of this feasibility study remained only at the preliminary stage, this thesis seeks to describe the main factors which would be involved in producing the ^{11}CO gas and labelling the red blood cells. Some preliminary results and figures are also revealed. Using the Birmingham MC40 cyclotron, we produced ^{11}C ($t_{1/2}$=20.385 mins) and acquired ^{11}CO gas through the chemical processing system. This ^{11}CO gas was used as the positron emission source which combined with the red blood cells. Red blood cells have a high affinity for CO. In the human body, when CO is absorbed by a red blood cell, it combines with the oxygen carrying haemoglobin to form carboxyhaemoglobin. There are approximately $200\sim300\times10^6$ haemoglobin molecules in a single red blood cell. Ideally, if all the oxygen positions in a red blood cell could be replaced by ^{11}CO, enough activity might be achieved for the purpose of tracking. In fact, we found that the possibility of tracking a single labelled red cell in vitro is low, due to the low specific activity of produced ^{11}CO and the poor labelling technique. However using the PEPT technique, with some adjustments of energy windows and the distance of the detectors, a tracer with an activity much less than 0.15 μCi should be still possible to be tracked despite the maximum velocity of the tracer one can usefully track at is much lower.

Acknowledgements

I began a PhD study in April 2002. Due to the influence of the building of the MC40 cyclotron from 2002 to 2004 at Birmingham, this study was delayed. I had leave of absence from June 2005 to 1st January 2006. I chose also to change my student registration status from PhD to MPhil on 1st January 2006. Although the progress of this feasibility study remained only at the preliminary stage, Dr. David Parker, my supervisor, and I had reached some preliminary results in producing the ^{11}CO gas by using the newly built MC40 cyclotron. A preliminary imaging for the labelled red cells had also been achieved by using the ADAC Forte PET camera.

The completion of this thesis has depended on the contributions of many people, to all of whom I owe a great deal of gratitude. Firstly, I would like to thank Dr. Parker for his guidance in this feasibility study and for his corrections to this thesis. Throughout my PhD and MPhil study, I have relied greatly on his guidance; without his enthusiasm and tuition, I cannot imagine that this thesis could have been completed.

Secondly, I would like to thank my family in Taiwan. Without their love and support, I cannot imagine that I should have gone so far. Thirdly, I very much appreciate the help I have received from the Nuclear Physics group. I am indebted to Mrs. Tina Campbell, Mr. Michael D. Smith, Dr. Garry Tungate and Dr. Victor A. Ziman for their assistances in experimental and administrative work. I would like to acknowledge the other postgraduate students in this research group – Paul, John, Leon, Bradley, Matthew, Anthony, Mark and Dave, who all have made the various conferences and lunch hours so enjoyable. I really want to thank them for standing by me in good and bad times.

Finally as a Christian, I would like to praise the Lord who presents me with a pattern of life and fosters me so that I can grow in life. I hope that this feasibility study will be of benefit to someone who is also interested in this issue. May God bless we all.

~Ching-Wang Chou

Contents

1 Introduction to PEPT 1

2 Production of ^{11}CO 19

3 Labelling red blood cells (RBCs) with ^{11}CO 44

4 Ideas related to tracking a single labelled RBC, discussion and suggestions for future work 62

List of Figures

List of Tables

Chapter 1

Introduction to PEPT

"Positron Emission Particle Tracking" (PEPT) was invented and developed at Birmingham. This technique is a variant of the medical technique of positron emission tomography (PET). It enables a single positron-emitting tracer particle to be tracked accurately inside a system of interest. The basis of PEPT is to detect coincidentally a pair of nearly opposite annihilation photons using a pair of photon sensitive detectors. This pair of annihilation photons will define a line somewhere on which the annihilation is assumed to occur. The tracer location can be determined in 3D many times per second by triangulation of a number of detected annihilation events. A sophisticated PET camera for following the tracer motion by detecting coincidental gamma-rays is commercially available. In the Birmingham Positron Imaging Centre, an ADAC Forte PET camera and related techniques are being used to study physical and industrial issues. PEPT has proved to be a very powerful tool for studying the behaviour of granular materials in mixers and fluidized beds or for studying viscous fluids.

1.1 Positron emission

The positron is emitted by the radioisotope and travels several millimeters to final thermal equilibrium with its surroundings. When this positron is essentially at rest, it will annihilate with an electron nearby and two 511 keV back-to-back γ-rays at nearly 180° apart ($<0.3°$) are then emitted. See Figure 1.1 below.

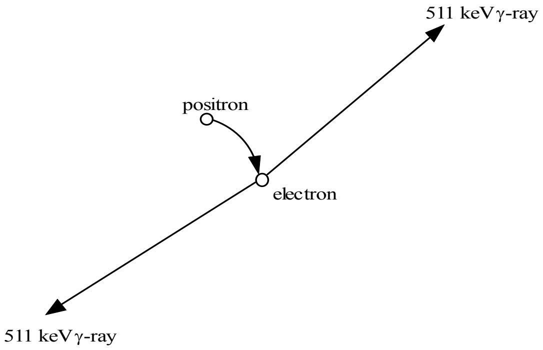

Figure 1.1: Positron annihilation

Positron emission decay (β^+) commonly occurs among proton-rich nuclides, which are more often lighter nuclides than heavier ones. ^{11}C, ^{13}N, ^{15}O, ^{18}F, ^{22}Na are all positron-emitting nuclides. The general formulae for β^+ decay are shown below (1.1, 1.2). An orbital electron is lost in forming the neutral daughter atom *D* in the decay of a positron emitter. In the formula (1.1), *Z* is the atomic number, e^+ is the positron and *v* is the neutrino. The mass number *A* of the daughter nuclide *D* remains the same as the parent nuclide *P* after this reaction (1.1). In the formula (1.2), *p* is the proton and *n* is the neutron. The first formula (1.1) could be simplified to the second formula (1.2), which is basically equivalent to the first one.

$${}^{A}_{Z}P \rightarrow {}^{A}_{Z-1}D + e^{+} + \nu \qquad (1.1)$$

$$p \rightarrow n + e^{+} + \nu \qquad (1.2)$$

In the decay of a positron emitter, one proton in the nucleus is converted into a neutron, a positron and a neutrino. The proton decay can only occur in the nucleus because for a free proton it would violate the conservation of energy by about 0.5 MeV. In contrast, a free neutron could decay into a proton, an electron and an antineutrino and this reaction is an exothermic process with energy release about 0.5 MeV. Since the proton is positively charged, the electric charge is conserved in the reaction of positron emission. The neutrino has no charge and may be zero mass. For the proton-rich isotope to emit β^+, it must have more protons than neutrons, such that the nucleus would be more stable if a proton changed into a neutron, where "more stable" means that the bonding energy is increased by more than 0.5 MeV. Normally, nuclei are more stable with roughly equal numbers of protons and neutrons due to the symmetry of the strong force holding the nucleus together. For higher Z nuclei, the increasing number of protons adds electric forces which repel and make the nuclei less stable. There is a precise calculation for the energy release Q of a positron emitter below. For the decay reaction among the positron emitters to occur, the mass of the parent atom must be greater than that of the daughter by at least $2m_ec^2$=1.022 MeV, namely Q must be positive.

$$M(A,Z)c^2 = M_Pc^2 + Zm_ec^2 - \sum_{i=1}^{z} B_i \ , \ B_i = \text{electron bonding energy} \tag{1.3}$$

$$M(A,Z-1)c^2 = M_Dc^2 + (Z-1)m_ec^2 - \sum_{i=1}^{z-1} B_i \tag{1.4}$$

$$Q \equiv (M_P - M_D - m_e - m_\nu)c^2 \equiv M(A,Z)c^2 - M(A,Z-1)c^2 - 2m_ec^2 - (m_\nu c^2 - \sum_{i=1}^{z} B_i + \sum_{i=1}^{z-1} B_i) \tag{1.5}$$

$$Q \cong M(A,Z)c^2 - M(A,Z-1)c^2 - 2m_ec^2 \ \text{(ignore the later 3 terms)} \tag{1.6}$$

In the above formulae (1.3~1.6), M_P and M_D represent the mass of parent and daughter nuclei while *M(A,Z)* and *M(A,Z-1)* represent the mass of parent and daughter atoms. *A* is the mass number, *Z* is the atomic number, *c* is the speed of light in vacuum, m_e is the rest mass of electron and m_ν is the rest mass of neutrino. In the last formula (1.6), the small difference in the atomic bonding energies for electrons and the mass of neutrino (neutrino may be massless) has been neglected. The emitted positron slows down to thermal energies in a few pico-seconds in a condensed medium and travels up to 1 millimeter. In a very dense medium, this range may be smaller.

The β^+ energy spectrum is continuous as is that for β^- decay. Figure 1.2 below shows the β^+ energy spectrum distribution. At the end of the spectrum, there is a maximum energy, E_{max}, which corresponds to the maximum kinetic energy given to the positron. As we know, there are three final products in the β^+ decay, the daughter nucleus, the positron and the neutrino. In the limit as the energy and momentum given to the neutrino approach zero, the positron has a maximum kinetic energy corrected by the energy imparted to the daughter nucleus. The end point energy also represents exactly the Q value for this decay reaction. The average positron energy is somewhat larger than one-third of E_{max}.

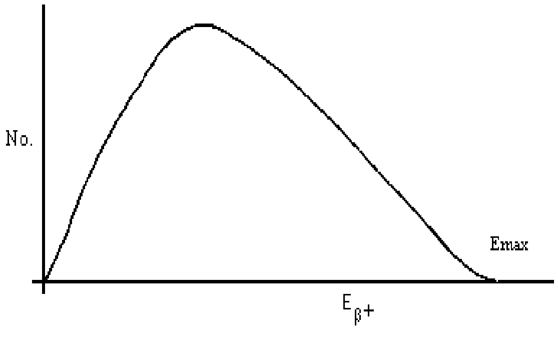

Figure 1.2: The energy spectrum of positron emission

Table 1.1 below describes the major physical characteristics for four major positron emitters used frequently in radiation imaging. As can be seen from Table 1.1, the emission rates of positrons for these four isotopes are not all 100% as electron capture (EC) competes with positron emission. However, for ^{11}C, ^{13}N and ^{15}O, their positron emission rates are nearly equal to 100%. For the isotope ^{11}C, positron emission occurs 99+% of the time and the EC occurs 0.2% of the time. An example of the positron emission decay scheme of ^{22}Na can be seen below (Figure 1.3). Its positron emission occurs 89.8% of the time and EC occurs 10.2% of the time. Either positron emission or EC leaves the ^{22}Na daughter nucleus in an excited state with a gamma-ray energy of 1.275 MeV.

Nuclide	Production reaction	Half-life(minute)	Decay mode	Max energy(MeV)
^{18}F	^{18}O(p,n)^{18}F	109.7	β^+ (97%)	0.635
^{15}O	^{14}N(d,n)^{15}O	2.07	β^+ (99.9%)	1.72
^{13}N	^{16}O(p,α)^{13}N	9.96	β^+ (99.9%)	1.19
^{11}C	^{14}N(p,α)^{11}C	20.39	β^+ (99+%)	0.96

Table 1.1: Positron emitters. Data from [Wah02]

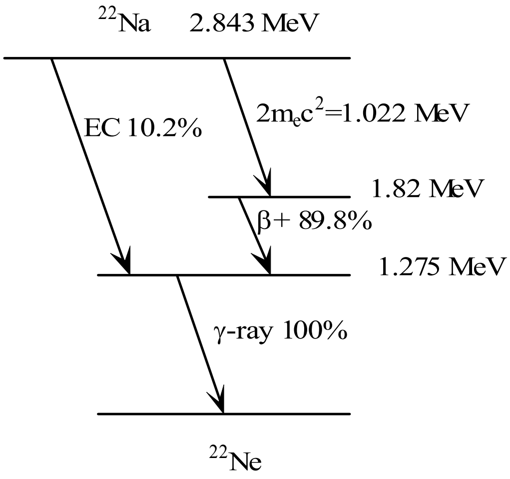

Figure 1.3: ^{22}Na decay mode

1.1.1 Positronium

Positronium (Ps) represents a bound state between a positron and an electron, which could be treated formally as a hydrogen atom. This bound state is electrically neutral and its centre of mass is midway between the constituent positron and electron (their masses are equal and are opposite in charge with the same quantity). In the Bohr model, the energy formula of a hydrogen atom is as shown below (1.7).

$$E = \frac{-R_\infty hcz^2}{n^2} \tag{1.7}$$

where E is the ionization energy, R_∞ is the infinity Rydberg constant, h is the Planck constant, c is the speed of light in vacuum, z is the atomic number (=1), n is the energy level. In a state of positronium, the R_∞ must be replaced by $\mu R_\infty / m_e$ in which μ is the reduced mass (=m_e/2). So the energy formula for $E_{positronium}$ is as shown below (1.8). The ionization energy of a hydrogen atom is 13.6 eV. For a positronium, it is 6.8 eV, which is just half of 13.6 eV.

$$E = \frac{-R_\infty hcz^2}{2n^2} \tag{1.8}$$

The reciprocal wavelengths λ of the emitted spectral lines are as shown below (1.9). Compared to the hydrogen atom, the frequencies f of the emitted lines would be half and the wavelengths double. In the formula (1.9), the z value for the positronium is equal to 1, n_f is the final energy level and n_i is the initial energy level.

$$\frac{1}{\lambda} = \frac{f}{c} = \frac{R_\infty z^2}{2}\left(\frac{1}{n_f^2} - \frac{1}{n_i^2}\right) \tag{1.9}$$

For the distance D between the electron and the nucleus (proton) in a hydrogen atom, a formula (1.10) can be seen below.

$$D = \frac{4\pi\varepsilon_o n^2 \hbar^2}{m_e z e^2} \tag{1.10}$$

where ε_o is the permittivity of free space, n is the energy level, $\hbar$ is the reduced Planck constant, m_e is the rest mass of the electron, z is the atomic number(=1), e is the elementary charge. In a positronium atom, the mass of electron in the distance formula (1.10) should be replaced with the reduced mass (=m_e/2). This means that at any quantum state n, the distance in a positronium is always twice the distance in a hydrogen atom (1.11). In a hydrogen atom, the smallest orbit is 0.529 Å. For the ground state, the separation of a positronium is close to 1 Å.

$$D_{positronium} = 2D_{hydrogen} \tag{1.11}$$

From the above description of a positronium, it can be easily explained from Bohr's model of the hydrogen atom. If we apply Schrödinger equation to this bound state, it can be solved similarly. The Schrödinger equation for a positronium is identical to that for hydrogen, where the reduced mass of the hydrogen atom is replaced by one half of the electron mass. The eigenvalue equation for the center of mass of Ps can be solved. The eigenvalues are very close to half of those of hydrogen. An eigenfunction solved from a Schrödinger time-independent equation using spherical polar coordinates is given below (1.12).

$$\psi = R_{nl}(r)\ \vartheta_{lm_l}(\theta)\ \phi_{m_l}(\varphi) \tag{1.12}$$

where ψ is the eigenfunction, n is the principal quantum number, l is the orbital quantum number, m_l is the magnetic quantum number and r, θ, φ are the three spatial variables. The principal quantum number n dominates the quantization of energy and its value is exactly the same as the energy formula from Bohr's model of a hydrogen atom.

1.1.2 Annihilation angle

At the instant of annihilation, the momentum of the positron is nearly zero. The most plausible image of the annihilation of a positron-electron pair is the appearance of two nearly opposite photons. Because of the existence of the electron's momentum, the two opposite photons cannot locate on the same straight line. They have a slight deviation of angle.

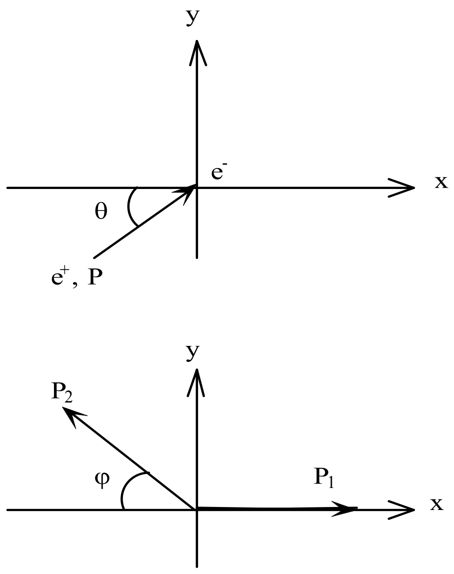

Figure 1.4: Pair annihilation

By the conservation of energy and momentum, several formulae can be built according to Figure 1.4. First of all, one could assume that an electron stays at the origin of the coordinates. A positron with momentum P is incident on the electron. Compared to the potential and kinetic energies, the rest mass energy $m_e c^2$ is much larger. Thereby the potential and kinetic energies can be ignored. Three formulae of energy and momentum conservation are shown below (1.13~1.15).

$$2m_e c^2 = cP_1 + cP_2 \tag{1.13}$$

$$P\sin\theta = P_2 \sin\varphi \tag{1.14}$$

$$P\cos\theta = P_1 - P_2 \cos\varphi \tag{1.15}$$

where m_e is the rest mass of the electron (and the positron), c is the speed of light in vacuum, P_1 and P_2 are the momenta of the annihilation photons, θ is the incident angle of the positron and φ is the annihilation angle. One can solve for P_1 and P_2 from (1.14), (1.15) and insert P_1 and P_2 into the equation of energy conservation (1.13). A formula (1.16) relating the angles θ, φ and the mass and momentum of the positron can be found below.

$$2m_e c = \frac{P(\sin\theta\cos\varphi + \sin\theta + \cos\theta\sin\varphi)}{\sin\varphi} \tag{1.16}$$

Some approximations can be made in the above equation. First of all, φ is a very small angle, usually near 0.001 radian (0.06 degree). Thereby the value of $\cos\varphi$ could be nearly equal to 1. The value of $\sin\varphi$ is nearly equal to φ by radian. The last term $\cos\theta\sin\varphi$ is much smaller than the other two terms and could be neglected. After processing these approximations, the formula (1.17) below can be obtained to describe the relationship between the annihilation angle φ and the positron's incident angle θ. Using this deduced formula, the annihilation angle φ could be estimated.

$$\varphi = \frac{P\sin\theta}{m_e c} \tag{1.17}$$

A theoretical result can be found from Table 1.2. If the incident angle of the positron is defined as 30°, sin30° is equal to 0.5. Normally in the solid, the positron's momentum P is much smaller than m_ec. Thereby the individual ratio of momentum of a positron to m_ec could be chosen as 0.01, 0.001, 0.0001, 0.00001. Based on the above assumptions, the annihilation angle φ could be estimated. This theoretically deduced result is consistent with the common experimental result that the annihilation angle is normally less than 0.3°.

P/m_ec	φ in radian	φ in degree
0.01	0.005	0.286
0.001	0.0005	0.0286
0.0001	0.00005	0.00286
0.00001	0.000005	0.000286

Table 1.2: Values of the annihilation angle

1.1.3 Annihilation photons

Positron annihilation will include the formation of annihilation photons. How many annihilation photons will occur depends on the spin orientations (spin angular momentum) of the bound state (positron-electron pair). The positronium could exist in the two spin states, S=0, 1. For S=0, the bound state is in the singlet state, in which the spins for the electron and positron are anti-parallel and this bound state is named the para-positronium. For S=1, the bound state is in the triplet state in which the spins for the electron and positron are parallel and this bound state is named the ortho-positronium. The lifetime for the singlet para-positronium is 10^{-10} second, while for the triplet ortho-positronium it is 10^{-7} second. The number of photons emitted must be even for the singlet state and odd for the triplet state, because of the requirements of parity conservation. The need to conserve angular momentum and to impose CP invariance leads to a selection rule below created by Wolfenstein and Ravenhall in 1952 [Wol52].

$$(-1)^{n_\gamma} = (-1)^{L+S} \tag{1.18}$$

The above formula (1.18) shows that a positronium in a state with spin S and orbital angular momentum L may only annihilate into n_γ gamma-rays. For a free positronium, a single gamma-ray annihilation and a radiationless annihilation are forbidden, using the above selection rule. In practice, most ortho-positronium states will convert to para-positronium and decay by two photon emissions. This phenomenon has been found in solid state physics and is expected from their individual lifetimes.

1.2 Description of PEPT

PEPT is a particularly valuable technique for studying motion within a closed, circulating system in which the tracer particle can explore all possible types of motion. In nuclear medicine, PET is used to assess metabolic activity in different parts of the body and produces cross-sectional images of the body. Instead of attempting to image the distribution of a fluid tracer as in PET, in PEPT a single tracer particle is introduced into the system of interest and can be tracked as it moves between the two detectors of an ADAC Forte positron camera (the one used in the present research). Each detector can determine interaction coordinates to within a few millimeters from the incident gamma-rays. Only simultaneously detected events are recorded in both detectors. The tracer position can be decided by triangulation from a small number of coincident events. The basis of PEPT is to collect coincident events and the resulting coincidence events are recorded event-by-event on computer, allowing subsequent reconstruction. Figure 1.5 below describes schematically the principle of tracer location in PEPT.

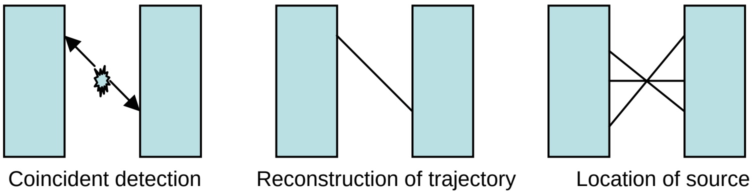

Figure 1.5: Principle of tracer location in PEPT

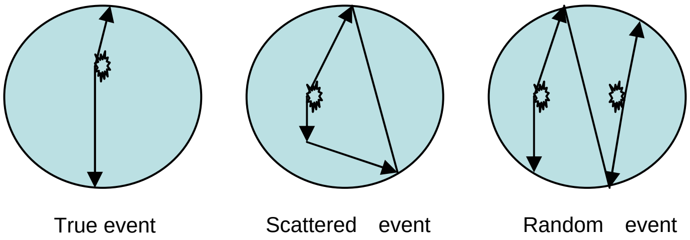

Figure 1.6: True, scattered and random events

But not all events are useful for tracking. Only true events are needed. Within a specified resolving time *t* of each other, pulses are considered to be coincident in two detectors. Because of this finite resolving time, two independent pulses may produce a random event. A gamma-ray may be scattered before detection and consequently arrive at the detector. This will result in a wrong scattered event on the computer. The figure above (Figure 1.6) describes schematically a true event, a scattered event and a random event. In addition, some positron-emitting radionuclides (e.g. ^{22}Na, ^{124}I) emit gamma-rays to give the associated gamma-ray coincidence with an annihilation photon or another associated gamma-ray. The purpose of the PEPT algorithm is to reject the background due to these scattered, random and associated coincident events.

1.2.1 PEPT algorithm

The PEPT iterative algorithm has been developed at Birmingham since 1987 by Dr. David Parker et al. [Par93]. The proceeding of the PEPT algorithm is as follows. *N* detected coincidence events are given as an initial sample. There will exist a point coordinate closest to which all the paths of their gamma-rays pass. Once the closest point is determined, then those paths furthest from it will be discarded as corrupt. This process will be iterated for the remaining paths until only a fraction *f* of original events remains. *f* is the fraction of events finally used by the PEPT algorithm and has a specified value which depends on the amount of scattering material present and varies across the field of view. For each iteration, the discarded events are those whose distances are larger than a comparison value $k \times \overline{d}$. The formula below (1.19) describes the relationship between the discarded events and the comparison value $k \times \overline{d}$ for each iteration.

$$d_i \geq k \times \overline{d} \tag{1.19}$$

where $\overline{d}$ is the mean distance for all remaining events, *k* is usually equal to a constant 1.2 and d_i is the distance to each event from the minimum distance point coordinate on each iteration. The formula (1.20) in which $\overline{d}$ is an average distance for the initial *N* events is shown below.

$$\overline{d} = \frac{d_{i1} + d_{i2} + \ldots\ldots d_{iN}}{N} \tag{1.20}$$

Those paths which are larger than $k \times \bar{d}$ will be discarded. The minimum distance point coordinate and $\bar{d}$ will be renewed on each iteration. This is a dynamic process for determining the minimum distance point coordinate, discarding those furthest points from it on each iteration and will end by retaining a specified fraction *f.*

1.2.2 Precision of location

There are two important factors which limit the precision with which the location of the decaying tracer can be determined and therefore limit the spatial resolution: (1) The distance the positron travels before it annihilates is known as the positron range; (2) The electron and positron are not completely at rest when they annihilate. This fact results in the two annihilation photons being emitted back-to-back with a slight deviation angle, and this eventually results in a small positioning error, which depends on the separation of the detectors of ADAC Forte PET camera. For a common PET camera with a detector separation of 80 cm the error is normally about 2 mm. In practice, the spatial resolution of a PET imaging system is usually poorer than this, for the above reasons and the detector effects. There is an exaggerated schematic below (Figure 1.7) to describe the effect of the positron range and the small annihilation deviation angle on the location of the decaying tracer.

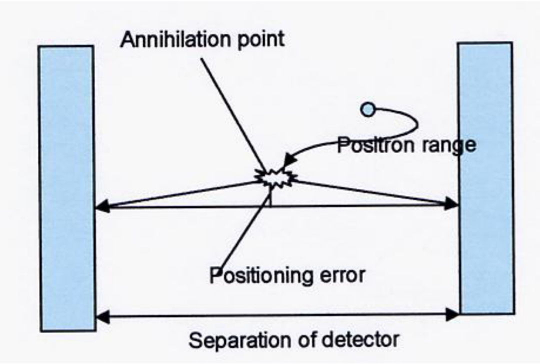

Figure 1.7: An exaggerated schematic of positron range and positioning error

For the precise location of a slow moving tracer (or a stationary tracer) in PEPT, we could locate it within the value Δ for every location given by the formula below (1.21) where N is the initial sample of detected coincidence events, *f* is the fraction of events finally used by PEPT algorithm and σ_{PSF} is the standard deviation of the camera's point-spread function (approximately 5 mm). A stationary tracer can be located with arbitrary precision by taking a sufficiently large sample *N* of events.

$$\Delta \approx \frac{\sigma_{PSF}}{\sqrt{fN}} \tag{1.21}$$

In the case of a fast moving tracer, during the measurement period, the tracer has moved a significant distance. The optimum number of events per location can be found from the formula below (1.23) where *R* is the data rate and *v* is the tracer's velocity. This optimum number *N* is large enough to give adequate precision but not large enough to let the tracer move too far during location process. To deduce the formula (1.23), one can consider that when Δ～distance is covered in a short time *dt*, an optimum number of events per location can be reached. Thereby one can build the following mathematical relation (1.22):

$$\frac{\sigma}{\sqrt{fRdt}} \approx vdt \tag{1.22}$$

where $Rdt=N$. Through the re-arrangement of this relation, one can reach the formula (1.23) below.

$$N^{\frac{3}{2}} \approx \frac{\sigma R}{v\sqrt{f}} \tag{1.23}$$

For the reasonable location of a fast moving tracer, one can require fN to be at least 5 events in practice. If one sets $N=b/f$ and inserts this relation into formula (1.23), one can reach a formula $v \sim (\sigma fR)/b^{3/2}$. Normally under the current PEPT technique, one can insert the values $b \sim 5$, $\sigma \sim 5$ mm, $R \sim 10^5$ s^{-1}, $f \sim 0.3$ into this formula and find the velocity～16 m/s which is the maximum velocity using at least 5 location events. Therefore, given a data rate R, there will be a maximum velocity one can usefully track at.

1.2.3 Requirements of tracer

The maximum coincidence rate R for the Forte is approximately 100k events per second. For a bare central point source ^{18}F and a detector separation of 600 mm, this count rate is produced by an activity of approximately 300 μCi [Par02]. If the source is surrounded by attenuating material, to achieve the same count rate, it requires higher activity and normally the maximum activity used under the practical condition is 1000 μCi. In general, a tracer with activity in the range of 300~1000 μCi could reach the optimum tracking using the current ADAC Forte PET camera and the PEPT technique. If an even higher activity is used, the data set will become dominated by random coincidences between unrelated pulses from the two detectors, as each of them is operating at a very high individual count rate (＞2M cps) [Par02].

There are currently three main labelling techniques for producing the tracer. Direct bombardment is used to bombard a glass bead which is larger than 1000 μm. Using the technique of direct bombardment, if the size of the glass bead is less than 1000 μm, the activity achieved will be too low and it could not be used as a proper tracer. For a tracer size smaller than 1000 μm, the ion exchange technique is used to exchange the counter-ions of the resin bead in a ^{18}F ion solution. For an even smaller tracer, a technique called surface adsorption is developing well [Fan06]. Using PEPT technique to do the tracking, normally there are two general requirements for the tracer: (1) The tracer is required to act as an inert flow tracer which is unreactive with fluids; (2) The half-life of the isotope used to label the tracer particle is long enough to complete the tracking.

1.3 Birmingham Positron Camera

A positron camera is used to observe the history of a tracer particle or a fluid tracer. There are two major goals in the design of a PET camera: (1) To detect as many of the emitted photon pairs as possible to achieve a high signal-to-noise ratio which is proportional to the square root of the number of events that contribute to the image, whereby the quality of the PET scan could be improved as the number of detected events has been increased. This quality performance therefore depends on the radioactivity of the tracer, the imaging time and the sensitivity of the scanner; and (2) To localize photon interactions in the detectors as accurately as possible. This determines the spatial resolution, or sharpness, of the images. There are three main weaknesses when a PET camera is used to undertake the imaging. (1) Typically only 1% of the total events emitted isotropically from the source are used in the reconstruction; (2) Typically 30% to 40% of detected events are accidental or false coincidences; and (3) Spatial resolution is limited by a number of factors.

In the Birmingham Positron Imaging Centre, our ADAC Forte PET camera is applied to 3D tomography, 2D projection imaging (PEPI) and single particle tracking (PEPT). When the two detectors are kept stationary, a single 2D projection of the distribution of a positron-emitting tracer within the volume between two detectors can be measured. For 3D tomographic imaging, it is necessary to rotate the pair of detectors about the field of view so as to measure projections at all angles, from which the 3D distribution of tracer can be reconstructed. In the PEPT, instead of forming an image for the tracer particle, we simply calculate a single tracer's location on the basis that the paths of the detected gamma-rays should all meet at this location to within the resolution of the camera.

This Birmingham PET camera is a Forte dual-headed gamma camera. It consists of two heads on a motorised gantry, which permits rotation about a horizontal axis, and adjustment of the face-to-face separation of the detectors from 250 to 800 mm. Each head contains a single crystal of NaI(Tl) scintillator, 500x400 mm^2 and 16 mm thick, optically coupled to an array of 55 photomultiplier tubes (49×76 mm tubes and 6×50 mm tubes). Every photomultiplier is connected to a separate ADC and a single board computer which controls the 55 ADC channels in the head. The dead-time per pulse is approximately 170 ns and each head can operate at a singles rate of over 2M cps [Par02]. If an equipment of interest can be set up between the two detectors of a positron camera, within the field of view (FOV), tracking can be completed without any difficulty. The Forte has an FOV of 80x50x40 cm^3 and is mounted on rails which allow the camera to move easily. With a central point source, useful count rates of over 100k events/s can be achieved [Par02]. The spatial resolution of the camera (FWHM of the back projected image of a point source) is approximately 5 mm [Par02]. A picture of the Birmingham positron camera can be seen below (Figure 1.8). Typical electronics for a coincident detection camera can be seen underneath (Figure 1.9).

Figure 1.8: Birmingham positron camera

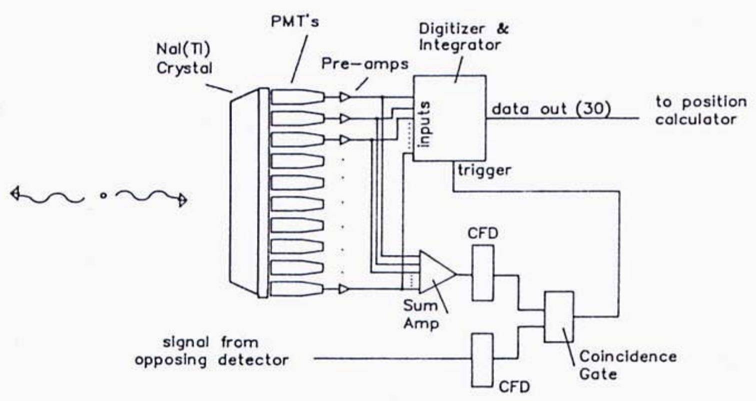

Fig. 2. Schematic of detector and processing electronics.

Figure 1.9: Typical electronics for positron camera. Taken from [Kar88]

1.3.1 Interactions in the detectors

The detectors have an energy resolution of better than 15% (FWHM of the 511 keV photopeak) which is sufficient to discriminate against photons scattered by more than 30°. The energy resolution is defined using the formula below (1.24).

$$R = \frac{Full\ \ Width\ at\ Half\ Maximum}{Full\ \ Energy\ Peak} \tag{1.24}$$

The shape of the full energy peak can be described as an approximate Gaussian function. The mean of this Gaussian function is related to the average energy of the gamma-ray. The width of the Gaussian function shows something of the precision with which the NaI(Tl) detector measures the energy of the gamma-ray. The full energy peak is built up from a series of atomic processes after a gamma-ray loses all its energy in the detector. The photoelectric effect, Compton effect and pair production are the three major interactions for a gamma-ray to react within the NaI(Tl) detector. For the pair production, near the nucleus of a detector atom, the gamma-ray is converted into a positron-electron pair. As the electron has a rest mass of 0.511 MeV, the minimum energy of a gamma-ray needed to have the effect of pair production is 1.022 MeV. Nevertheless, in practice, the highest probability of this effect's occurring in the detector is the gamma-ray with energy above 4 MeV. Therefore, in our detection of 0.511 MeV gamma-ray from the positron annihilation, the major interactions of gamma-rays with the NaI(Tl) will be the photoelectric effect and the Compton effect.

For the photoelectric effect occurring in the detector, the probability of occurrence of the photoelectric effect is directly related to the Z of the absorber and inversely related to the energy of the gamma-ray. Thus, a lower energy gamma-ray (<1 MeV) in the high-Z absorber most often has the photoelectric effect. After the photoelectric interaction takes place, the incident photon completely disappears and one ejected electron with kinetic energy goes on to ionize other atoms. The resulting atom is left in an excited state. The atom may then de-excite by one of several different atomic processes. For example, an electron may fill the atomic vacancy created by the ejection of the photoelectron with the subsequent emission of a lower energy photon (X-ray process) or this emission photon may cast out an outer-shell electron (Auger process). The low-energy x-rays and Auger electrons are unable to escape an NaI(Tl) scintillator detector. X-rays will be absorbed by detector atoms causing additional excitations while the Auger electrons will give up their kinetic energy through electric interactions with other detector atoms. In the photoelectric effect, the ejected electron can have kinetic energy which is the difference between gamma-ray energy and the bonding energy in the atom for this electron. A basic formula (1.25) for the photoelectric effect is formulated below.

$$KE_{max} = E_{\gamma} - W \tag{1.25}$$

where KE_{max} is the maximal kinetic energy of the ejected electron, E_{γ} is the energy of the incident photon and W is the work function which is the minimum energy required to remove an electron from atomic bonding.

For the Compton effect to occur in the detector, the produced new scattered photon may either be absorbed by the photoelectric effect, or, if the energy is still high, it may go on to have another Compton scattering. Compton scattering occurs in all materials and predominantly with photons of medium energy, i.e. about 0.5 to 3.5 MeV. Some formulae below (1.26~1.28) can be seen to describe the energy of a scattered photon which a scatter angle of 30° can possess in the Compton effect. In the formula (1.26), $E\gamma'$ is the energy of the scattered photon, $E\gamma$ is the energy of the incident photon, m_e is the rest mass of the electron, c is the speed of light in vacuum and θ is the scatter angle of the scattered photon. After the calculation, a scatter photon with a scatter angle of 30° can own 88% of the energy 511 keV. Compared with the energy resolution, if the detector has 15% energy resolution, it should be able to detect this Compton scattered photon which has a 12% loss of energy 511 keV. For the scatter photons with different scatter angles in the Compton effect, we find the figure below (Figure 1.10) describes the energy ratios of scattered photons to 511 keV photons at different scatter angles.

$$\frac{1}{E_{\gamma'}} = \frac{1}{E_\gamma} + \frac{1}{m_e c^2}(1 - \cos\theta) \tag{1.26}$$

$$E_{\gamma'} = \frac{E_\gamma}{1 + \frac{E_\gamma}{m_e c^2}(1 - \cos\theta)} \tag{1.27}$$

$$For\ \ 511\ \ keV\ \ \gamma-ray,\ \ E_\gamma = m_e c^2$$

$$E_{\gamma'} = \frac{E_\gamma}{2 - \cos\theta} \tag{1.28}$$

$$For\ \ \theta = 30^\circ,\ E_{\gamma'} = 0.88\ \ E_\gamma$$

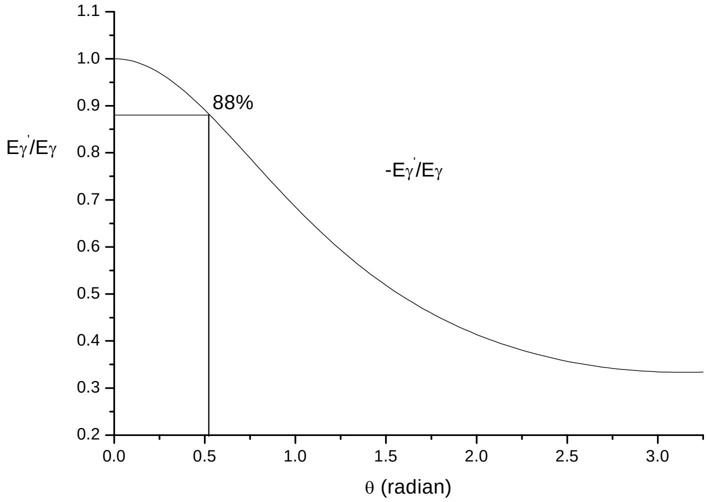

Figure 1.10: The energy ratios of scattered photons to 511 keV photons at different scatter angles

The quantum efficiency of each head of the ADAC Forte for detecting 511 keV photons is approximately 23% (full spectrum) or 16% using only photopeak pulses, while the coincidence resolving time is 7.5 ns. The concept of quantum efficiency is formulated (1.29, 1.30) and described schematically (Figure 1.11) as below. If we use only the photopeak pulses in area 1 in Figure 1.11, the quantum efficiency is 16%; if we use the full spectrum area 1+2 in Figure 1.11, the quantum efficiency will be 23%. This value of 23% means the useful pulses which are given off by 23% of the gamma-rays striking a detector. Thereby the overall efficiency for detecting a pair of gamma-rays is nearly 5% (23%x23%).

$$\frac{No.\ of\ \ pulses\ \ in\ 1}{No.\ of\ \ \gamma-rays\ \ striking\ \ detector} = 16\% \tag{1.29}$$

$$\frac{No.\ of\ \ pulses\ \ in\ 1+2}{No.\ of\ \ \gamma-rays\ \ striking\ \ detector} = 23\% \tag{1.30}$$

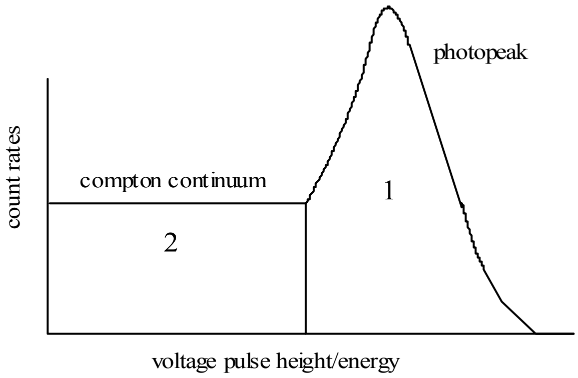

Figure 1.11: Ideal pulse height spectrum

In theory, we can calculate the reaction rate at which the gamma-rays interact with the crystal. A formula is given below (1.31) to calculate the reaction rate.

$$I = I_{\circ} e^{-\mu x} \tag{1.31}$$

where I_o is the incident intensity of gamma-rays, I is the final intensity after leaving the crystal, x is the reaction depth and μ is the linear attenuation coefficient. For a 511 keV gamma-ray in NaI, $\mu \sim 0.33$ cm^{-1}, the thickness of NaI for Forte is 1.6 cm. The fraction of interaction will be $(I_{\circ} - I_{\circ} e^{-\mu x})/I_{\circ} \sim 0.41$ which means that there are 41% incident gamma-rays to interact with the crystal. In reality, the quantum efficiency is affected by many factors such as the PMT tube and the crystal quality. It will never reach such a high efficiency value (41%).

1.4 Example of PEPT (Pendulum)

For all systems of interest confined between the two detectors, the operation procedure to track a tracer is similar. A tracking program under the UNIX system is responsible for producing the relationship between the position and time of the tracer particle. A PC Windows program "Track" will be used to process the results files from the tracking program under the UNIX system. This Track program can produce some preliminary visualization plots for the tracer movement. Basically, the tracking procedure is shown as a schematic below (Figure 1.12):

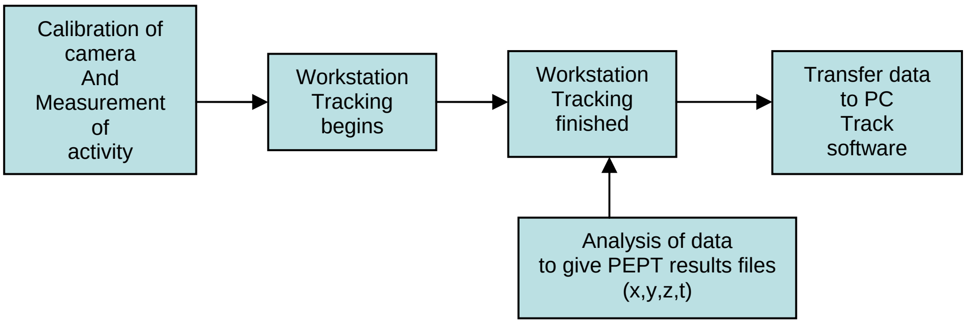

Figure 1.12: Tracking Procedure

1.4.1 The coordinate system for the camera

The purpose of tracking a tracer is to know how its position changes with time. In order to follow how the tracer's position changes with time between the two detectors, we must know the pre-defined coordinate system for the positron camera. Figure 1.13 shows the coordinate system of the positron camera. From this figure, it is clear where the origin is. The x-axis is entering the paper from the coordinate origin. If the two detectors are symmetrical or co-linear, a tracer moving along the z-axis only will not change its relative position on the monitor which we are viewing.

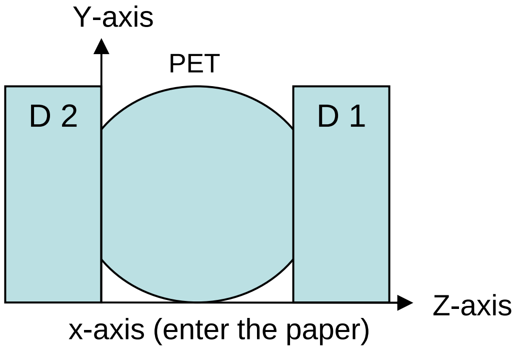

Figure 1.13: The coordinate system for tracking a tracer

1.4.2 PEPT results file

Before executing the tracking, we must make sure that the calibration operation for the positron camera is finished, the activity of the tracer is ready for use and the experimental equipment is confined within the field of view of the two detectors. When we are ready to begin tracking, we will need to execute a command called 'petlog' which is an executable file on the workstation. On the petlog tracking panel, we need to define some parameters including the run name, first run number, the separation of the two detectors, their relative angle, the route of the destination directory for storing data files, the preset time and the title of this test. The tracking time is totally a matter for the researcher. Once we think the time for tracking is long enough, we can stop it through the petlog tracking panel and the tracking will be automatically terminated. Data from the positron camera consist of the co-ordinates of the pairs of detected γ-rays. They are processed using the PEPT algorithm and produced through an ASCII file containing a sequence of tracer locations as a function of time. Each file consists of a header detailing experimental and processing conditions followed by a list of locations. There is a structure of PEPT results file below (Table 1.3) which is also the forepart of the data obtained from the simple pendulum test (section 1.4.4).

From Table 1.3, we can see that there is a header detailing processing conditions followed by 8 columns. The first column represents the location time in milliseconds from the start of the run. The next three columns represent the Cartesian coordinates of the location x, y, z in millimeters. The 5th column represents the error, providing some indication of the reliability of this location. The range of error is generally 0～7. In some studies, the error can reach 7, but it is normally 0. If the error values are larger than 10, that will almost certainly indicate that the location process has failed. The 6th column is used for the shaft angle in degrees and the 7th column for the torque. Finally the 8th column represents the actual number of events used in calculating this location.

$test01$

$separation = 804$

$f(opt): 0.050 \quad Displacement \;\; parameters: 300,\ 400\ ,\ 1500$

$Fixed \;\; slice\text{:}\;\; 250 \; events / slice, \quad 1 \; location / slice$

Time(ms)	X(mm)	Y(mm)	Z(mm)	Error	Angle	Torque	No. of events
209	236.8	188	174.4	1.1	0	0	12
602.1	264.6	152.4	403.1	0.9	0	0	10
879.3	284	184.8	540.9	0.7	0	0	10
1263.3	258.3	150.4	371	1.4	0	0	11
1586.8	233.4	184.2	176.6	0.8	0	0	10
1846.4	246.7	160.2	252.6	1.3	0	0	10
2261.9	282	178	522.8	1.1	0	0	10
2505.5	277.9	167.5	493.3	1.1	0	0	11
2859.1	238.2	164.1	234	1.4	0	0	10
3020.7	234.7	174.9	200.3	0.7	0	0	10
3426.3	267.3	150.9	366.1	1.3	0	0	10
3773	276	170.4	498.4	0.8	0	0	10
4022.8	257.8	152	395.9	1.5	0	0	11

Table 1.3: Structure of a PEPT results file

1.4.3 Track program

After the results files are acquired on the workstation, we need to transfer these files from there to PC; a Track program on PC Windows is used for the visualization and initial analysis of these transferred PEPT results files. This Track program was produced by Dr. David Parker. Although this software has not been published, yet everyone who does data analysis of PEPT has taken advantage of its power. Basically, the PC is interconnected to the workstation. A FTP program on Windows is used to transfer those PEPT data into the PC windows. The pre-defined network address for the workstation is app1.ph.bham.ac.uk. After logging into the workstation from the FTP program, we can begin transferring these data to the PC's Windows. Below is the panel of the Track program on the Windows system. There are twelve modes of operation available within the Track program. Each mode provides a method for the presentation and analysis of PEPT data. We can select any modes for the different visualizations of PEPT data by pressing the appropriate buttons as shown below (Figure 1.14).

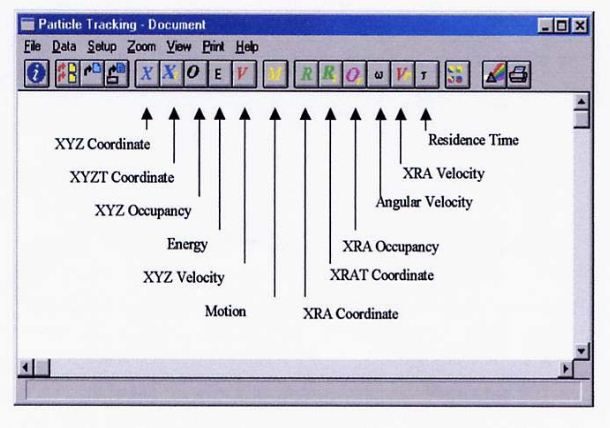

Figure 1.14: Panel of Track program

1.4.4 A result for a simple pendulum test using PEPT

A simple pendulum test was made to become familiar with the operation procedure of tracking. A pendulum with a ^{22}Na source at its end was forced to swing between the two detectors. The figure below (Figure 1.15) describes the experimental schematic. The pendulum was confined to swinging mostly in the direction of the z-axis. When the pendulum was nearly at rest after swinging for a while, it was pushed to resume oscillating. This pushing phenomenon shows in Figure 1.16 that for every several seconds a deeper pulse will be produced which may be explained by the action of using a hand to push the pendulum. This pendulum did not have a perfect harmonic oscillation due to air resistance, some friction and, as the largest source of error, the driven system (a hand).

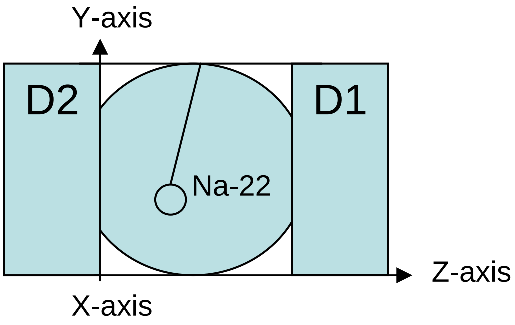

Figure 1.15: A pendulum swinging between the two detectors

Two preliminary visualization figures for the simple pendulum test are shown below (Figure 1.16 and Figure 1.17). They were the results of using a Track program to process the PEPT data from the workstation. Figure 1.16 was produced from mode 1 on the panel of the Track program. It shows that only the change in position of the z-axis over time is relatively apparent. The other two coordinates change very little. Figure 1.17 was produced from mode 4 on the panel of the Track program. It shows the probability distribution of velocity components along the x, y and z-axes.

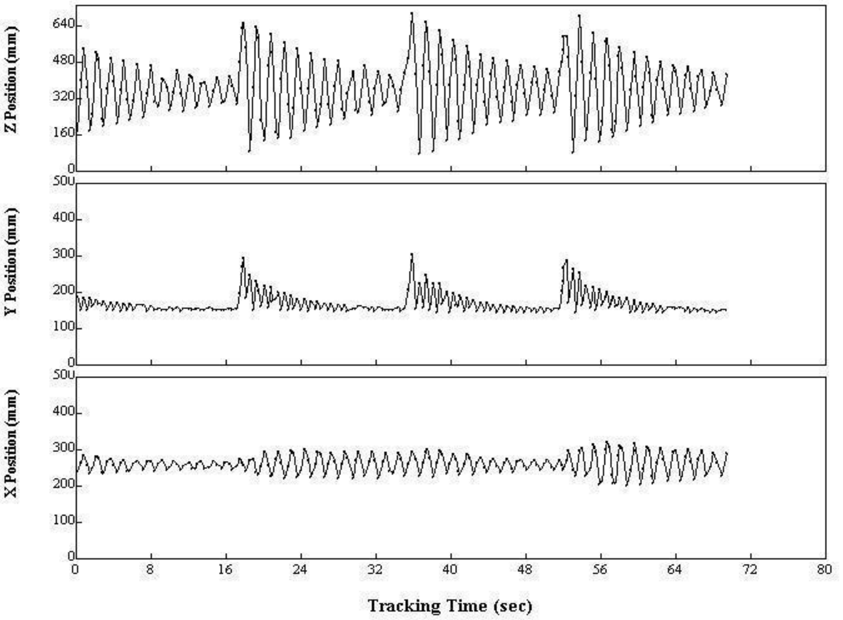

Figure 1.16: The position change with tracking time (from mode 1 on the Track program)

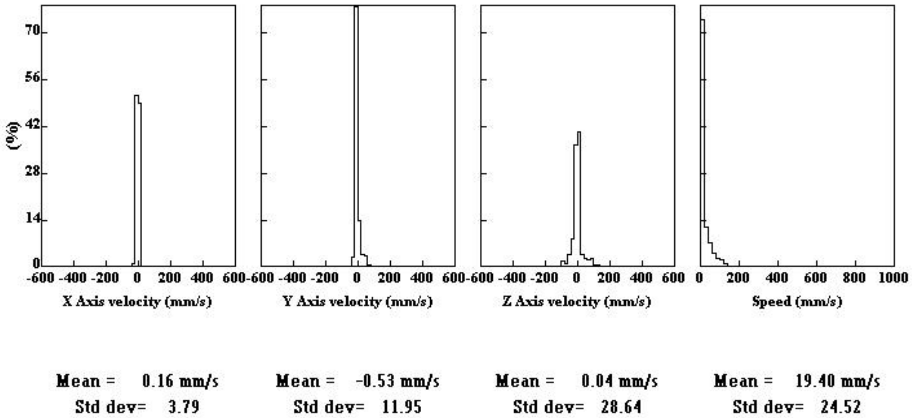

Figure 1.17: The probability distribution of velocity components (from mode 4 on the Track program)

1.5 The application of PEPT to track a single labelled red blood cell

^{11}C ($t_{1/2}$=20.385min), ^{13}N ($t_{1/2}$ =9.965min), ^{15}O ($t_{1/2}$=2.037min), ^{18}F ($t_{1/2}$=109.77min) are all positron-emitting isotopes which are used as positron sources in the PET imaging. In the PEPT technique, ^{18}F is the favourite isotope due to its longer half-life and ease of production. A tracer with enough activity required under the current PEPT technique depends on the important labelling techniques. As described in section 1.2.3, three main labelling techniques in the PEPT lab are used to produce the tracer. However, as the red cell is a biological unit and its average size is only 7.7 μm, it seems that a labelling technique different from the current techniques should be considered. There is an interesting description of the labelling size below. If we try to label a tracer particle with a dimension of 10 μm using only one ^{11}C atom, we will find that it is like using a big ball with a dimension of 520 m to touch the earth we live on.

In the blood vessels of the human body, the bonding affinity of haemoglobin for CO is 200 times greater than its affinity for O_2. When the CO is absorbed by the red cell, it combines with the oxygen carrying haemoglobin to form carboxyhaemoglobin. The bonding positions of ^{11}CO are exactly the same as the bonding positions of O_2. For this feasibility study, the main problems related to tracking a red cell in vitro are how to label it with enough activity required under the current tracking technique and how to isolate it. If we can overcome these problems, we should be able to track a single labelled red cell in a test pipeline system using the PET camera and the PEPT technique. As ^{15}O's half-life is too short, it may not be suitable for labelling the red cell.

In section 3.4, I show that if every bonding position in a red cell was occupied by a ^{11}CO, the cell would have an activity of 0.015 mCi (15 μCi). Using the PEPT technique, we assume that there is a tracer with an activity of 0.3 mCi. With the ADAC Forte this gives approximately 13k events/s using 20% energy windows and detectors which are 60 cm apart. The data rate depends on the camera's geometry. If 100 events are needed to determine the tracer's location, we can get 130 locations every second and locate every 8 ms (1000 ms/130). Suppose this tracer is moving at 1 m/s, in 8 ms it can move a distance of 8 mm. Technically we can increase the data rate by opening the energy windows or moving the detectors closer. For example, with an activity of 0.15 mCi for a tracer, if we move the detectors closer and increase the energy windows, we should be able to track it at 1 m/s and with an activity 0.015 mCi we should be able to track at 0.1 m/s. In the human aorta, the blood speed is close to 0.3 m/s, but in human capillaries the speed is less than 1 cm/s. These two speeds can provide a reference and comparison when tracking a red cell in vitro.

Unfortunately some results from other groups indicate that it is extremely difficult to achieve pure ^{11}CO (～9200 Ci/μmole). The specific activity reported is less than 1% of the theoretical value due to dilution by ^{12}CO and other chemical forms. In other words, based on their measurements, in theory it is impossible to achieve a labelled red cell with an activity of 15 μCi, because this requires an SA of 9200 Ci/μmole and perfect labelling for the cell. The expected maximum activity of a labelled red cell should be only 1% of 15 μCi. Nevertheless in PEPT with adjustment of the energy windows and the distance of the detectors, we are still able to track a tracer with an activity much lower than 0.15 μCi. But obviously the maximum velocity of a tracer one can usefully track at is much lower.

Incidentally, based on the fast development of molecular manufacturing to allow the construction of micron-scale machines comprising nanometer-scale components [Fre98], it may be possible in the future to develop a "magic carrier" with which the radioactive atoms probably can be labeled and a labelled carrier can flow in a test system to provide information using the PEPT technique. For example, this artificial micron-scale machine can be an artificial red cell, which can probably be labelled with ^{11}CO and used in PEPT for the tracking purposes.

1.6 Outline of thesis

Chapter 1 mainly describes the related concepts of PEPT and provides an example to show how PEPT works. The possibility estimation and the future possible development for tracking a single red cell are also mentioned in section 1.5. Chapter 2 mainly introduces the related concepts of nuclear reaction, the function of the MC40 cyclotron, some important issues related to producing ^{11}CO and the related measures of the produced ^{11}CO. I did much experimental work to produce ^{11}CO successfully, but was not able to measure purity due to the lack of instruments. Chapter 3 mainly describes the fundamental properties of red cells and haemoglobin and introduces a spectrophotometric method to decide the concentrations of oxyhaemoglobin and carboxyhaemoglobin. Dr David Parker and I built a simple manual set-up for labelling the red cells. This set-up can be used only to investigate the possibility of labelling the red cells. It was not able to provide other quantitative analyses. I did some preliminary trials of this simple manual set-up to label the red cells. A preliminary intensity image of red cells labelling is shown in Figure 3.14. Several methods to isolate a single labelled red cell are also proposed for future reference. A theoretical maximum activity of a single labelled red cell is shown in section 3.4. Chapter 4 mainly describes the related ideas for building a future simulated in vitro blood flow system. The concept of CFD is also mentioned. I discuss the related contents in this thesis in the last section, 4.4.

Chapter 2

Production of ^{11}CO

In the Positron Imaging Centre, the most often used radioisotope is ^{18}F. As the glass bead has abundant oxygen-16 atoms, ^{18}F can be produced within small glass beads through nuclear reaction ^{16}O(^{3}He,p)^{18}F or ^{16}O(^{3}He,n)^{18}Ne$\rightarrow$^{18}F. Moreover, suitably radioactive glass tracers down to 1 millimeter in size can be produced successfully. In order to meet the extensive applications of PEPT in pharmaceutical and organic industries, the technique of ion exchange has recently been used to produce ^{18}F labeled polystyrene resin particles which can be as small as 60 μm. For this technique, ^{18}F is firstly produced in solution and then transferred into resin beads by ion exchange. In some PET centres, the nuclear reaction ^{18}O(p,n)^{18}F is used to produce ^{18}F as well (in natural oxygen, there is 0.2% ^{18}O).

The radionuclide ^{11}C can in principle be produced in three different ways: (1) an accelerator (cyclotron or Tandem Van de Graaff) can produce carbon-11 through ^{14}N(p,α)^{11}C or ^{11}B(p,n)^{11}C; (2) ^{11}C is produced from activated charcoal in an oxygen environment, by ^{12}C(γ,n)^{11}C photonuclear reaction (threshold energy 18.7 MeV), or produced in water through the reaction of ^{16}O(γ,αn)^{11}C [Bar96]. Both reactions use bremsstrahlung gammas, which come from the electron beam impinging on a suitable target; and (3) protons of energies up to 37 MeV are generated when ultra-intense lasers (up to 1020 Wcm^{-2}) interact with hydrogen containing solid targets [Led05]. These protons can be used to induce nuclear reactions in secondary targets to produce ^{11}C via (p,n) reaction or ^{13}N via (p,α) reaction.

The Birmingham MC40 cyclotron can be used to produce the radionuclide ^{11}C. Several nuclear reactions below can be used to obtain ^{11}C by this means: (1) ^{14}N(p,α)^{11}C; (2) ^{11}B(p,n)^{11}C; (3) ^{11}B(d,2n)^{11}C; (4) ^{10}B(d,n)^{11}C; and (5) ^{12}C(^{3}He,α)^{11}C. Reaction (1) was used in Birmingham. Through the ^{14}N(p,α)^{11}C nuclear reaction, carbon-11 was produced by the proton bombardment of pure nitrogen. A mixture of a tiny amount of oxygen in nitrogen can produce radioactive carbon dioxide ^{11}CO$_2$ in the reaction chamber [Lap03]. Carbon monoxide (^{11}CO) can then be produced by reduction of ^{11}CO$_2$ on zinc powder at 390°C or on activated charcoal at 900°C [Iwa81].

2.1 Direct reaction

There are many types of nuclear reaction, but they can be divided roughly into two groups, compound nucleus reactions and direct reactions. In the compound nucleus reaction, the bombarding particle is captured by the target nucleus to form an intermediate state - the compound nucleus. In this kind of nuclear reaction, it is expected that all sense of direction of the incident particle will be lost. A compound nucleus has no memory of how it was formed. The lifetime of compound nuclei is about 10^{-16} s. The subsequent decay of this intermediate state is largely independent of the mode of formation. A given compound nucleus may decay in one or more ways, depending on its excitation energy.

The second type of reaction does not involve the formation of an intermediate state. This type of reaction, in which there is no relatively long-lived intermediate compound nucleus, is called a direct reaction. Direct reactions occur on a short time-scale of about 10^{-21} s. This is the time taken for the projectile to travel past the nucleus rather than the span of 10^{-16}s for which a compound nucleus exists. Most direct reactions involve transfer either from or to the projectile nucleus when it passes the target nucleus. A direct reaction involving transfer is called a stripping reaction or a pick-up reaction, according to whether the projectile nucleus loses or gains nucleons in the reaction. An example of a stripping reaction is known as a (d,p) reaction. In this reaction a deuteron loses a neutron when it collides with a target nucleus and the proton originally from the deuteron continues on its path. Transfer reactions are used to produce new isotopes or nuclei, which are very difficult or impossible to produce by other methods.

For the production of ^{11}C at Birmingham, the nuclear reaction used is ^{14}N(p,α)^{11}C. According to Figure 2.1 and Figure 2.2, as some resonance peaks appear in the excitation functions, this phenomenon may suggest that the above nuclear reaction belongs to the category of compound nucleus reactions. However, from another point of view, this reaction type can also belong to a pick-up reaction, which is one kind of direct reaction. When a proton passes the target nucleus ^{14}N, the other three nucleons, including one proton and two neutrons originally from the ^{14}N nucleus, are captured by the incoming proton and the α particle appears to continue on its path. As the nuclear reaction is a probabilistic collision process, for the ^{14}N(p,α)^{11}C, we can probably explain it as the two above-mentioned types of nuclear reactions combined.

2.1.1 Cross-section

In a nuclear reaction, the area of target nucleus seen by the incident particle is proportional to the rate of reaction. The unit for cross-section is barn (b, or 10^{-28} m^2). The practical reaction probability of a nuclear reaction is proportional to the cross-section. Actual reaction cross-sections vary widely with the energy and identity of the incoming particle, and with the characteristics of the target nucleus. The values of reaction cross-sections may be calculated using quantum mechanical considerations, or they can be directly experimentally determined. In the experimental determination of a cross-section, the calculations differ according to the relative thickness of the target and its effect on the intensity of incoming particles. We can find a simple geometrical cross-section for the target nucleus. The geometrical cross-section of the target nucleus is $\sigma(\text{geometric})=\pi(R_{\text{target}})^2$, where $R=1.2A^{1/3}$ fm, 1 barn=10^{-24} cm^2 =100 fm^2. It is apparent that simple geometrical cross-section calculation for the target nucleus ignores many factors which can be important in estimating the probability of a nuclear reaction, such as the projectile energy, projectile size and the stability of the target nucleus.

2.1.2 Thin targets

In a thin target, the flux density of projectiles and cross-section σ are assumed to be constant throughout the target. If the slab is thin enough, none of the nuclear cross-sections overlaps any others. In formula (2.1) below, $N_{incident}$ is the number of incident particles and $N_{product}$ is the number of produced products. For each incident particle, the probability of reaction $N_{product}/N_{incident}$ is equal to (no. of atoms/area)$\times\sigma$, where (no. of atoms/area)= n (number of atoms per unit volume)$\times t$ (thickness of thin target). In the second formula (2.2) below, R is the reaction rate and I is the incident intensity. The two formulae (2.1, 2.2) are without doubt equivalent to each other.

$$N_{product}=N_{incident}\times n\times t\times\sigma \tag{2.1}$$

$$R_{reaction}=I_{intensity}\times n\times t\times\sigma \tag{2.2}$$

2.1.3 Thick targets

For a thick target, the energy of incident particles will change. A cross-section is a function of an incident particle's energy. This means that the σ value will change as the penetration depth and the reaction rate will never be proportional to a constant σ. It is assumed that the number of target nuclei is not significantly depleted during irradiation, which is most often true. The number of incident particles is also not significantly changed with depth. The experimental total cross-section as a function of incident energy can be seen from Figures 2.1 and 2.2 in which the unit of y-axis is mb (milli-barn). The formula below (2.3) describes the relationship between the reaction rate and σ in a thick target.

$$R=I\times n\int_{front}^{back}\sigma(E)\frac{1}{\frac{dE}{dx}}dE \tag{2.3}$$

where *R* is the reaction rate, *I* is the intensity of incident particles, *σ(E)* is the cross-section function of energy, front and back mean that the incident particles penetrate the thick target from front to back and *x* is the variable of penetration depth.

2.1.4 Threshold energy for $^{14}N(p,\alpha)^{11}C$

The threshold energy of $^{14}N(p,\alpha)^{11}C$ is 3.129 MeV. In order to calculate the threshold energy, it is better to use the concept of Δ (mass difference). In nuclear physics, Δ is defined as M-A, where M is the atomic mass and A is the mass number. The unit use of Δ is MeV. Δ of ^{1}H is 7.2890 MeV; Δ of ^{14}N is 2.8637 MeV ; Δ of ^{11}C is 10.648 MeV; Δ of ^{4}He is 2.4248 MeV. Thereby, the Q value for this nuclear reaction $^{14}N(p,\alpha)^{11}C$ is equal to -2.9201 (7.2890+2.8637-10.648-2.4248) MeV. In order to make this reaction occur, the energy of the proton beam in the laboratory reference frame KE_{lab} should exceed the threshold energy. The two formulae below (2.4, 2.5) can be used to calculate this threshold energy. As we can see from the formula (2.4), the least KE_{CM} (the kinetic energy in the reference frame of center of mass) can be equal to 2.9201 MeV. Using the second formula (2.5), we can find the threshold energy (=the least KE_{lab}). In the formula (2.5), M_p is the mass of incident proton and M_N is the mass of nitrogen atom.

$$KE_{CM} + Q \geq 0 \tag{2.4}$$

$$KE_{lab} = (\frac{M_P + M_N}{M_N}) \times KE_{CM} \tag{2.5}$$

At Birmingham, we were using a proton beam with energy of 16 MeV to bombard the target gas N_2. This energy is much greater than the threshold energy. Hence it was no problem to secure this nuclear reaction.

2.1.5 Total cross-section for $^{14}N(p,\alpha)^{11}C$

The total cross-section of absorption of a particular accelerated particle is the sum of all partial cross-sections. When the proton beam is bombarding the nitrogen gas, several reactions (p,pn), (p,n), (p,2p), (p,d), (p, α) may happen. The total cross-section is for all reactions in nitrogen. The two figures (Figure 2.1 and Figure 2.2) below can describe the relationship between proton energy and total cross-section (mb) for the nuclear reaction of $^{14}N(p,\alpha)^{11}C$.

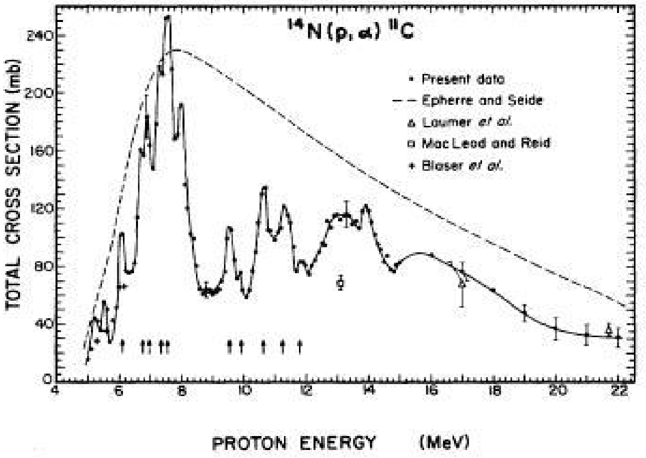

Figure 2.1: Total cross-section for $^{14}N(p,\alpha)^{11}C$ against $E_{lab.}$ Taken from [Jac74]

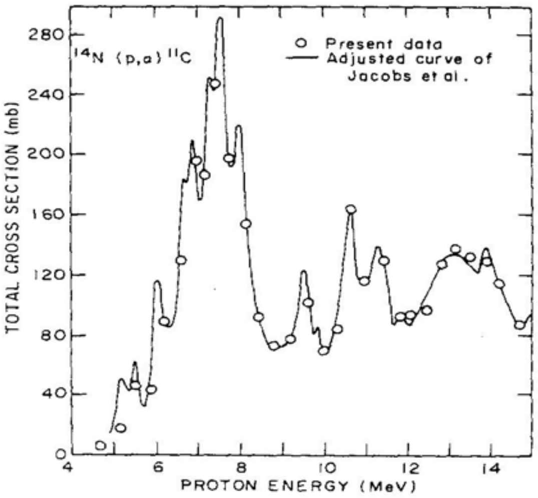

Figure 2.2: Total cross-section for $^{14}N(p,\alpha)^{11}C$ against $E_{lab.}$ Taken from [Cas78]

2.1.6 Theoretical calculation of produced activity of $^{11}CO_2$ in the target

As we know, using the energetic beam from the Scanditronix MC40 cyclotron to bombard a solid, liquid or gas target can produce some radioactive atoms within the target. From the theoretical consideration of $^{11}CO_2$ production in the target, two related formulae (2.6, 2.7) are derived as shown below.

$$\frac{dN}{dt} = R - \lambda N \tag{2.6}$$

$$N = \frac{R}{\lambda}(1 - e^{-\lambda t}) \tag{2.7}$$

where N represents the number of produced radioactive atoms, R is the production rate which is a constant, λ is the decay constant (unit=s^{-1}). The above two formulae and the figure below (Figure 2.3) can be used to show the relationship between decay rate and production rate in the target chamber. From Figure 2.3 which is plotted on the basis of formula (2.7) if we choose R=1, we can find in direct irradiation that the production rate is constant, but the decay rate will saturate with the production rate. The saturation curve in Figure 2.3 would decrease if all atoms in target were used up, but in most conditions, this is not a problem. It should be noted that the material for the target holder must resist high temperatures during the period of bombardment. Most cooling systems use water as a coolant.

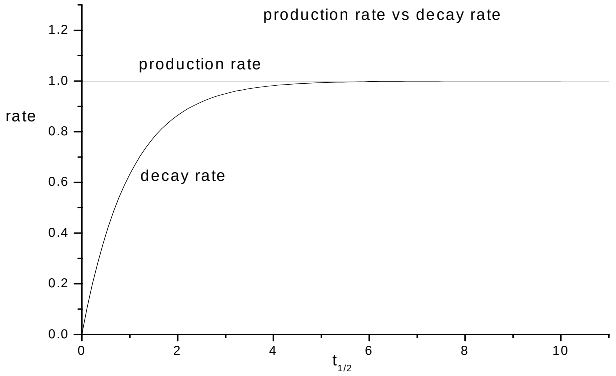

Figure 2.3: Decay rate and production rate

We can use $N_{prod}=N_\circ \times n \times t \times \sigma$ (formula (2.1)) and $\lambda N=R(1-e^{-\lambda t})$ (formula (2.7)) to calculate the activity value of the $^{11}CO_2$ produced in the target. The value of R can be calculated from N_{prod}. Thereby, if we know the value of $N_\circ$,n ,t and σ (average), we can obtain the R value. $N_\circ$ is related to incident intensity. This value can be calculated precisely from the beam current in a cyclotron; n is the number of target atoms per unit volume which is related to target pressure and ambient temperature in our reaction chamber; t is the depth of the reaction chamber; σ is the average total cross-section; $t_{1/2}$ is 1223.1 s; λ is (ln2/1223.1 s)=0.000567 s^{-1}. The table below (Table 2.1) lists 8 activity values due to different bombardment times. If we choose R=1, the activities in Table 2.1 basically are exactly consistent with Figure 2.3.

$t=t_{1/2}/8$	$\lambda N=R(1-e^{-\lambda t})=0.083R$
$t=t_{1/2}/4$	$\lambda N=R(1-e^{-\lambda t})=0.159R$
$t=t_{1/2}/2$	$\lambda N=R(1-e^{-\lambda t})=0.293R$
$t=t_{1/2}$	$\lambda N=R(1-e^{-\lambda t})=0.500R$
$t=2t_{1/2}$	$\lambda N=R(1-e^{-\lambda t})=0.750R$
$t=4t_{1/2}$	$\lambda N=R(1-e^{-\lambda t})=0.937R$
$t=8t_{1/2}$	$\lambda N=R(1-e^{-\lambda t})=0.996R$
$t=10t_{1/2}$	$\lambda N=R(1-e^{-\lambda t})=0.999R$

Table 2.1: Theoretical activities

2.2 Cyclotron

Ernest Lawrence and M. Stanley Livingston built the first cyclotron to accelerate charged particles at Berkeley in 1931. The basic principle of a cyclotron is that when a charged particle is orbiting one semicircular path in a Dee, the time it takes is independent of the radius of the path. The reason is that when the charged particle spirals to a larger radius, it also gains energy and spirals at greater speed. The gain in path length is basically compensated for by the greater speed. For a particle mass *m*, charge *q* in magnetic field *B*, assuming uniform *B* and invariant mass, the dominant formulae (2.8~2.10) can be seen below. The circular motion is maintained by the Lorentz force=qvB; the time taken for a semicircular orbit is $m\pi/qB$; the orbital frequency is $qB/2\pi m$. A typical cyclotron can also be seen below (Figure 2.4).

$$F=\frac{mv^2}{r}=qvB \tag{2.8}$$

$$t=\frac{m\pi}{qB} \tag{2.9}$$

$$f=\frac{\omega}{2\pi}=\frac{qB}{2\pi\, m} \tag{2.10}$$

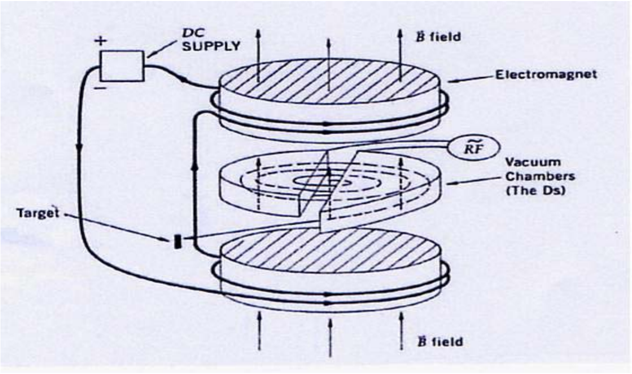

Figure 2.4: Schematic for a typical cyclotron. Taken from [Das94]

As we are increasing the energy for charged particles, the relativistic behaviour of the accelerated charged particles becomes clear. The frequency relation above fails, due to the increased mass. As the spiral speed is near the speed of light, the mass of the charged particle is increased. The momentum of the charged particle *mv* is replaced by γmv. γ is equal to $(1-\beta)^{-1/2}$, $\beta=v/c$. This effect cannot be compensated for when using a fixed-field, fixed-frequency cyclotron. The relativistic effect appears easily at lower energies when accelerating electrons. Therefore, a fixed-frequency cyclotron is not suitable for accelerating the electrons.

In order to reach the relativistic energies when using a cyclotron, there are two main ways to compensate for this relativistic effect. One way is to vary the resonance frequency. As we can see from the above frequency relation, when mass is increased, if the frequency is increased as well, the relationship can be maintained. This kind of cyclotron is called a synchrocyclotron. Another way is to increase the magnetic field with the increasing orbital radius. The increasing mass can be compensated for from the increased magnetic field. This kind of cyclotron is called the AVF (azimuthally varying field) cyclotron, which has specially shaped magnets to create variations in the magnetic fields. The particles can maintain the same time of flight (despite their increased relativistic mass) by the increase in B in the AVF cyclotron.

2.2.1 A Scanditronix MC40-MVA cyclotron at Birmingham

A Scanditronix MC40-MVA cyclotron is now (Figure 2.5) in operation at the University of Birmingham. This cyclotron was originally obtained from a hospital in Minneapolis, USA, in 2002 and has run successfully since early 2004. Most modern cyclotrons use negative ion acceleration to simplify extraction. MC40 is a positive ion accelerator, which can accelerate protons, deuterons and helium ions. Its major applications in this school are: (1) producing radionuclides for engineering systems studies; (2) producing radionuclides for radiopharmaceuticals and medical studies; (3) producing radionuclides for laser studies; (4) testing Charissa detectors prior to overseas runs. Table 2.2 lists some of the particles usually accelerated and their masses in MeV/c^2.

Figure 2.5: Birmingham's MC40 Cyclotron

Particle	proton	deuteron	$^3He^{2+}$	$^4He^{2+}$
mass	938.27	1875.6	2809.4	3727.4

Table 2.2: Masses of charged particles: MeV/c^2

The ion source for the MC40 is a central hot filament. When ions orbit in a magnetic field (the maximum magnetic intensity is 1.8 T), they will pass through hollow Dees. There are two 90° Dees with separate radiofrequency systems. Acceleration is provided by radiofrequency. Accelerating frequency is equal to $N\times$orbital frequency (N=harmonic number; N=1 for out of phase and N=2 for in phase). From equations (2.11) and (2.12), where q is the charge of the particle, B is the magnetic field, R is the extraction radius, c is the speed of light in vacuum, m is the rest mass of the electron and E is the energy, one can deduce the gained energy at N=1 or N=2 under these known parameters. For example, when producing carbon-11, the energy of the proton beam can be deduced from the formulae below. If we choose the harmonic number N=1, the orbital frequency=16.72 MHz and the extraction radius R=0.53 m, from the practical calculation using the formulae below (2.11, 2.12), the energy of the proton beam used to bombard the target gas can be found to be~16.16 MeV. Table 2.3 lists some energies gained for different charged particles when their harmonic numbers are 1 or 2.

$$Accelerating\ frequency = N \times Orbital\ frequency = \frac{NqB}{2\pi\ m} \tag{2.11}$$

$$\frac{NqB}{2\pi\ m} = \frac{Nc}{2\pi\ R}\sqrt{\frac{2E}{mc^2}} \tag{2.12}$$

Protons	N=1	12-40 MeV
Protons	N=2	3-10 MeV
Deuterons	N=2	6-20 MeV
$^4He^{2+}$	N=2	17-40 MeV
$^3He^{2+}$	N=1	35-53 MeV
$^3He^{2+}$	N=2	13-30 MeV

Table 2.3: Energies of Charged particles from the cyclotron

Voltage (maximum Dee voltage is nearly 30 KV) on Dees oscillates at the precise frequency to accelerate ions when they enter or leave. The driven system is tuneable between 14 and 28 MHz using a variable quarter wave stub. At R=53 cm, a beam is extracted using an electrostatic deflector (30 KV) followed by a magnetic channel and internal steering magnet.

A schematic diagram below (Figure 2.6) describes the practical orbit for a particle to run in the MC40 cyclotron. As can be seen from Figure 2.6, the two 90° Dees named D1 and D2 have separate radiofrequency systems and the four dummy gates are grounded. The particle can be accelerated during the passages of these four gaps and gain energy. The phase change at N=1 and N=2 can be seen from Figure 2.7 and Figure 2.8. In Figure 2.7, at N=1, the oscillation curve for D1 is a '$-\cos\theta$' function and the oscillation curve for D2 is a '$\cos\theta$' function. In Figure 2.8, at N=2, the oscillation curve for D1 and D2 is a '$-\sin 2\theta$' function. Due to the Faraday shielding effect, when the particle is orbiting in the Dees, it does not feel any electric field exerted on it.

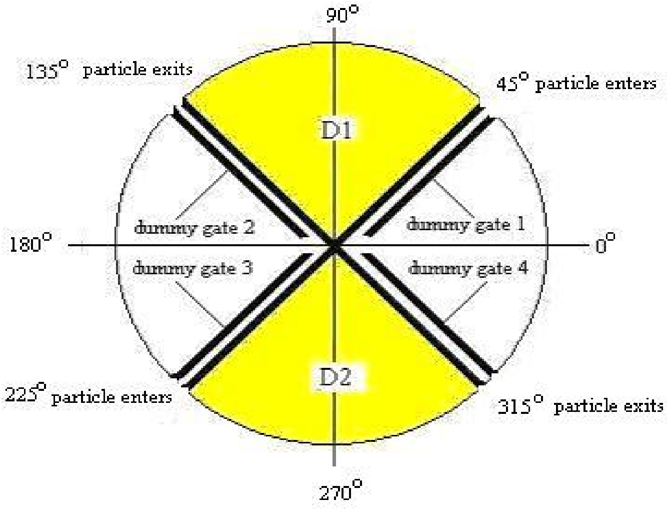

Figure 2.6 A schematic diagram for a particle to run in the MC40 cyclotron

For N=1, the voltages on D1 and D2 are out of phase, as can be seen from Figure 2.7. At 45°, the particle leaves dummy gate 1, enters D1 and gains the energy $qV_{max}/\sqrt{2}$ in this gap. The voltage value at 45° can be seen from Figure 2.7 (1). At 135°, the particle exits D1, reaches dummy gate 2 and gains the energy $qV_{max}/\sqrt{2}$ in this gap. The voltage value at 135° can be seen from Figure 2.7 (1). At 225°, the particle leaves dummy gate 3, enters D2 and gains the energy $qV_{max}/\sqrt{2}$ in this gap. The voltage value at 225° can be seen from Figure 2.7 (2). At 315°, the particle exits D2, reaches dummy gate 4 and gains the energy $qV_{max}/\sqrt{2}$ in this gap. The voltage value at 315° can be seen from Figure 2.7 (2). For the total energy gained per turn at N=1 by the particle, as can be found from the above calculations, the particle may gain $qV_{max}/\sqrt{2}$ at each gap crossing whereby the total energy gained per turn for the particle at N=1 is $4qV_{max}/\sqrt{2}$.

For N=2, the voltages on D1 and D2 are in phase, as can be seen from Figure 2.8. At 45°, the particle leaves dummy gate 1, enters D1 and gains the energy qV_{max} in this gap. The voltage value at 45° can be seen from Figure 2.8 (1). At 135°, the particle exits D1, reaches dummy gate 2 and gains the energy qV_{max} in this gap. The voltage value at 135° can be seen from Figure 2.8 (1). At 225°, the particle leaves dummy gate 3, enters D2 and gains the energy qV_{max} in this gap. The voltage value at 225° can be seen from Figure 2.8 (2). At 315°, the particle exits D2, reaches dummy gate 4 and gains the energy qV_{max} in this gap. The voltage value at 315° can be seen from Figure 2.8 (2). For the total energy gained per turn at N=2 by the particle, as can be found from the above calculations, the particle may gain qV_{max} at each gap crossing, whereby the total energy gained per turn for the particle at N=2 is $4qV_{max}$.

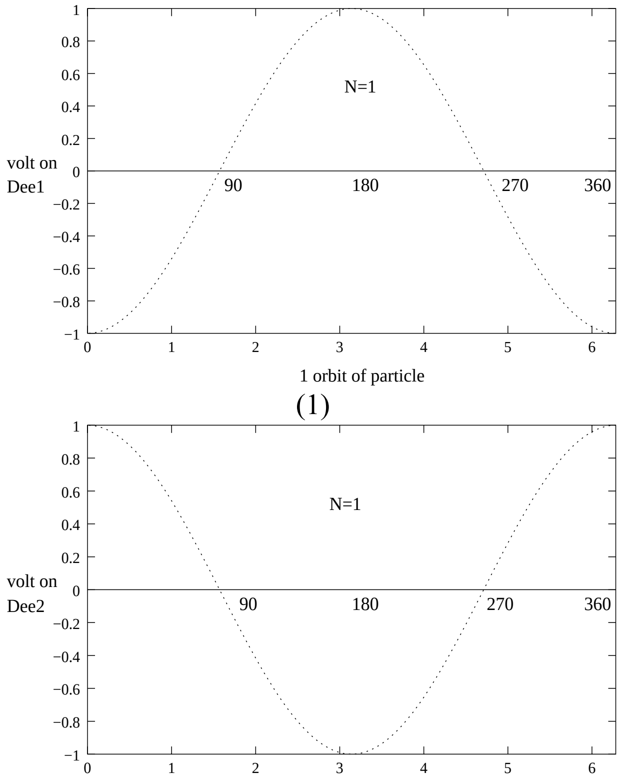

(1)

(2)

Figure 2.7: (1), (2), N=1 out of phase

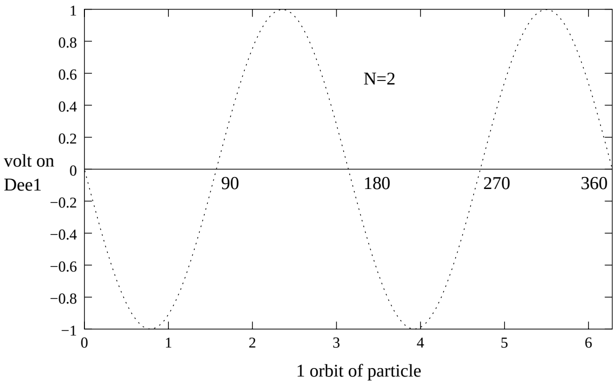

(1)

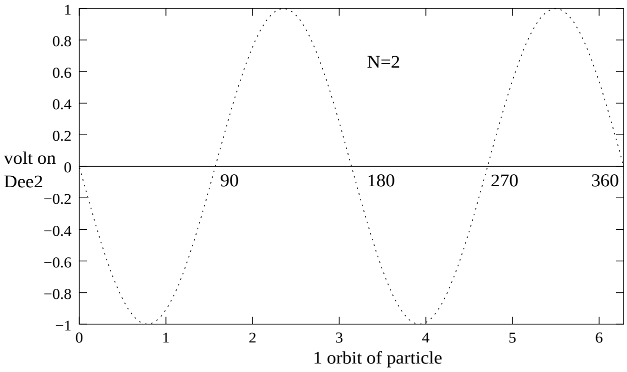

(2)

Figure 2.8: (1), (2), N=2 in phase

2.3 Practical Issues

^{11}CO is an important precursor of many ^{11}C-labelled pharmaceuticals. Its nearly 100% rate of positron emission and a suitable half-life make it a very welcome radioisotope in the study of positron emission tomography. In the following sections we discuss the factors influencing the practical production of ^{11}CO.

2.3.1 O_2 and CO_2 percentages in the target

The oxygen percentage in the reaction chamber plays an important role in synthesizing the gas $^{11}CO_2$. Several papers have suggested that the optimum oxygen percentage mixed with the oxygen-free nitrogen in the chamber should be less than 0.2 percent [Pow03, Pow00]. It is interesting that, if the reaction target is full of natural air before bombardment, from the composition data for the current atmosphere, we can estimate the possible percentage for every sort of gas in the target (nitrogen is 78.084 percent; oxygen is 20.948 percent; carbon dioxide is 0.0315 percent; carbon monoxide is 0.000012 percent.). This amount of oxygen within natural air in the target is much more than is suggested in several papers and can cause a disaster when we want merely to obtain $^{11}CO_2$. Besides the problem of oxygen concentration in the target, the concentrations of $^{12}CO_2$ and ^{12}CO in the target before bombardment should also be noticed, as they cannot be chemically separated from the desired $^{11}CO_2$ and ^{11}CO. However, by using a very powerful pump and a highly precise pressure meter, one can decide the vacuum degree in the target and estimate the rare amounts of $^{12}CO_2$ and ^{12}CO by using their probable percentages in the air. By doing the related calculations, if the pressure in the target can be kept at 0.1 mbar (using 298 K, volume of target$\sim$380 cm^3), the estimated mole number for CO_2 is$\sim$4.8x10^{-10} and the estimated mole number for CO is$\sim$1.8x10^{-13}. The target is then filled with high-purity nitrogen (using 5 atm, 298 K, volume of target$\sim$380 cm^3). The nitrogen gas is specified as 99.99% pure. If we assume that the remaining 0.01% has the same composition as air, this adds a further ~ 2.4×10^{-9} moles of CO_2 and a further ~ 9.2×10^{-13} moles of CO. Hence the total amount of CO_2 before bombardment is ~ 2.9×10^{-9} moles and the total amount of CO before bombardment is ~ 1.1×10^{-12} moles. If the ^{11}C yield in the target is 50 mCi, one finds that the mole number of ^{11}C is ~ 6×10^{-12}. Thus the ratio of CO_2 to ^{11}C is ~ 483 and the ratio of CO to ^{11}C is ~ 0.183. The ratio results need no cause for concern because the pressure kept in the target is only assumed at 0.1 mbar and it is also assumed that some CO_2 and CO exist within the high-purity nitrogen (99.99%, 5 atm in the target). One way to reduce the level of natural CO_2 in the gas used to fill the target is to pass this gas through an LN_2 before the target. And the residual CO_2 can be largely absorbed by the NaOH in the processing system. However, if the pressure in the target can be kept at 10^{-5} mbar and the high-purity nitrogen (5 atm in the target) does not contain any CO_2 or CO, one finds that the ratio of CO_2 to ^{11}C is less than 1% and the ratio of CO to ^{11}C is less than 0.0003%. If the pumping system cannot reach a vacuum level equal to or less than 0.1 mbar and the high-purity nitrogen still contains some CO_2 and CO, we can still increase the ^{11}C yield in the target and thereby decrease the ratio of ^{12}C to ^{11}C.

Knowing the oxygen level in the target holder is important for the production of $^{11}CO_2$. As a similar calculation with the mole number of CO_2 in the target after pumping, the mole number of O_2 is ~ 3.2×10^{-7} if the pressure in the target can be kept at 0.1 mbar. When the target is full of high-purity nitrogen (99.99%), the mole number of N_2 is ~ 0.076 (using 298 K, 5 atm, volume of target ~ 380 cm^3) and the estimated mole number of O_2 originally existing within the high-purity nitrogen is ~ 1.6×10^{-6}. Thereby the total amount of O_2 in the target after filling the high-purity nitrogen can be estimated to be ~ 1.92×10^{-6} moles. The ratio of O_2 to N_2 in the target before bombardment can be finally estimated to be ~ 0.00253%, which is much lower than the suggested O_2 concentration [Pow03, Pow00].

A high level of oxygen may result in the production of oxides of nitrogen NO_x. The most obvious evidence for the use of excess oxygen in the target are the reaction $^{16}O(p,\alpha)^{13}N$ and the reaction $^{15}N(p,n)^{15}O$. The produced ^{13}N can combine with each other to form $^{13}N_2$ naturally, while the produced ^{15}O can also combine with ^{16}O to form $^{15}O^{16}O$ naturally (in natural nitrogen, normally there is 99.63% ^{14}N and 0.366% ^{15}N.). As we know, ^{13}N and ^{15}O are also positron-emitting radioisotopes whose half-lives are about 10 minutes and 2 minutes respectively. These byproducts will interfere with the activity measurement of $^{11}CO_2$ or ^{11}CO. Another problem is that the use of excess oxygen can cause unnecessarily rapid oxidation of the zinc powder, resulting in the possibility of $^{11}CO_2$ "breakthrough" [Cla75]. If the purity of the target gas ^{14}N is 99.99 percent, it should preferably contain not more than 0.2 percent oxygen [Pow03, Pow00].

For the production of ^{11}C, it was found that much of the activity was lost on the internal surface of the chamber wall if there was not “sufficient” oxygen in the reaction chamber [Van83]. A little oxygen in the reaction chamber can help to radiolytically process the produced radionuclide ^{11}C into $^{11}CO_2$. In our production system, before transferring the oxygen-free nitrogen (99.99%) into the target chamber, the target and processing system were pumped using a rotary pump which can achieve a base pressure of around 0.1 mbar, but the pressure gauge was unable to measure accurately pressures below a few mbar. The pressure gauge used was not sensitive to the pressure measurement in the target holder. A more sensitive pressure gauge will be necessary in the future. In any case, it was impossible to achieve a very high vacuum level using the pumping equipment available. This meant that it was just possible to keep the pressure value in the chamber as low as possible. After we obtained a suitable vacuum level (assumed to be 0.1 mbar) in the chamber, we were able to transfer the oxygen-free nitrogen (99.99%) into the target holder. In reference [Pow00], the researchers found that the use of completely pure N_2 also resulted in a significant yield of $^{11}CO_2$. The reason for this phenomenon is possibly from the trace residual oxygen in the pure N_2 or the chemical reaction of ^{11}C with the oxygen atoms originally existing on the wall surface of the target chamber [Pow00]. We were using 99.99% nitrogen as our target gas. The oxygen gas could exist among the remaining 0.01% and the original residual oxygen after pumping also existed in the target holder. These two sources of oxygen could contribute a considerable oxygen supply for the combination with ^{11}C. Nevertheless, if we need a more precise composition for oxygen, carbon dioxide, carbon monoxide and nitrogen in the target before bombardment, some sort of gas analyzer to justify the percentage of gases in the target chamber will be necessary.

2.3.2 Side reactions in the target

There are six major side reactions which appear when the main reaction is taking place. The cross-sections of the $^{14}N(p,n)^{14}O$ reaction [Noz81] and the $^{16}O(p,\alpha)^{13}N$ reaction [Saj86] are lower than that of the $^{14}N(p,\alpha)^{11}C$ reaction [Bid80]. This means that ^{11}C is produced in higher yields than the other two isotopes. From the reference [Bid80], it is concluded that the production yield of ^{11}C by the $^{14}N(p,\alpha)^{11}C$ reaction is much higher than the ^{14}O produced by the $^{14}N(p,n)^{14}O$ reaction. ^{13}N, ^{14}O and ^{15}O must be completely removed if ^{11}C is to be utilized for the purpose of imaging. In order to decrease the ratio of signal-to-noise when counting, the usual way is to let these isotopes decay for 10 minutes before counting begins. By this means, the activities of ^{13}N, ^{14}O and ^{15}O can be reduced. Six side reaction formulae and their half-lives are listed below (2.13～2.15).

$$^{14}N(p,d)^{13}N,\ \ ^{16}O(p,\alpha)^{13}N,\ \ t_{1/2}=10\ mins \tag{2.13}$$

$$^{14}N(p,n)^{14}O,\ \ t_{1/2}=70.6\ s \tag{2.14}$$

$$^{14}N(p,\gamma)^{15}O,\ \ ^{15}N(p,n)^{15}O,\ \ ^{16}O(p,d)^{15}O,\ \ t_{1/2}=122.2\ s \tag{2.15}$$

2.3.3 Production yields in the target

To increase the production yields in the gas target chamber is sometimes important for the purposes of different experiments. For the $^{11}CO_2$ produced in the aluminum chamber at Birmingham, there are several factors which can affect the final yields. These factors include the internal shape of the target holder, the pressure in the target holder, the proton beam intensity, the gas flow condition in the target chamber and the ambient temperature of the target holder. The internal shape of the target holder we were using (Figure 2.9) was not a hollow cylindrical structure. It was a hollow conical shape 300 mm in length. The proton beam firstly transited through two entrance foils with a smaller diameter, then the beam entered this hollow conical chamber. In one reference [Van83], it was suggested that this conical shape can help the production of ^{11}C. Concerning the pressure value in the target holder, we did not make a suitable assessment. However, if it was desirable to increase the yield of $^{11}CO_2$, increasing the pressure (adding more N_2) and the beam intensity can both be helpful. For the gas flow condition in the target holder, the increase in beam penetration as related to the tabulated particle range was found to be higher in a gas target irradiated under flow-through conditions than under static conditions [Hes87]. This means that under flow-through conditions in the gas target, more reaction opportunities occur. With regard to the ambient temperature of the target holder, this factor can affect the N_2 numbers per unit volume in the reaction chamber and can thus influence the production yields.

Using this $^{14}N(p,\alpha)^{11}C$ reaction, the low yields for the production of $^{11}CO_2$ by the proton bombardment of nitrogen gas might be due to two main factors. Firstly the scattering happened when the proton beam transited through the entrance foils of the target holder. This effect can decrease the beam intensity. Secondly the reduction of the gas density occurred due to heating by the beam. This effect can decrease the reaction opportunity between the proton and ^{14}N.

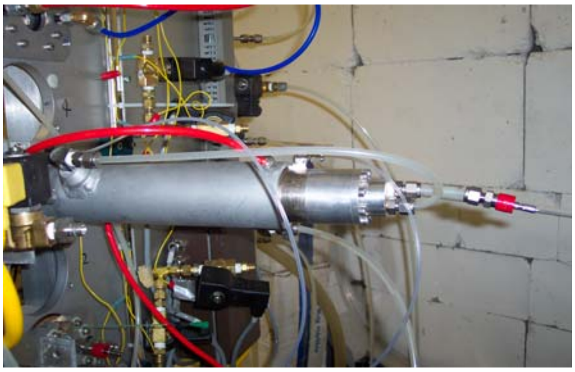

Figure 2.9: Target system

We can conduct a mathematical description for the production yields in our target system using some of the possible parameters involved. If the gas pressure in the target is 5 atm and the ambient temperature is 298 K, the number of nitrogen atoms per cubic centimeter can be calculated as equal to 2.5×10^{20} atoms/cm^3. The gas target can be regarded as a thin target when we desire only to calculate its production yields. As described in section 2.1.2 above, dealing with thin targets, the reaction rate R is equal to $I_{intensity}\times n\times t\times\sigma$. If the incident proton intensity is 1 μA～$6\times10^{12}s^{-1}$, the target length is 30 cm and the average cross section is 100 mb; combined with the above four variables I, n, t, σ, we find that the reaction rate R (saturated activity) is equal to 4.5×10^9 Bq (～122 mCi). Thereby the production yield is found to be 122 mCi per μA. We may make a comparison for this theoretical value with the production yields in the reference [Van83]. In this paper, the researchers wanted to find the optimal production of $^{11}CO_2$ by proton irradiation of nitrogen gas. The N_2 target in their system had a gas pressure of 10 atm and was irradiated with 18.0 MeV protons. The production yield of ^{11}C was found experimentally to be equal to $(83.3 \pm 3.7)10^{14}$Bq/A or (225 ± 10 mCi/μA) at saturation [Van83]. Due to the different parameters and different target chambers in our system and theirs, we did not expect to have the same production yield in our target experiment. However, as can be seen from the unit of production yield, ideally we were able to increase the activity production by increasing the proton intensity.

If one is interested in the energy loss of the proton beam in the target chamber, a program called TRIM (the Transport of Ions in Matter) can be used to assess the residual energy when the proton reaches the back of target. This program can be downloaded from the website: www.srim.org. TRIM can calculate both the final 3D distribution of the ions and also all kinetic phenomena associated with the ion's energy loss [Zie85]. For example, if the gas pressure is 5 atm in the target chamber and the ambient temperature is 298 K, the gas density is equal to 0.00572 g/cm^3. If the incident proton energy used in our system is 16 MeV, by comparing with the result of TRIM assessment in which the particle range is equal to 3.9 mm under 16 MeV of incident proton energy and 0.81 g/cm^{3}gas density, we can evaluate the proton range under 16 MeV of incident proton energy and 0.00572 g/cm^3 gas density. The proton range under our target system can be found to be equal to (0.81/0.00572)×3.9 mm=550 mm. As we know that the length of target used was equal to 300 mm, we can use TRIM to inversely assess the incident proton energy needed to pass the range 250 mm. We can find this by calculating 250×(0.00572/0.81), which is equal to 1.77 mm. By comparing this with the result of TRIM assessment, we can calculate that 10 MeV may be needed to have this range. Thereby we can conclude that with a 300 mm long target chamber, 16 MeV incident proton energy and 5 atm gas pressure, the proton beam may lose 6 MeV during the passage of target gas and reaches the back of target with a residual energy 10 MeV. Since in Figure 2.2 the maximum cross-section occurs below 10 MeV, this suggests that increased yields can be achieved using a lower incident proton energy. For the purpose of testing the Chemical Processing System, only low activity was required. Most runs used 0.5 μA, 16 MeV and the target was irradiated for only 5 minutes.

2.3.4 Chemical Processing System (CPS)

The Chemical Processing System (CPS) (please see Figures 2.11 and 2.12) is adapted from a commercially manufactured item which was packaged with the cyclotron. It was designed to reduce the $^{11}CO_2$ into ^{11}CO. Though it was designed for use with the cyclotron, we changed its layout largely in order to meet our needs in practice. Figure 2.12 shows the new layout which we designed and built. From the console station of the cyclotron, we could control the inlet and outlet of the radioactive gas by automatic remote operation. As a reductive agent to transform the $^{11}CO_2$ into ^{11}CO, zinc powder was put into a quartz tubing which was located in an oven at a temperature of 393 °C. After the preliminary product $^{11}CO_2$ was produced, valve 17 (V17) (please see Figure 2.12) was opened to let the radioactive gas $^{11}CO_2$ and the residual nitrogen gas flow through into the liquid nitrogen trap. Most of the $^{11}CO_2$ was trapped inside the spiral stainless steel trap in the LN_2. The residual nitrogen gas flowed through V16 (Figure 2.12) into a reservoir.

The trapping technique for $^{11}CO_2$ (with a boiling point of 195 K) is important for the following radiochemical steps. If the trapping efficiency for $^{11}CO_2$ is low, it will affect the concentration of the final product. In reference [Moc95], one research group employed carbon molecular sieves to adsorb the $^{11}CO_2$ selectively from the gas target at room temperature. This trapping technique requires no liquid nitrogen cooling but the residual N_2, O_2, CO, NO and moisture from the target are not retained in this trap. The adsorbed $^{11}CO_2$ could be recovered quantitatively by thermal desorption. The efficiency of this solid-phase reversible trap was > 99%. For our cryogenic trap, it was better to use liquid argon (with a boiling point of 87 K) as the cooling liquid, because the main residual gas from the target is N_2 which could probably be trapped together with the $^{11}CO_2$ when the cooling liquid is LN_2 (with a boiling point of 77 K). However the liquid argon is much more expensive than liquid nitrogen and therefore liquid nitrogen is normally preferred as the cooling liquid despite the possibility of the residual N_2 gas being trapped as well.

Before flowing into the liquid nitrogen trap, the preliminary product $^{11}CO_2$ was transferred through a Mass Flow Regulator (MFR, Brooks Instruments). This mass-flow controller is factory set to a pre-selected gas, pressure and flow range. N_2 gas is pre-set for factory use. The accuracy of the flow rate of the new gas is generally within 3% of the calculated flow rate at any output based on the factory estimation. To know the flow rate for any new gas, we need to multiply the output reading by the ratio of the factor of the new gas to the factor of the calibration gas. The following formula (2.16) is based on that in the factory's manual.

$$Estimated\ gas\ flowrate = Output\ reading \times \frac{factor\ of\ new\ gas}{factor\ of\ calibrated\ gas} \tag{2.16}$$

In our experiments, we were using two mass-flow controllers in the CPS. One controller was at the target's outlet and the other was at the entrance to the oven. The mass-flow controller is factory-set to calibrate to N_2. The new gas in our experiment was $^{11}CO_2$ whose gas factor is 0.77 as set in the factory. Therefore, if the output reading is 75 ml/min, the estimated flow rate for $^{11}CO_2$ is 75×0.77/1=57.75 ml/min. Unfortunately, according to the real measurement of the flow rate, the actual flow rate in these two flow controllers was not consistent with the estimated value. The measured result was quite different even with the 3% error explanation in the factory's manual. The flow rate figure below (Figure 2.10) indicates the relationship between the actual measured flow rate and the output reading of the mass-flow controller. Figure 2.10 is plotted using the flow rate of $^{11}CO_2$. As we knew the volume of the target chamber (～380 cm^3), every time we filled the target chamber with the $^{11}CO_2$ produced, we could turn on valve 17 and let the $^{11}CO_2$ gas flow through the MFR which could be adjusted to different values for every separate inflow of $^{11}CO_2$. As can be seen from Figure 2.10, the MFR values were chosen and adjusted to 30, 60, 120, 145 for each inflow of $^{11}CO_2$. We could measure the total time taken by the $^{11}CO_2$ to flow out of the target chamber on the basis of the pressure change (for example, in the reaction chamber ideally from 5 atm to 0 atm) shown on the pressure reading of the control panel. Thereby the flow rate of $^{11}CO_2$ flowing through the MFR could be found using the chamber volume divided by the total time taken for $^{11}CO_2$ to leave the chamber. The linear regression in Figure 2.10 suggests that the flow rates for $^{11}CO_2$ flowing through MFR should be equal to 11.5 ml/min, 17.1 ml/min, 28.1 ml/min and 32.7 ml/min, based on the MFR values at 30, 60, 120, 145 respectively.

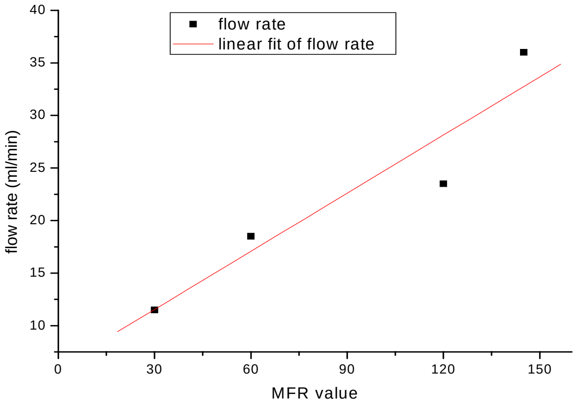

Figure 2.10: Measured flow rate

It is better to warm the trap before opening the valves between the trap and the oven. The trap was removed from the liquid nitrogen into the air for nearly 3 minutes. This warming-up period was able to increase the pressure before valve V1 and, when opening the connection valves, the flow appeared to move at a higher speed through the oven. We could verify this from the meter reading of the MFR at the panel of the control station.

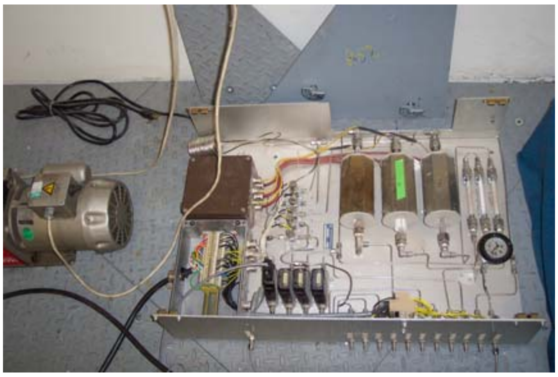

Figure 2.11: Chemical Processing System (CPS)

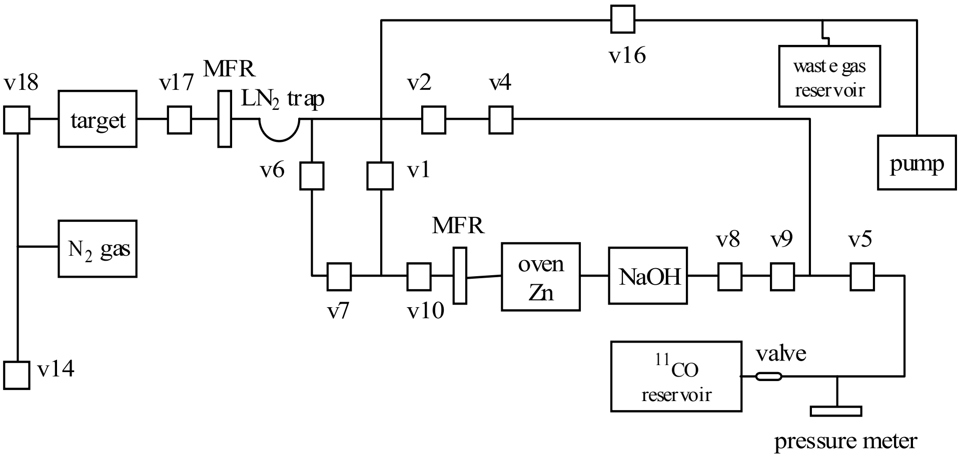

Figure 2.12: Schematic of CPS for practical use

An important concept is the possible use of carrier gas to enable $^{11}CO_2$ and ^{11}CO to flow along the CPS system. The carrier gas can be any inert gas which does not react with the inner material of tubing and the produced radioactive gases. Gases such as helium, argon and nitrogen can all be used as the carrier gas to assist the flow of $^{11}CO_2$ and ^{11}CO. As helium gas is very expensive, the most popular carrier gas is normally nitrogen. However, due to the practical operational condition in our system, we did not in the end use any carrier gas to help the transportation. Even without nitrogen to assist the flow, however, the produced $^{11}CO_2$ could flow well into the oven and the final product ^{11}CO could also flow smoothly into the reservoir. In section 3.2.1, it may be seen that the carrier gas was eventually used to assist transportation, since the distance between the ^{11}CO reservoir and the red cells labelling system was more than 10 m.

In using the CPS system, the leakage test was very important. We needed to make sure that the radioactive gas could not be released into the space where we were working. The main leakage came from the connection points of the steel and plastic tubing. We found a special leak from the MFR regulator, where it was especially easy for the connection with the tubing to be loose. As the actual measured flow rate and the output reading of MFR were different, it seems doubtful whether the leakage in the MFR was responsible for the difference. However, as a very careful leakage test was executed before running this CPS system, there was only a very slender chance for the leakage in MFR to have been responsible for the difference in the flow rate measurements.

2.3.5 Pressure in the CPS

The pressure level in the CPS tubing was important for the movement of $^{11}CO_2$ and ^{11}CO which flowed through the tubing within this system. We needed to achieve as low a pressure value as possible in the tubing before opening valve 17 to let the $^{11}CO_2$ gas flow out of the reaction chamber. Normally the pumps spent many hours on decreasing the pressure values in the tubing. Figure 2.13 below describes the pressure-time relation when pumping was taking place. A curve has been fitted to the experimental data in the figure. After 30 hours of pumping, the pressure value was nearly 30 mbar. This value seemed to be a pressure barrier for this system. As can be seen from Figure 2.13, the 30 mbar remained constant over 20 hours of pumping. As the outgassing from the inner surfaces in the steel and plastic tubing and in particular from the NaOH and zinc powder may have contributed to the pressure level inside the system, the equilibrium between the gas release and the pumping was likely to have been reached at something like the 30 mbar barrier. After 30 hours of pumping, however, the pressure began to reduce. It took a further 4 hours to reach 9 mbar. We found that the pressure value in the CPS system could go down to 7 mbar shown on the pressure meter reading and this value could be maintained without pumping for 10 minutes. As we believed there was a zero offset in the pressure gauge, the actual pressure value was probably lower than 7 mbar.

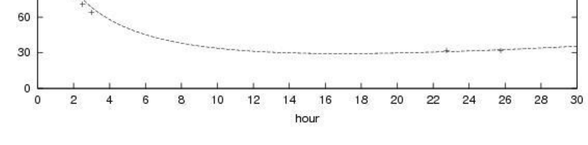

Figure 2.13: Pressure-time relation in the CPS

2.3.6 Reduction of $^{11}CO_2$

The oven was designed to have a hollow space within it where a quartz tubing could be heated. The zinc powder weighing about 12 mg was put into this quartz tubing. Silica wool was used as stoppers at each end. The 12 mg zinc powder should fill the space completely so that all of the $^{11}CO_2$ could have a reduction reaction with the zinc powder. If the zinc powder filled the tube very densely, this denseness could probably affect the flow rate and the reduction reaction for the $^{11}CO_2$. The melting point of zinc powder is 419 °C (its boiling point is 907 °C). The temperature in the oven was set at 393 °C, which was suitable for the reduction reaction. Granular zinc metal is harmful if swallowed or inhaled and may affect the central nervous system, kidneys, or blood. Direct contact with zinc powder may cause irritation to the skin, eyes and respiratory tract. When handling this metal powder, care was taken to have no direct contact with it. The reduction reaction may be seen below (2.17).

$$^{11}CO_2+Zn \xrightarrow{393\,^{\circ}C} ZnO+{}^{11}CO \qquad (2.17)$$

^{11}CO was produced by a reduction of $^{11}CO_2$ on zinc heated at 390ºC. Reference [Iwa81] suggests that a prolonged use of zinc tends to reduce the yield of ^{11}CO, and in the end to result in the complete oxidation of the zinc surface. Therefore fresh zinc should be used on every run. However, even with the use of fresh zinc each time, the conversion efficiency for zinc powder was only around 50% [Iwa81]. To find a better way to improve the conversion efficiency for $^{11}CO_2$ reduction to ^{11}CO is an important issue. In reference [Roe04], a method of a rapid, almost quantitative conversion of $^{11}CO_2$ into ^{11}CO via [^{11}C]formate and [^{11}C]formyl chloride is introduced. In reference [Zei97], one research group used molybdenum as the reductive agent to reduce the $^{11}CO_2$ to ^{11}CO. The molybdenum was put into a quartz tube, which was kept at an optimum reaction temperature of 850ºC. A maximum radiochemical yield of 81% was measured when this method was used. If higher conversion efficiency can be reached using the methods mentioned above, then more ^{11}CO is produced and thus a higher concentration in the final sample.

Magnesium perchlorate can be used to pre-dry high-purity nitrogen before the bombardment of proton beam and can remove traces of water after obtaining $^{11}CO_2$. However, this experiment made no use of this valuable compound. A sodalime absorber was used to absorb a trace of unconverted $^{11}CO_2$ at the furnace output. Particular care had to be taken to ensure that the target gas was not contaminated with CO_2 and CO. As mentioned in section 2.3.1, they could not be chemically separated from the desired $^{11}CO_2$ and ^{11}CO.

The energetic protons bombarded the target gas ^{14}N (99.99%) and produced the $^{11}CO_2$ compound in the reaction chamber. After passing through the zinc powder and the sodalime absorber, the final product ^{11}CO flowed through V8, V9, V5 and finally into a reservoir. A simple labelling system (please see Figure 3.9) could be connected to this reservoir, which was full of ^{11}CO. Before flowing into the reservoir, we had installed a pressure meter to indicate the pressure value with which we could compare the discrepancies for the reservoir's storage of ^{11}CO each time. We used only an evacuated aluminum reservoir to store the produced ^{11}CO, but this was not a suitable container, as some ^{11}CO could be deposited on the inner surface of the aluminum wall. In reference [Zei97], one research group reports using a silica trap cooled with liquid argon to capture the ^{11}CO. In reference [Hos02], another research group used carbon molecular sieves cooled in a dry ice/isopropanol bath to trap the ^{11}CO. These two methods of capturing ^{11}CO are suitable for future reference.

We could also use activated charcoal at 1000 °C as a reduction reagent. But a serious problem in using activated charcoal is that stable CO will be produced at the same time. This is not a desirable result when doing the labelling with the red blood cells. This reduction reaction may be seen below (2.18).

$$^{11}CO_2+C \xrightarrow{1000\,^{\circ}C} CO+{}^{11}CO \qquad (2.18)$$

2.4 Measuring the produced ^{11}CO

The efficiency of CPS for producing ^{11}CO can be simply indicated by using the radiation monitor to compare dose rates from different parts of this system. The radiation monitor had shown that most of the activity was in the ^{11}CO reservoir but there was some also in the NaOH trap and some in the waste gas reservoir. This result, detected by the radiation monitor, was basically the same on every run of the production of ^{11}CO. As some of the produced ^{11}CO could be deposited on the inner surface of the ^{11}CO reservoir, this phenomenon could reduce the available activity. In order to identify and investigate the produced ^{11}CO, we used a NaI(Tl) scintillation detector to make the relevant measurements. Some fundamental properties of the scintillation detector are first described (see sections 2.4.1 and 2.4.2, below).

2.4.1 Scintillation detector

The energies of common radiations can be as low as a fraction of an eV (a slow neutron) or up to the GeV level (cosmic rays). For measuring the interactions between radiations and detectors, it is the ionization process which forms the basis for most detector systems. A common scintillator detector consists of a crystal and a PMT tube. Inorganic scintillators are the most common detector materials used in positron emission tomography, due to their high efficiency with 511 keV gamma-rays and good coincidence resolving time. Most applications ask the same properties from a scintillator: high density and atomic number, high light output, short decay time without afterglow, suitable emission wavelength, mechanical ruggedness, radiation hardness and low cost. The table below (Table 2.4) shows three main scintillation crystals used in PET imaging.

Parameter(*at 511 keV)	NaI(Tl)	BGO	LSO
Effective atomic number	51	75	66
Density(g/cm^3)	3.67	7.13	7.4
Decay time(ns)	230	300	48
Light output [NaI(Tl)=100]	100	15	75

Table 2.4: Properties of main scintillators. Data from [Eij02]

Three parameters are often mentioned in characterizing the various types of detector: efficiency, resolution and dead time. Scintillators can provide detectable photons in the visible part of the light spectrum after a photon or charged particle has passed through it. Because the intensity of the emitted scintillation light is very low, the signal is amplified by using a PMT (photomultiplier tube) which will convert a weak photon signal to a detectable electric pulse. When the gamma-rays enter the scintillator, they can interact with this scintillator through the Photoelectric effect, Compton scattering or e^+e^- Pair production. The incident photon then produces a photoelectron directly or soon after undergoing one or more Compton scatterings to produce a photoelectron. The scattered photons can escape from the crystal directly or push out a photoelectron.

The incident photons may escape altogether, meaning that the detector does not detect them at all. Or, after one or more Compton scatterings, these scattered photons escape from the crystal. The total energy of incident photons is equivalent to the total escape energy plus the total deposited energy. The final electrical signal is proportional to the light output, which is also proportional to the deposited energy. In other words, there is a linear energy response in which the constant of proportionality between the light yield and the deposited energy should be independent of the incident photon energy. We can make some assumptions to calculate the numbers involved in the light output. If the light conversion efficiency of a detector is 6%, the energy of the incident γ-ray is 1 MeV, and the average energy of the produced scintillation lights is 2 eV, we can obtain (1 MeV/2 eV)×0.06=30,000 photons for the light output.

A commonly used inorganic scintillator is NaI which is usually doped with the activator Tl. An activator can be excited by electron-hole pairs produced by incident gamma-rays in the crystal lattice and then be de-excited by photon emission. NaI has become the standard scintillator material for gamma-ray spectroscopy. A PMT is attached to the opposite side of the crystal through a light pipe or directly.

2.4.2 Electronics for a scintillation detector

Basically, a scintillation detector system includes the crystal, PMT tube, preamplifier, amplifier, SCA, MCA and a computer. A PMT tube consists of several components. The scintillation photons will firstly enter a semitransparent material, which is called the photocathode. The valence electrons are weakly bound in this material. When the scintillation photon hits the valence electron, this electron will be pushed out via the Photoelectric effect. The scintillation photons striking the photocathode will release many electrons, which will enter the tube in which a series of dynodes will multiply these electrons to the anode (electron collector). There are typically 6~14 dynodes in PMT and a total gain is in the range of 10^4~10^7. The signal from the anode is linearly proportional to the amount of photon incident on the photocathode. A straightforward mathematical formula below (2.24) can be devised for the above phenomenon. There are several parameters in the formula (2.19) where m means the number of photons produced in the crystal; k means the optical efficiency of the crystal; l means the quantum efficiency of the photocathode; n means the number of dynodes; R means the dynode multiplication factor; and e means the elementary charge. For a 0.1 MeV gamma-ray, typically, $m = 1000$, $k = 0.5$, $l = 0.15$, $n = 10$, $R = 4.5$. Therefore, Q could be calculated as 41×10^{-12} C. This value is very small and hence a very sensitive amplifier is needed.

$$Q = m \times k \times l \times R^n \times e \ \textit{(the charge collected at the anode)} \tag{2.19}$$

A basic set-up for a detection system is shown in Figure 2.14 below. The amplifier output is connected to a multi-channel analyzer (MCA) to obtain an energy spectrum or to a single-channel analyzer (SCA) to count a single energy radiation. A discriminator is an electronic circuit which can be set to accept certain preset amplitudes. A lower level discriminator (LLD) can set the lower limit of amplitude; an upper level discriminator (ULD) can set the upper limit. The simple device to discriminate amplitude level is called a single-channel analyzer (SCA). The number of pulses which pass through the SCA can be recorded by a scalar which is connected to the SCA. The analog-to-digital converter (ADC) is used to transform the analog signals into the digital data from the amplifier. These digital data will be stored in the histogramming memory, in which every incoming pulse is sorted into its proper channel. Every channel represents a specific range of particle energies. The combination of the ADC and the histogramming memory forms a multi-channel analyzer (MCA). The basic function of the MCA involves only the ADC and the memory. We can imagine the histogramming memory as a vertical stack of addressable locations, ranging from the first address (or channel number 1) at the bottom up to the maximum location number (say,1024) at the top. A computer is connected to the MCA to display the spectrum. In a typical pulse height spectrum, the vertical axis represents the count numbers and the horizontal axis represents the channel numbers or corresponding energies.

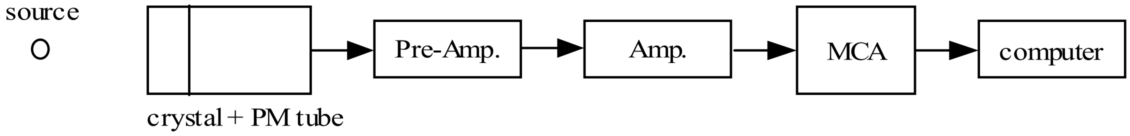

Figure 2.14: Schematic of a standard scintillation spectrometer set-up

2.4.3 Decay mode of ^{11}C

The decay mode describes the specific way in which a particle decays. From the Q calculation for positron-emitting nuclides described in Chapter 1, it will be seen that there is always an energy fall of $2m_ec^2$ =1.022MeV in the nucleus before the positron is emitted. For carbon-11, 99.76% will decay through the positron's emission and 0.24% will decay through the electron capture. The decay mode for ^{11}C is shown in Figure 2.15.

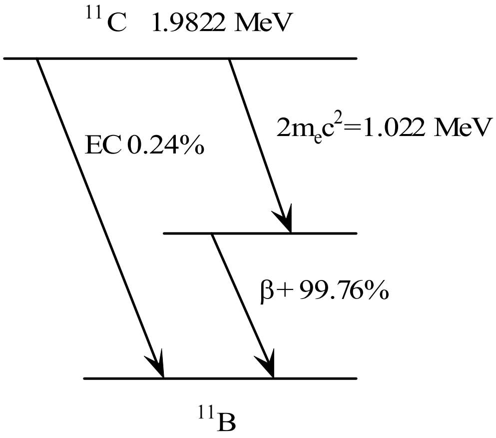

Figure 2.15: ^{11}C decay mode

When there are too many protons in the nucleus, and not enough energy to emit a positron, an inner-shell electron may be captured by one proton in the nucleus. This phenomenon is called the electron capture (EC) which will produce a neutron in the nucleus and emit a nutrino from the nucleus (please see formula 2.21). If the energy difference between the parent and the daughter atoms is less than 1.022 MeV, the positron emission is prevented and the electron capture is the major mode of decay. The decay formulae 2.20 and 2.21 for ^{11}C are shown below.

$$^{11}C \rightarrow {}^{11}B + e^{+} + v_e \tag{2.20}$$

$$^{11}C + e^{-} \rightarrow {}^{11}B + v_e \tag{2.21}$$

where B is the element boron, e^+ is the positron, e^- is the electron and v_e is the neutrino.

2.4.4 Verification of ^{11}CO

According to $A=A_0 \times e^{-\lambda t}$, the value of λ for carbon 11 can be precisely calculated and this value is found to be ~$5.67\times10^{-4}s^{-1}$. The experimental decision to find a λ value for ^{11}C was reached as follows. We had chosen five separate time points to count the disintegrations from ^{11}CO, using a NaI (Tl) scintillation detector. The five time points were at time=0, 600, 1200, 2400 and 3600 seconds. For each time point, the counts were measured for 10 seconds to accumulate the disintegrations from ^{11}CO. Using our NaI(Tl) scintillation detector and a SCA system, five count values were found. Through the calculations for the activities and a transformed formula, $\ln A=\ln A_0-\lambda t$, we were able to find a linear relationship between lnA and time. Figure 2.16 shown below illustrates our experimental fitting for the λ. As a linear fitting for these five points, the λ value is equal to $5.88\times10^{-4}s^{-1}$, which is close to the theoretical value $5.67\times10^{-4}s^{-1}$.

Some factors which could affect the measurement of relative activity should be noticed. A fixed set-up was important in counting the photons impinging on the window. If the distance between the source and the detector was not constant, the comparison of relative activity had lost its accuracy. Precise timing was also vital.

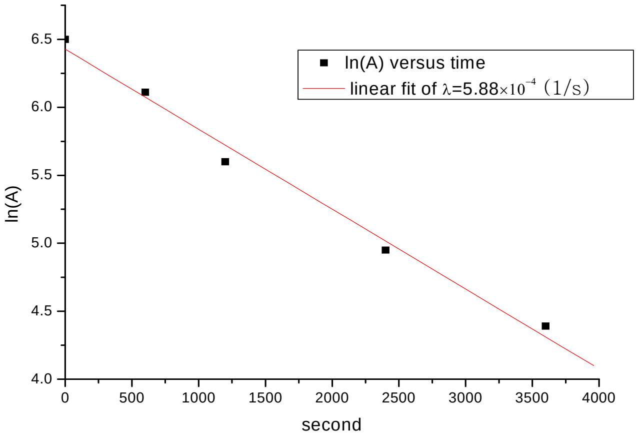

Figure 2.16: Five time points in measuring λ

2.4.5 Activity of ^{11}CO

In Figure 2.12, it will be seen that we did not set up an activity measurement system around the reservoir of the produced ^{11}CO. Instead, we set up an activity measurement system in the labelling system (please see Figure 3.9) in which a storage vial inserted into the well of an ionization chamber received the incoming activity from the ^{11}CO reservoir. It took probably 20 minutes to reach 1 mCi, which was the meter reading of the ionization chamber. This value, 1 mCi, was the maximum we had measured using the practical apparatus.

It is usual to measure the activity of a radionuclide in the lab by using an ionization well chamber. However, a NaI(Tl) scintillation detector or a HPGe detector may also be adopted for this purpose. We could also use a pair of face-to-face NaI(Tl) scintillation detectors which are attached with a coincident circuit to measure the activity. The ADAC Forte dual-headed gamma camera could be used to measure the activity of ^{11}CO as well. Further details about the use of a single scintillation detector to measure the activity may be useful at this point.

Basically, it is possible to measure the activity of a point source using a NaI(Tl) scintillation detector. However the main problems related to the final activity value apply to the detector peak efficiency and geometric acceptance. The formula is shown below (2.22).

$$A = \frac{R}{\varepsilon_{peak} \frac{\Delta\Omega}{4\pi} B} \tag{2.22}$$

In this formula (2.22), A is the activity, R is the number of photons detected per time unit and B is the branching ratio for this particular transition. The ε_{peak} is defined as the fraction of photons detected in the full-energy peak relative to the total number of photons impinging on the window (2.23). As a standard method, the value of the ε_{peak} can be determined by several calibrated sources of known intensities.

$$\varepsilon_{peak} = \frac{N_{peak}}{N_{total}} \tag{2.23}$$

The $\Delta\Omega/4\pi$ is the term for the geometric acceptance. The geometric acceptance should be possible to evaluate if the source-detector arrangement is well known. For the simplest arrangement, a point source and a cylindrical detector, the geometrical acceptance can be exactly calculated. However, for a common radioactive source with a finite dimension, the term 'geometric acceptance' becomes mathematically complex and can probably be resolved only by numerical computation using a Monte Carlo algorithm. The equation below is a general form for the geometrical acceptance. $\vec{n}$ is a unitary vector perpendicular to the detector surface. $\vec{r}$ is the vector to link a point source to a detector elementary area dA. For a source with a finite dimension, the integration below (2.24) needs to be evaluated to include all of the source points.

$$Geometrical\ acceptance = \frac{1}{4\pi}\int d\Omega = \frac{1}{4\pi}\int_A \frac{\vec{r}\bullet\vec{n}}{\left|r^3\right|}dA \qquad (2.24)$$

We were using a NaI(Tl) detector to detect the gamma-ray spectra for the positron-emitting radioisotope ^{11}C. By using the detected spectra, if we could find out the geometrical acceptance and the peak efficiency, we could use the above formulae to calculate the activity value. However, in practice, it is not easy to use these formulae to calculate the final activity of ^{11}C under our experimental set-up.

2.4.6 Specific Activity of ^{11}CO

The specific activity (SA) of a sample is defined as its radioactivity per unit mass. The unit of SA can be Bq/mol, Bq/g or Ci/g. In the case of our produced ^{11}CO, if ^{12}CO, which is not radioactive, was present in the sample, this could reduce the SA value of the produced sample. A no-carrier-added (NCA) sample is always the ideal requirement for a radioactive sample.

For the production of ^{11}CO in our system, a major concern was related to how to maximize the SA value. Obviously, if we could acquire 100% of ^{11}CO in the final sample from the production system, the SA value of ^{11}CO gas could ideally reach the maximum (～9200 Ci/μmole). However, it was not in that case in situ.

Some different chemical forms existed together with the final ^{11}CO sample, such as $^{11}CO_2$, $^{12}CO_2$, O_2, N_2 and H_2O etc., and therefore 100% pure ^{11}CO could not be produced in the final sample. In order to reduce the percentage of these unrelated chemical forms in the final gas sample, we used some suitable separation techniques to remove them. For example, to reduce the level of natural CO_2 in the gas used to fill the target, it might have been helpful to pass this gas through a LN_2 before the target (although we did not try this.). In the CPS system, when the $^{11}CO_2$ gas flowed through into the liquid nitrogen trap, the $^{11}CO_2$ gas became dry ice and other kinds of gas, mainly nitrogen, flowed into another waste gas reservoir. Magnesium perchlorate could have been used to remove the traces of water after obtaining $^{11}CO_2$ (although we did not use it.). The probable improvements of the conversion efficiency for reducing $^{11}CO_2$ to ^{11}CO and the absorption efficiency for unconverted $^{11}CO_2$ could also greatly enhance the yield of ^{11}CO and purify the produced ^{11}CO. Some short-lived radioisotopes, such as ^{13}N, ^{14}O, ^{15}O, which were produced together with the ^{11}C in the target chamber, should be allowed to decay for at least 10 minutes before doing the counting for ^{11}CO gas. Moreover, it appeared that we should always pay attention to the vacuum level in the production system.

In reference [Zei97], one research group produced $^{11}CO_2$ with a specific activity～15 Ci/μmole. It used molybdenum as the reductive agent to reduce the $^{11}CO_2$ to ^{11}CO. The molybdenum was put into a quartz tube, which was kept at an optimum reaction temperature of 850 ^{o}C. A maximum radiochemical yield 81% was measured by using this method. This research group used a small silica trap cooled with liquid argon to trap the produced ^{11}CO. This silica trap was eventually removed from the liquid argon vessel and measured in an ionization chamber. The purity was investigated by a radio-gas chromatograph. The specific activity could be measured by releasing the ^{11}CO gas into an evacuated vial of known volume and it was calculated as～8 Ci/μmole. One can divide 8 Ci/μmole by 9200 Ci/μmole (theoretical SA of pure ^{11}CO), which yields the ratio of～0.09%, which also showed the purity of the ^{11}CO in this sample.

A radio-gas chromatograph (radio-GC) method can be used to quantify the different mass peaks and thereby investigate the purity of our produced gas sample. The principle of this method is that the different chemical constituents of a gas sample can pass in a gas stream (carrier gas in a mobile phase in the radio-GC column) at different rates depending on their various physical and chemical properties and their interaction with a stationary phase in the radio-GC column. However, since this instrument was not available, we did not investigate the purity of our produced gas sample.

There is no doubt that if we can completely remove the different chemical forms from the produced sample ^{11}CO, if we can completely delete the contamination of CO_2 and CO in the system and if we can reduce the other activity contributions which are different from ^{11}C, they will be helpful to the radiochemical purity and the SA calculation.

2.4.7 Gamma-ray spectrum of ^{11}CO

X-ray photons have energies in the range 100 eV to 100 keV. Gamma-rays are then all the photons with energies greater than 100 keV. X-rays have so much energy and such a short wavelength that they can go right through the human body. Gamma-rays have very high energy and will even penetrate metals. Gamma-rays and X-rays can cause cancer, but gamma-rays can also be used to destroy cancer cells, in the technique called radiotherapy. Some radioactive materials can produce gamma-rays. Normally, in the laboratory, the Na(Tl) scintillation detector and the HPGe detector can be used to create the gamma-ray spectra. The performance difference between these two kinds of detector is the peak energy resolution. The HPGe detector has a much higher energy resolution.

If a gamma-ray loses all its energy to an emitted electron through the photoelectric effect, this means that it has deposited all of its energy to this scintillator. A gamma-ray interacting through Compton scattering does not deposit all its energy within this scintillator. The scattered photon tends to escape from this crystal. For a low-energy gamma-ray, the effect of pair production is almost impossible. However if the incident photon has a higher energy (>1.022 MeV), the pair production is more likely. The produced electron and positron in the pair production deposit their kinetic energy within the scintillator and finally positron annihilation occurs to produce two 511 keV photons. We can understand the practical meaning of a pulse height spectrum based on the above descriptions of the interactions between the scintillator and the incident gamma-rays. As an example of ^{137}Cs, its pulse height spectrum below (Figure 2.17) illustrates the major characteristics of the interactions in the scintillator.

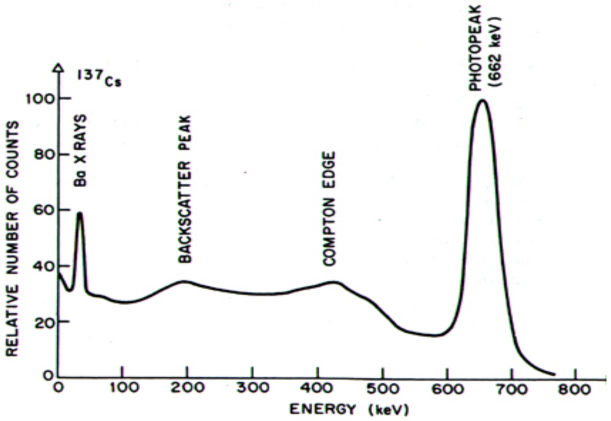

Figure 2.17: A pulse height spectrum for Cs-137. Taken from [Das94]

From the above figure (Figure 2.17), only those gamma-rays that lose all of their energy within the crystal contribute to the photopeak 662 keV. This includes those gamma-rays which undergo the photoelectric effect directly or one or even more Compton scatterings to produce photoelectrons. The Compton continuum distribution is created by the series of recoil electrons in Compton scatterings. The Compton edge 478 keV is created by the most energetic recoil electron via Compton scattering. The backscatter peak is contributed by the scattered photons from the surrounding material. The energy of the scattered gamma-ray at 180° is 662 keV-478 keV=184 keV, which is slightly below the backscatter peak. The relative area under the spectrum curve depends mainly on the size of the crystal. For the pulse height spectrum of ^{22}Na below (Figure 2.18), in addition to the expected peaks at 0.511 MeV and 1.275 MeV, two Compton edge structures are seen in the spectrum as well. Basically through the understandings of the spectra of Cs-137 (Figure 2.17) and Na-22 (Figure 2.18), we could confidently expect a deeper knowledge of the interactions within the scintillator.

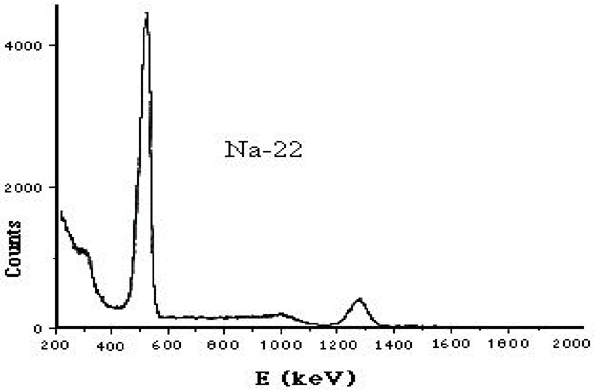

Figure 2.18: A pulse height spectrum for Na-22. Taken from [Kno00]

A pulse height spectrum figure for ^{11}CO measured by our scintillation detector is shown below (Figure 2.19). As expected, its pulse height spectrum has an energy peak at 511 keV; another peak with lower energy is contributed by the scattered photons from the surrounding material. A program named "AttenChn" which could be run under the win32 system was used to decode the Chn file produced from the MCA system of the Ortec Maestro II. This program could transform the Chn files into Microsoft Excel files whereby we could plot any pulse height spectra for some radionuclides.

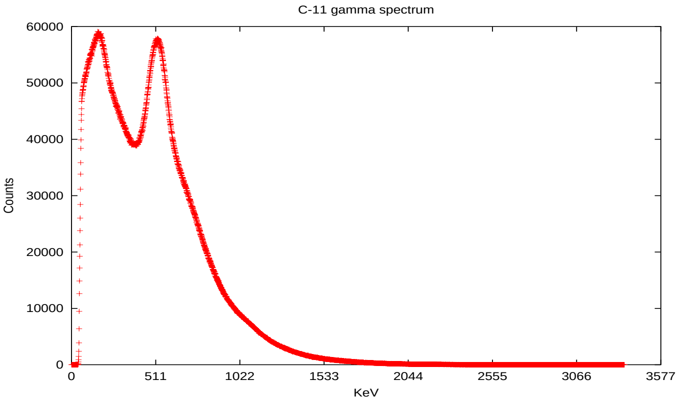

Figure 2.19: A pulse height spectrum for ^{11}CO

2.5 Summary

Due to the experimental limitation in situ, we did not try to measure the activity of trapped $^{11}CO_2$ in the LN_2. Instead, a theoretical estimation of the activity of produced $^{11}CO_2$ in the target is shown in section 2.1.6. I also made a theoretical estimation in section 2.3.3 for the production yield in the target of our own system.

This theoretical value was found to be equal to 122 mCi/μA, which could be compared with an experimental value of 225 mCi/μA [Van83]. A theoretical estimation for the energy loss of proton beam in the target chamber is also shown in section 2.3.3.

I made some calculations in section 2.3.1 to find the probable amount of individual residual gases (O_2, CO_2 and CO) in the target after pumping and the probable amount of individual residual gases (O_2, CO_2 and CO) after filling the high-purity nitrogen. The mole ratios of CO_2 to ^{11}C and CO to ^{11}C after bombardment in the target and the total oxygen percentage before bombardment in the target are shown in section 2.3.1. The results of these calculations are helpful for understanding the probable distribution of residual gases in the target and their effects on the following radiochemical steps. Due to the limited capability of our pumping system (only 0.1 mbar) and the poor pressure meter used (only several mbar), we could not fully ensure the vacuum level in the target and in the CPS system. The only remedy we had was to extend the pumping time and to avoid any leakages in the target and in the CPS system. As the vacuum level in the CPS system could probably reach 0.1 mbar (although section 2.3.5 only says that it should be lower than 7 mbar), the originally existing CO_2 and CO in the CPS system (before processing the $^{11}CO_2$ from the target) should not greatly have affected the following radiochemical steps.

Most of ^{11}C produced was apparently in the form of $^{11}CO_2$ (trapped in LN_2) and would then have been reduced to ^{11}CO. As the conversion efficiency for zinc powder was only around 50% [Iwa81], to find another method to improve the conversion efficiency of $^{11}CO_2$ reduced into ^{11}CO was important. As mentioned in section 2.3.6, other researchers [Roe04] employed the method of rapid, almost quantitative conversion of $^{11}CO_2$ into ^{11}CO via [^{11}C]formate and [^{11}C]formyl chloride, and in reference [Zei97], it used the molybdenum as the reductive agent to reduce the $^{11}CO_2$ to ^{11}CO. The molybdenum was put into a quartz tube which was kept at an optimum reaction temperature of 850°C. A maximum radiochemical yield 81% was measured by using this method.

The trapping techniques for $^{11}CO_2$ and ^{11}CO were important. As mentioned in section 2.3.4, in reference [Moc95], a solid-phase reversible method was employed to provide a trapping efficiency of more than 99% for the produced $^{11}CO_2$. As described in section 2.3.6, in reference [Zei97], a silica trap cooled with liquid argon was used to trap the ^{11}CO, and in reference [Hos02], the carbon molecular sieves cooled in a dry ice/isopropanol bath was employed to trap the ^{11}CO. A higher trapping efficiency could naturally attain a higher concentration of the final product. The above-mentioned methods to trap the $^{11}CO_2$ and ^{11}CO are suitable for future reference.

As mentioned in section 2.4.6, in the reference [Zei97], the research group which employed molybdenum as the reductive agent to reduce the $^{11}CO_2$ to ^{11}CO produced $^{11}CO_2$ with a specific activity～15 Ci/μmole. A small silica trap cooled with liquid argon was used to trap the produced ^{11}CO. This trap was eventually removed from the liquid argon vessel and measured in an ionization chamber. The purity was investigated by a radio-gas chromatograph. The specific activity could be measured by releasing the ^{11}CO gas into an evacuated vial of known volume and it was calculated as～8 Ci/μmole. One can divide 8 Ci/μmole by 9200 Ci/μmole (theoretical SA of pure ^{11}CO), which produces a ratio of～0.09%, showing the purity of the ^{11}CO in this sample. As described in section 1.5, if we had had a SA～8 Ci/μmole for the produced ^{11}CO, in theory that would have meant that the expected maximum activity of a labelled red cell would have equaled only 15 μCix(8/9200)～13.5 nCi. Under the current PEPT technique, normally a tracer with 0.3 mCi can give approximately 13000 events per second. Thereby a tracer with 13.5 nCi could give $13000\times(13.5\times10^{-9})/(0.3\times10^{-3})$～0.6 events per second from the ADAC Forte. However, I only assume we achieved a SA～8 Ci/μmole. Based on the experimental results from other research groups, the experimental SA value of produced ^{11}CO can reach 18 Ci/μmole. Thereby in theory it is still possible to have a higher data rate for tracking purposes. And using detectors with higher efficiency could also increase the data rate.

In this study we used a LN_2 technique to trap the produced $^{11}CO_2$, but used only an evacuated aluminum chamber to store the produced ^{11}CO. The problem with this reservoir was that the ^{11}CO gas was easily deposited on the inner surface of the aluminum wall and then lost some activities for practical use. Moreover, the reservoir was so big that anyone who wanted to directly measure its activity by using a scintillation detector would meet many uncertainties. A better way to avoiding this problem is to use a small silica trap which can be inserted into an ionization chamber. To calculate the SA value, one could then release the ^{11}CO gas from the small silica trap (which is removed from the liquid argon) into an evacuated vial of known volume. Due to the trapping problem with ^{11}CO (no suitable trapping technique for ^{11}CO was used) and the lack of a radio-GC, I was not able to investigate the purity of the produced ^{11}CO and to measure its specific activity ($^{11}C/^{12}C$ ratio). However some factors affecting the SA value and some improvements for maximizing the SA are shown in section 2.4.6. In section 3.2.1, a storage vial of known volume for ^{11}CO was inserted into an ionization chamber. I was able to estimate the SA value by using the measured maximum activity value (1 mCi) divided by the calculated gas moles. The estimated SA value was～0.714 μCi/μmole. However as a great deal of carrier gas N_2 was mixed together with the transported ^{11}CO in the storage vial, the calculated SA value was not accurate.

Chapter 3

Labeling red blood cells (RBCs) with ^{11}CO

3.1 Introductory RBC

Blood is a liquid tissue. Suspended in the watery plasma are red blood cells (erythrocytes), platelets (thrombocytes) and white blood cells (leukocytes). The red blood cells are among the smallest cells in the body (the smallest is sperm) and the most numerous type of cell present in the blood. A typical red cell has an average diameter of 7.7 μm and a maximum thickness of roughly 2.6 μm, but the center narrows averagely to about 0.8 μm. It is normally disc-shaped, soft and flexible, and red in colour. It is produced in the bone marrow and has no nucleus or mitochondria. Basically the red cell looks like a doughnut (please see Figure 3.1). This sort of shape provides a large surface-to-volume ratio which gives the cells a maximum probability of contact with the tissues. In one cubic millimeter of blood in the human body, there are on average about 5 million red cells. Women have average of 4.8 million of these cells per mm^3; men have average of 5.4 million of these cells per mm^3. Since there are approximately 5 litres of blood in the body, this means that in normal conditions there are on average about 25 trillion red cells present at any given time in the body.

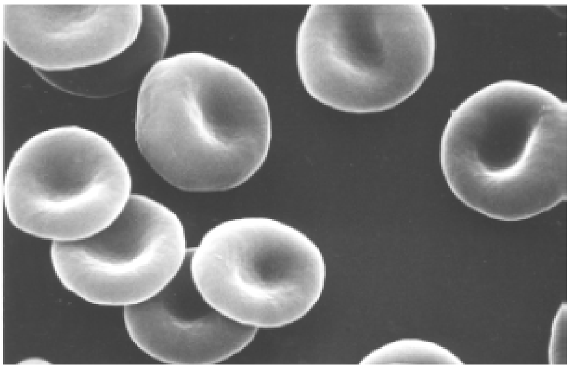

Figure 3.1: A SEM picture of erythrocytes. Taken from [Ery02]

The erythrocytes are responsible for the transport of oxygen and carbon dioxide. They can carry oxygen to all tissues from the lungs and carbon dioxide can also be transported from tissue cells to the lungs. An erythrocyte is also called a red cell because when the haemoglobins (a protein molecule in red cells) combine with oxygen, they become bright scarlet in colour. Red cells live for only about 120 days and are ingested by the phagocytic cells in the liver and spleen. Most of the iron in their haemoglobin is reclaimed for reuse. The remainder of the haem portion is degraded into bile pigments and excreted by the liver. Nearly 3 million red cells die and are scavenged by the liver each second.

3.1.1 Haemoglobin (Hb)

In the human body, the haemoglobin (Hb) is found in red blood cells. 98% of all of the oxygen that comes into the blood will get transported by haemoglobin. The remaining 2% is dissolved in the plasma. When the oxygen sticks to the haemoglobin, it is called oxyhaemoglobin. Otherwise it is called deoxyhaemoglobin. Oxygen associates with haemoglobin through weak chemical bonds. Once oxyhaemoglobin encounters an environment with a lower partial pressure of oxygen, the oxygen molecule will leave oxyhaemoglobin to move into this environment. There are approximately $200\sim300\times10^6$ haemoglobins in a single red cell.

The haemoglobin or hemoglobin is the iron-containing metalloprotein. It is a very large protein molecule which is designed to transport a relatively small oxygen molecule. Hb is an exquisite O_2-delivery system. This haemoglobin molecule is composed of four subunits. Every subunit has a haem and a polypeptide chain known as a globin chain, which is attached to a haem group. Every globin chain is non-covalently bound to the haems. The structure of the haem is a heterocyclic ring known as porphyrin. An iron containing porphyrin is termed a haem. This small rectangular haem group holds an iron atom in its center (please see Figure 3.2). There are four main kinds of interaction to maintain the quaternary structure of the haemoglobin [Wei74]. The first one is that the hydrophobic interactions which group together in the interior haemoglobin cause the polypeptide to fold. The second interaction is from the ionic bonds which occur between negatively and positively charged particles within the haemoglobin. The third interaction is from the hydrogen bonds which chemically bond between positively charged hydrogens and negatively charged atoms present in the haemoglobin. The fourth interaction is the Van der Waals forces, which stabilize the close interactions between the hydrophobic residues.

The position of the iron atom is the bonding site of the oxygen. Each iron can bind one O_2 molecule. A fully-loaded haemoglobin molecule binds four oxygen molecules. Four iron atoms lie at the heart of the Hb structure (please see Figure 3.3). An important characteristic for the bonding between O_2 and Fe is the effect of the oxidation state 2+ of Fe. When O_2 is bound to Fe, the oxidation state of Fe changes from 2+ to 3+. As known previously, the Fe^{3+}Hb (metHb) does not bind any O_2. The protein scaffold protects Fe against oxidation from 2+ to 3+. The formula below (3.1) describes the bonding relation.

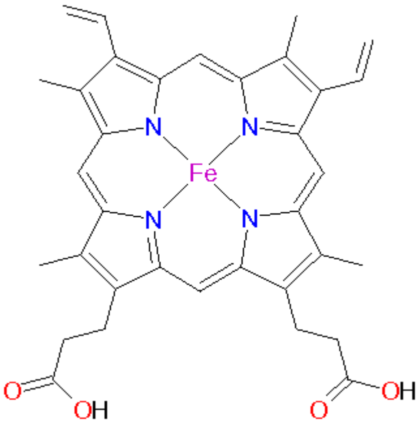

Figure 3.2: Structure of Haem. Taken from [Glo02]

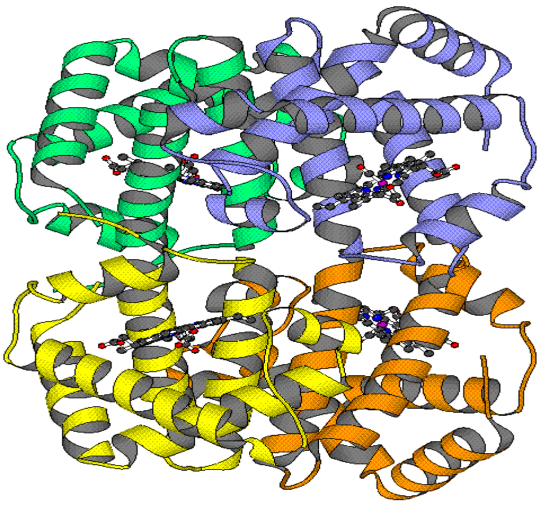

Figure 3.3: The helical structure of Haemoglobin. Taken from [Pro02]

$$Hb+4O_2 \rightarrow Hb(O_2)_4 \tag{3.1}$$

Cooperative bonding is also the characteristic of haemoglobin, giving it greater ability to bind oxygen [Wei74]. The sigmoid shape of the oxygen dissociation curve is a result of the cooperative bonding of oxygen to the four polypeptide chains (please see Figure 3.4). Such a curve, which is described as "cooperative", is due to the interactions between the four subunits making up the haemoglobin molecule.

97% of the normal adult haemoglobin is haemoglobin A (HbA) with 2 alpha chains and 2 beta chains. 2.5% of the normal adult haemoglobin is haemoglobin A2 (HbA2) with 2 alpha and 2 delta chains. The normal fetal haemoglobin is haemoglobin F (HbF) with 2 alpha and 2 gamma chains. The alpha chain is 141 amino acids long, while the beta chain is 146 amino acids long. Fetal haemoglobin (HbF) is found in the developing fetus and has a limited population in adult red cells. It has a more bonding affinity for oxygen. In adults, the haemoglobin is also called a tetramer. Each subunit of a tetramer has a molecular weight of about 16,000 Daltons and its total molecular weight is about 64,000 Daltons (one Dalton $\sim 1.66\text{x}10^{-24}$ g).

The bonding of oxygen is affected by other molecules similar to O_2. For example, the gas CO can compete with oxygen at the bonding site of Fe. The bonding affinity of haemoglobin for CO is 200 times greater than its affinity for O_2.

3.1.2 Factors to affect the bonding of the haemoglobin to oxygen molecules

Oxygen saturation is a measure of how much oxygen the blood is carrying as a percentage of the maximum it can carry. When every oxygen bonding site on all the Hb molecules is occupied by oxygen, the blood is said to be 100% saturated and the blood cannot carry any more oxygen. One haemoglobin molecule can carry a maximum of four molecules of oxygen. If a haemoglobin molecule is carrying three molecules of oxygen then it is carrying 75% of its maximum. If one hundred haemoglobin molecules are carrying 380 oxygen molecules then they are carrying 95% ((380/400) x100%) of their maximum and they are said to be 95% saturated. One important concept about oxygen saturation (sO_2) is its difference from the partial pressure of O_2 (PO_2). Hypoxia is due to the reduced PO_2 in the tissue; cyanosis is due to the reduced sO_2 in the blood.

There are several factors which can affect the ability of haemoglobin to pick up or release oxygen. The first factor depends on the partial pressure of oxygen in its environment. When the PO_2 is high, as it is in the capillaries around the lung, each haemoglobin can carry the maximum load of four oxygen molecules. As the blood circulates around the body, the blood experiences lower levels of partial pressure where the haemoglobin releases some of oxygen that it is carrying. The second factor is the temperature. Increasing the temperature denatures the bond between the oxygen and the haemoglobin, which increases the amount of oxygen and haemoglobin and reduces the concentration of oxyhaemoglobin. The oxygen dissociation curve (Figure 3.4) will shift to the right, due to the higher temperature. The third factor is the pH value which is related to the Bohr effect. As we know, normal physiological pH is 7.4. The Bohr effect suggests that if the pH drops below 7.4, the ability of haemoglobin to bind to oxygen will be lower and the oxygen dissociation curve will shift to the right. The fourth factor is the concentration of organic phosphates. 2,3-Diphosphoglycerated (DPG) is the primary organic phosphate in mammals. DPG can bind to haemoglobin and thus reduce the affinity of oxygen for haemoglobin. The oxygen dissociation curve will shift to the right, due to the bonding of DPG with haemoglobin. The fifth factor is the concentration of carbon dioxide, which affects the oxygen dissociation curve in two ways: firstly, it can influence the intracellular pH (the Bohr effect) and secondly, CO_2 accumulation can cause carbamino compounds which are generated through the chemical interactions. Low levels of carbamino compounds have the effect of shifting the oxygen dissociation curve to the right, while higher levels can cause a leftward shift. The sixth factor is the concentration of CO. Haemoglobin can bind with carbon monoxide 200 times more readily than with oxygen and therefore the presence of a large amount of carbon monoxide can easily interfere with the haemoglobin's acquisition of oxygen and then destroy the oxygen dissociation curve. However, a tiny amount of carbon monoxide has the effect of shifting the oxygen dissociation curve to the left and thus interfering with the unloading of O_2. The above-mentioned factors including the partial pressure of O_2, temperature, pH value, concentration of organic phosphates, concentration of CO_2 and the concentration of CO can directly affect the dissociation of oxygen.

Figure 3.4 describes the above four factors which affect the haemoglobin's ability to bind with oxygen in the human blood (the effects of the presence of CO_2 and CO are not shown in this figure). The horizontal axis of Figure 3.4 is the partial pressure of O_2 in the environment experienced by the red cells. The vertical axis of Figure 3.4 is the saturation percentage of haemoglobin with oxygen (oxyhaemoglobin). As can be seen from Figure 3.4, for the area where there is lower partial pressure of O_2, the haemoglobin releases some of the oxygen it is carrying, making the oxyhaemoglobin saturation rate lower; for the area with higher partial pressure of O_2, the haemoglobin can retain more oxygen, making the oxyhaemoglobin saturation rate higher. If the area which the red cells are experiencing a lower pH value, the oxygen dissociation curve will shift to the right. Therefore the oxyhaemoglobin saturation rate will be lower compared with an area with the same PO_2 but a higher pH value. If the DPG concentration in the environment experienced by the red cells is high and binds to haemoglobin, the oxygen dissociation curve will shift to the right. Therefore the oxyhaemoglobin saturation rate will be lower compared with an environment with the same PO_2 but a low DPG concentration. If the temperature in the environment experienced by the red cells is high, the oxygen dissociation curve will also shift to the right. Therefore the oxyhaemoglobin saturation rate will be lower compared with an environment with the same PO_2 but a lower temperature..

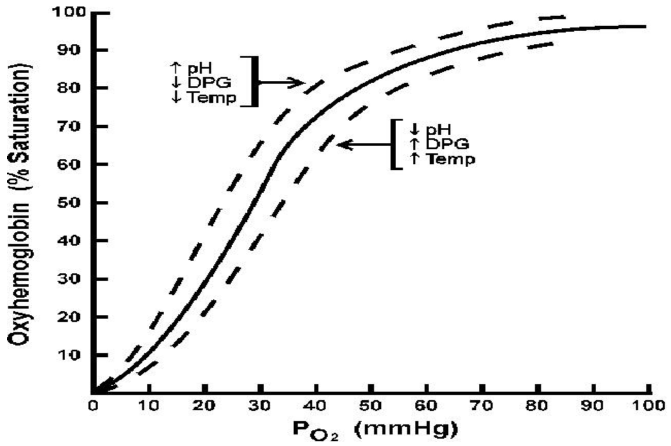

Figure 3.4 Hb saturation curve (oxygen dissociation curve). Taken from [Nap03]

3.1.3 Oxygen content determination

The oxygen saturation rate can be calculated from the measured parameters PO_2 and pH, on the basis of the standard oxygen dissociation curve (Figure 3.4). An assumption has been made to use this method, in which there exists an otherwise normal haemoglobin saturation curve. Most automated blood gas analyzers calculate the oxygen saturation rate in this way.

Spectrophotometric methods are also used to measure the oxygen saturation rate. The oxygen saturation rate can be calculated by investigating the difference between the absorption spectra of oxygenated haemoglobin and deoxygenated haemoglobin. Haemoglobin can absorb the infrared radiation as well as visible light and so it is easy to distinguish the oxyhaemoglobin and deoxyhaemoglobin by examining the absorption spectra patterns. Changes in oxygen saturation rate of haemoglobin can also be identified.

The principle of spectrophotometric method is mostly based on Beer's law, which describes the relationship between the absorbance A and the concentration c of a solute in a solution and the pass length l of a monochromatic light through this solution. The formula below applies to Beer's law.

$$A=\varepsilon\times c\times l \tag{3.2}$$

where A is a dimensionless number called absorbance, ε is a proportionality number called the molar absorptivity (unit: L• mmol^{-1} •cm^{-1}), c is the concentration of a solute in a solution (unit: mmol) and l is the pass length of a monochromatic light through this solution (unit: cm). ε is constant provided that the wavelength and temperature are constant. When there are two or more solutes in a solution, Beer's law can be expanded to the form given below:

$$A=l\times(\varepsilon_1 c_1+\varepsilon_2 c_2+\ldots\ldots) \tag{3.3}$$

where A is the absorbance of the mixture, ε_1 is the molar absorptivity for solute one, c_1 is the concentration of the solute one in the solution. Notice that the above formula applies only to the use of a given monochromatic light. Normally for every solute there exists a specific wavelength in which the solute will have a maximum absorption. This wavelength is a characteristic of this solute and is called λ_{max}. For a solution with two or more solutes, if we want to identify every solute, the different λ_{max} will normally be used to decide the maximum absorption for each one. By this means the following formula can be devised to describe the relationship between the absorbance of the mixture and the use of different wavelengths.

$$A(\lambda_j)=l\sum_{i=1}^{N}\varepsilon_{ij}(\lambda_j)c_i \tag{3.4}$$

where in this solution there exist N solutes, j is from 1 to N and ε_{ij} is the molar absorptivity of the i^{th} kind of solute measured by the wavelength λ_j.

All kinds of spectrophotometer have the following fundamental parts: a source of radiation energy, a grating to isolate the radiation energy to a specific narrow wavelength region, a device for holding the sample and a photoelectric cell for measuring light intensity. Normally we can use a wavelength selector on the spectrophotometer to choose the wavelength of interest for irradiating the sample. The transmittance T from the measurement of a spectrophotometer is defined as the ratio of the intensity of incident light to the intensity of transmitted light. The absorbance A is defined as the following formula:

$$A=-\log_{10}T \tag{3.5}$$

Normally when the light passes through the sample and falls on a photoelectric cell which can record the intensity of the light, transmittance T can be electronically converted and displayed on the scale of this instrument. However as the absorbance A is directly related to the concentration of a solute in a solution and to the pass length of the light through this solution, it is preferable to display this value on the scale of the spectrophotometer.

For the purpose of analysing a blood sample, we can normally regard the oxyhaemoglobin and deoxyhaemoglobin as the two solutes in the blood solution and thereby apply the spectrophotometric method to analyse this blood solution. Figure 3.5 gives the absorption spectra for human oxyhaemoglobin and deoxyhaemoglobin. Note that there is an isosbestic point (at which the molar absorptivity is identical for the two forms of haemoglobin) at around 548 nm and there is a maximum molar absorptivity at around 577 nm for oxyhaemoglobin. Generally a blood sample can be analysed at two wavelengths in the visible spectrum (380 nm～780 nm). In one wavelength a large difference in absorbance occurs between the deoxygenated and oxygenated haemoglobin. As can be seen from Figure 3.5, there is a maximum molar absorptivity at 577 nm for the oxyhaemoglobin and at this wavelength the change in molar absorptivity is greatest for a given change in concentration. That is, the measurement of concentration is most sensitive at this wavelength. The other wavelength is used to find the isosbestic point. As can be seen from Figure 3.5, there exists an isosbestic point at 548 nm. The measurement at the isosbestic point can give the total amount of haemoglobin present (From formula (3.3), c_1+c_2 can be calculated if only two solutes exist in the solution and $\varepsilon_1=\varepsilon_2$ at a given wavelength) and the absorption at the other wavelength depends on the difference in concentration of the two forms of haemoglobin. If we combine the measured data from the absorption spectrum at 577 nm and 548 nm, we can determine the individual concentrations for oxyhaemoglobin and deoxyhaemoglobin.

The Reflectance Spectrophotometry (RS) and the Near-Infrared Spectrophotometry (NIRS) are the major spectrophotometric methods for measuring the oxygen saturation rate of blood. As most samples are more opaque to visible light, the accuracy of the Reflectance Spectrophotometry is limited, due to the use of visible light. However, as most samples are more translucent to the near-infrared region of the spectrum (780 nm～1400 nm), Near-Infrared Spectrophotometry has greater accuracy than techniques using Reflectance Spectrophotometry. By applying Near-Infrared Spectrophotometry to analyse a blood sample, we can assess the oxygen saturation rate. The determination of CO content can also be justified by using the Reflectance Spectrophotometry or Near-Infrared Spectrophotometry as the basic principle to determine the CO content is identical with the determination of the O_2 content. Some related conceptual descriptions of the determination of carboxyhaemoglobin concentration are given in section 3.2.4.

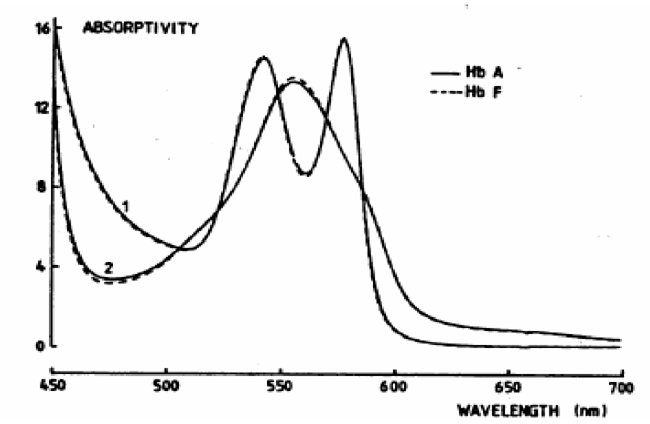

Figure 3.5: Absorption spectra of HbA (Adult) and HbF (Fetal): 1 is the oxyhaemoglobin, 2 is the deoxyhaemoglobin. Taken from [Zij91]

3.1.4 CO transport

Oxygen has a limited solubility in blood; in fact only about 2% of oxygen carried in the blood is dissolved in the blood plasma. Most of the oxygen is transported in the blood by haemoglobin. As described above, one haemoglobin can bind 4 O_2 molecules to form oxyhaemoglobin whereby the body can be adequately supplied with oxygen. Carbon monoxide (CO) is an odourless, colourless, non-irritant gas. When the CO is inhaled, it can readily bind to haemoglobin and does so about 200 times more tightly than oxygen, forming a compound called carboxyhaemoglobin. The gas of CO binds very well with haemoglobin and it does not tend to dissociate. As CO has a much higher affinity with haemoglobin, if both carbon monoxide and oxygen are inhaled, carbon monoxide will preferentially bind to haemoglobin.

The CO competes with oxygen to bind at the same position in the haemoglobin. This competitive result will reduce the amount of haemoglobins available to bind to oxygen and inhibit the red cells from carrying oxygen to the body organs, including heart and brain which will become starved of oxygen. Therefore, when a person inhales a great deal of CO, more and more carbon monoxide permanently binds to the haemoglobins, which are no longer available for transporting oxygen. If we replace oxygen with carbon monoxide in our blood, our bodies are poisoned and cause various degrees of damage, depending on the different exposure conditions. How quickly the carboxyhaemoglobin builds up is a factor of the concentration of the gas being inhaled (measured in parts per million or PPM) and the duration of the exposure. The formula below (3.6) describes the bonding relation between CO and the Hb.

$$Hb+4CO\rightarrow Hb(CO)_4 \tag{3.6}$$

In this feasibility study, we are interested only in a single red cell labelled with the radioactive gas ^{11}CO. The best condition for this study to succeed is that we can make every haemoglobin bind to 4 ^{11}CO molecules in a single red cell. For labelling the red cells in a vial of known volume (section 3.2.1), if the vial is full of high-purity ^{11}CO and if we know how many live red cells are in this vial, we can expect that every red cell in this vial will absorb the ^{11}CO gas to the maximum load. Namely, every haemoglobin will bind to 4 ^{11}CO molecules in a single red cell in this labelling vial. As described above, there are nearly $200\sim300\times10^6$ haemoglobins in a single red cell; ideally it may be concluded that one single red cell can absorb $\sim10^9$ $(250\times10^6\times4)$ ^{11}CO molecules which is equal to 0.015 mCi (please see section 3.4.2).

For a more quantitative description of the relationship between CO tension (concentration) and HbCO saturation rate with time, Reeves and Park [Ree92] investigated the θ_{CO} which is the carbon monoxide diffusing capacity per mL of blood (measured in vitro). They enclosed the whole blood thin film (1.5 µm～6.0 µm) in a highly gas permeable open mesh of Teflon fibrils and then exposed them to step changes of CO pressure (PCO) and O_2 pressure (PO_2). Figure 3.6 [Hug03], which was taken from Reeves and Park, can provide a clearer profile for the combination of haemoglobin and CO with time. As one can see from this figure, for the upper curve, the environment for the whole blood thin film had no CO gas but the O_2 pressure was 70 mmHg (1 mbar～0.75 mmHg). It was found that the HbO_2 saturation rate reached almost 100% within 160 ms. For the middle curve, the CO pressure was 70 mmHg and the O_2 pressure was 70 mmHg. It was found that the HbCO saturation rate could reach more than 75% within 160 ms. For the bottom curve, the O_2 pressure was 280 mmHg and the CO pressure was 70 mmHg. It was found that the HbCO saturation rate was lower than the middle curve but could still reach more than 50% within 160 ms. In this figure, $t_{1/2}$ means the time taken to reach half of the saturation rate for HbO_2 or HbCO. For the upper curve, $t_{1/2}$ is 8 ms; for the middle curve, $t_{1/2}$ is 68 ms and for the bottom curve, $t_{1/2}$ is 150 ms. For the upper curve, the whole blood thin film was in a pure oxygen environment (PO_2 = 70 mmHg) and the HbO_2 saturation rate could quickly reach 50%, within 8 ms. For the middle curve, the whole blood thin film was in a low PO_2 environment (PO_2 = 70 mmHg, PCO = 70 mmHg) and the HbCO saturation rate could reach 50% within 68 ms. For the bottom curve, the whole blood thin film was in a higher PO_2 environment (PO_2 = 280 mmHg, PCO = 70 mmHg) and the HbCO saturation rate could still reach 50% within 150 ms. From the above discussions for this figure, one can infer that if the whole blood thin film is in a pure CO environment and the CO pressure is 70 mmHg, the HbCO saturation rate should reach 50% in less than 8 ms, as the CO gas has an even higher affinity with the haemoglobin molecule.

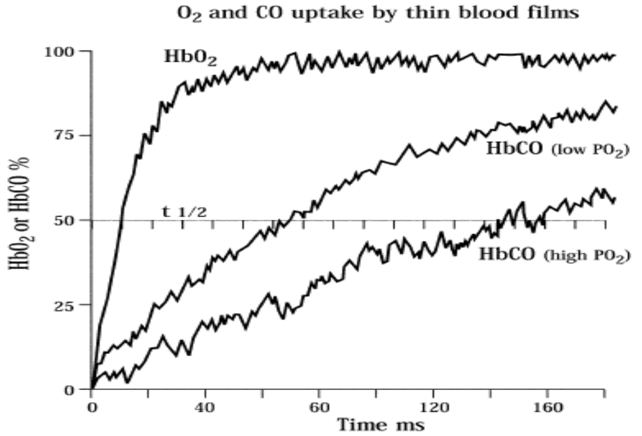

Figure 3.6: Time course of percent O_2 and CO bonding on a whole blood thin film. Taken from [Hug03]

The above result may be helpful for understanding the relationship between the saturation rate and time when we are using the radioactive ^{11}CO to label the red cells in our solution vial. As the result from Figure 3.6 is based on the use of the blood thin films, some extra-cellular diffusion barriers have been naturally minimized [Ree92]. That means that the gas CO or O_2 can more easily reach the red cell. A microscopic description of the diffusion capacity of CO in the red cell is given by [For64]. As CO diffuses into the red cell, the outer layers of Hb combine with it so rapidly that an 'advancing front' is built. This 'front' results from the chemical combination between the CO and the outer layers of Hb. Thereby this phenomenon of the 'advancing front' can reduce the dissolved CO tension and slows the diffusion of CO in the red cells. From a macroscopic point of view, Figure 3.6 provides a clearer understanding of the combination effect between the CO and the sample of whole blood thin film. Nevertheless all the above discussions can only be a relative reference when compared with the practical conditions in our labelling solution vial (see section 3.2.1).

3.1.5 Packed red blood cells

If one takes a sample of blood, treats it with an agent to prevent clotting and spins it in a centrifuge, one will find that the red cells settle to the bottom and the white cells settle on top of the red cells, forming a buffy coat. The upper layer of the buffy coat consists of plasma mixed with platelets. The platelet-rich plasma can be expressed off, leaving the plasma mixed with white cells and red cells. Blood can be stored as whole blood with all of the plasma present or as packed red blood cells (PRBCs) in which 70% of plasma has been removed and some necessary chemicals have been added. Both whole blood and PRBCs can be stored for up to 42 days at 1～6 ºC in a normal refrigerator.

3.1.6 How the red blood cell dies

In a human body, the average life cycle of a red blood cell is 120 days. Over this time, the red blood cells wear out and eventually die. Red blood cells are made in the bone marrow. They start out with a nucleus, like other cells, but when they fill up with haemoglobin the nucleus is squashed smaller and smaller until it completely disappears. In the human body, about 3 million red blood cells die per second. But the bone marrow produces new red blood cells equally fast. The bones are continually producing new red blood cells, replenishing the supply.

The red cell is enclosed in a thin membrane which is composed of chemically complex lipids, proteins and carbohydrates in a highly organized structure. The membrane itself is flexible and is able to bend in many directions without breaking. This is an important characteristic, because when the red blood cells pass through the tiniest blood vessels, the capillaries, which are narrower at some points than the size of red cells, they have to bend or become deformed to deliver the oxygen through these smaller capillaries. When the bending or deforming stress is removed, the red blood cell springs back to its original shape. The red cell readily tolerates bending and folding, but, the cell is damaged or destroyed by appreciable stretching of the membrane.

The membrane is freely permeable to water, oxygen, carbon monoxide, carbon dioxide, glucose, urea, ions and certain other substances, but it is impermeable to haemoglobin. Within the red cell, the major cation is potassium. In contrast, in plasma and extracellular fluids, the major cation is predominantly sodium. A pumping mechanism called a "sodium pump" in cellular physiology, driven by enzymes within the red cell, maintains its sodium and potassium concentrations within the red cell. The sodium pump is in fact a protein which is embedded in the membrane. It has been identified in many cells and probably occurs in all kinds of cell. This mechanism maintains a higher internal concentration of potassium ions [K+] than that of the surrounding medium (blood, body fluid, water) and also maintains a very much lower internal concentration of sodium ions [Na+] than that of the surrounding medium. If the pumping mechanism is broken, the red blood cell will die.

3.2 Method of Labeling RBCs with ^{11}CO

A method of labelling red cells previously used by J. C. Clark et al. [Cla75] is shown in Figure 3.7 below. A blood sample 5 ml is dropped into a 45 ml syringe. ^{11}CO is filled into this syringe with the blood sample. One can detect the activity of ^{11}CO in the syringe first. After a period of mixing, by rotating the syringe on its axis at 10 rpm for 10-18 minutes, about 50 percent of the ^{11}CO in syringe is absorbed into the red cells. ^{11}CO is then expelled to a safe container. One can detect the activity of the labelled red cells in the syringe and compare the measured activity values.

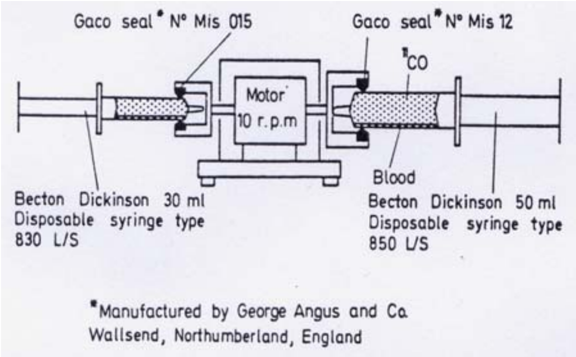

Figure 3.7: Syringe rotating device for in vitro RBCs labelling with ^{11}CO. Taken from [Cla75]

The labelling efficiency depends on the mixing time and the blood sample itself. Blood samples for labelling and subsequent re-injection are not allowed to remain in vitro for more than 3 hours at room temperature. One needs to use anticoagulant for the red cells when these cells are in the in vitro condition. For maximum uptake of activity, the optimum mixing time is shown in Figure 3.7 below.

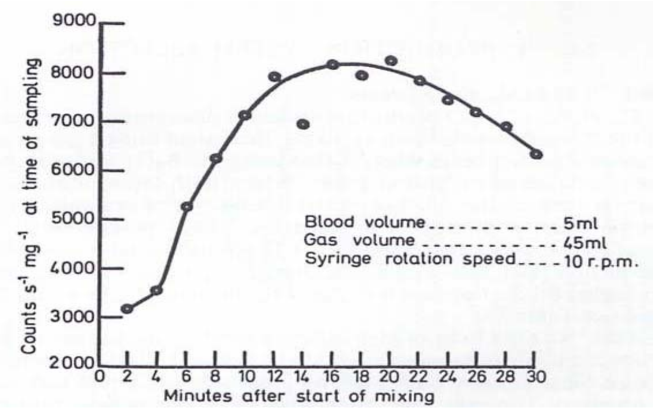

Figure 3.8: RBCs' activity versus mixing time. Taken from [Cla75]

3.2.1 A prototype labelling system

We had already built a preliminary labelling apparatus in which a bubbling method was used to do the labelling. This preliminary apparatus can be seen below (Figure 3.9). Before opening the switch valve V1 to let the ^{11}CO gas enter this labelling system, a vacuum pump (pump 1) was opened to evacuate the labelling system. When the pressure in the labelling system was down to a few mbar, this vacuum pump was turned off. A transportation pump (pump 2) was then turned on for the purpose of drawing the ^{11}CO gas into the labelling system. The ^{11}CO reservoir was located at the cyclotron area while the labelling system was in another room. As the ^{11}CO reservoir was more than 10 m away from the labelling systems, we needed to use the carrier gas nitrogen to assist the flow of ^{11}CO. We turned on V1 to let ^{11}CO flow into a storage vial which was inserted into a Capintec ionization chamber. It took probably 20 minutes for the activity reading to reach a maximum value of～1 mCi. After reaching this level of activity, we closed the switch valve V1 to disconnect the reservoir of ^{11}CO. By turning off V1, we had created a closed system for the purpose of labelling and the ^{11}CO gas was restricted to the storage vial. To operate the labelling process, we had merely to open the four other valves (V2, V3, V4, V7) and let the ^{11}CO gas flow through into the labelling vial in where the red cells were in a saline solution. The ^{11}CO gas can circulate in this closed system until it was decided that the labelling should be finished. Before transporting the ^{11}CO into the labelling system, the vacuum level in the labelling system should be noticed. Due to the limited capability of our pump system (only 0.1 mbar) and the poor pressure meter (only several mbar) used in this labelling system, we could only extend the pumping time and avoid any leakages in this labelling system in order to reduce the possible contamination of CO originally existing in the labelling system.

The SA value in this storage vial can be estimated. The mole number of gas in the storage vial was found to be～1.4×10^{-3} (using volume of storage vial～7×10^{-5} m^3, pressure～500 mbar, temperature～298 K) and the SA was calculated as 1 mCi/1.4×10^{-3} mole～0.714 µCi/µmole. However as the labelling system did not have a function for separating the carrier gas with the transported ^{11}CO, a great deal of N_2 was mixed with the ^{11}CO in the storage vial. Thereby the estimated SA value lost its accuracy.

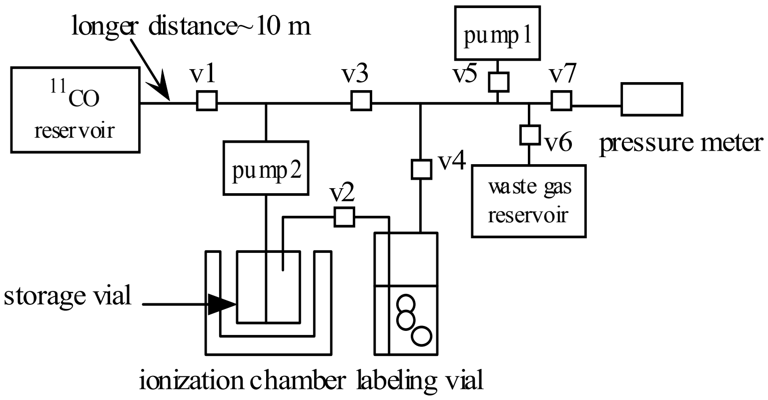

Figure 3.9: Schematic for a prototype labelling system

3.2.2 Several considerations in the labelling process

The carbon monoxide can be regarded as the gaseous solute. Its natural solubility is 0.0026 g in 100 g water at 25 °C. By using its solubility, we can find how many moles of ^{11}CO can naturally exist in the red cells solution. In principle, if we can allow more ^{11}CO gas (to raise the flow rate) to flow around the red cells in the saline solution, a higher collision probability can occur and more ^{11}CO gases may bind to the haemoglobins.

Some factors which affected the labelling efficiency in the labelling vial should be carefully considered. For example, the flow rate of ^{11}CO into the labelling vial (this affected the collision times per second), the concentration of red cells in the saline solution (this affected the total collision area), the pH value in the solution (this affected the dynamic activity of red cells) and the ambient temperature of the vial (this affected the solubility of ^{11}CO in the saline solution). In addition to these factors, as so much N_2 had been mixed with the ^{11}CO in the labelling system, it seriously reduced the SA value in the storage vial and seriously affected the labelling efficiency in the labelling vial. Therefore a delicate ^{11}CO trapping technique (we used only a simple storage vial) in the labelling system should be adopted to separate the carrier gas N_2. In order to obtain the red cells sample, a 5 ml syringe and a needle with a diameter of 100 µm were used to aspirate some blood from the donor's blood vessels.

3.2.3 Activity measurement for the labelled red blood cells

Before removing the labelling vial, the residue of ^{11}CO was expelled. We removed it (using a proper lead container) to the PEPT laboratory and measured its activity using the ionization well chamber. Alternatively, one can set up a scintillation detector to measure the activity in the labelling vial. However, as mentioned in Chapter 2, several important factors need to be considered carefully when using a scintillation detector to measure activity. In practice this is not an easy method. Figure 3.10 below describes the set-up of a scintillation detection.

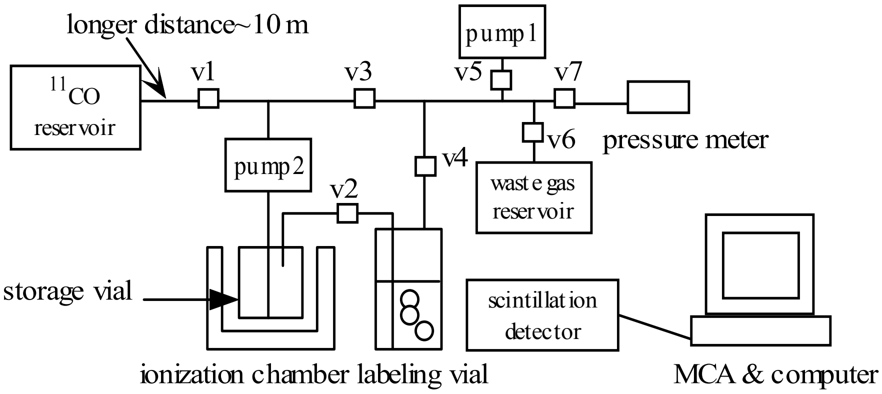

Figure 3.10: A scintillation detector used to detect the activity of labelled red cells

As a better choice, a well counter was used to measure the activity of the labelled red cells. 30 µCi was found for the labelled red cells. Thereby the labelling efficiency was equal to 30 µCi /1 mCi∼3%. This ionization well chamber is the Capintec CRC-15R dose calibrator, which has a thin wall, deep well (26 cm) and a 6.4 cm diameter opening (please see Figure 3.11). High-pressure Argon is used as the medium for reacting with the photons. Its resolution is 0.01 µCi. Maximum activity is up to 6.5 Ci for Tc-99m.

Figure 3.11: Capintec CRC-15R dose calibrator

A coincident detection device with a pair of NaI(Tl) scintillation detectors attached to a coincident circuit can be constructed to measure the activity of the positron-emitting tracer by detecting coincident pairs of 511 keV photons (please see Figure 3.12). The ADAC Forte PET camera can be regarded and used as a coincident detection device. The sensitivity of the coincident device is experimentally determined. Its performance can be compared to the performances of a well counter and a NaI(Tl) scintillation detector. As the square of the detection efficiency in one detector equals the coincidence detection efficiency, assuming the same type of detector and geometry, etc., the coincidence detection efficiency must be lower than the detection efficiency in one detector.

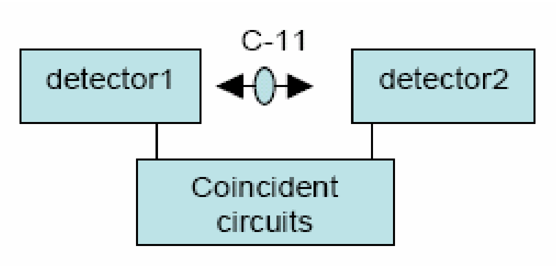

Figure 3.12: Schematic for the coincident detection

A technique called the $4\pi\ \beta-\gamma$ coincidence technique can also be adopted to calculate the activity. In many radiation applications, one needs to know the activity of the short-lived radionuclide, whereas the relative measurement may be hampered by the absence of a reference source. From one paper [Nic04], an analytical model based on a probabilistic approach was set up to calculate and predict the activity of ^{11}C using the $4\pi\ \beta-\gamma$ coincidence technique. The $4\pi\ \beta-\gamma$ coincidence technique and the results of modelling allow activity measurements of ^{22}Na and ^{11}C sources with a relative standard uncertainty in the order of one percent. A $4\pi\ \beta-\gamma$ coincidence counting system normally consists of a high pressure 4π proportional counter with two same face-to-face NaI(Tl) detectors around the 4π counter, which is typically operated at a pressure of 20 atmospheres.

3.2.4 Conceptual spectrophotometric analysis for carboxyhaemoglobin

The method described conceptually in section 3.1.3 can be applied to the examination of the concentration of carboxyhaemoglobin as the principle that examining the oxygen saturation rate is basically the same as examining the concentration of carboxyhaemoglobin in a blood sample (see section 3.1.3). For this feasibility study, we are naturally much interested in identifying the concentration of carboxyhaemoglobin in a blood sample. As a conceptual approach to examining the concentration of carboxyhaemoglobin, only the important concepts are mentioned in the following description. Figure 3.13 shows the absorption spectra of human haemoglobin for the carboxyhaemoglobin and methaemoglobin. For the simplicity of the question concerned, we can assume that all oxygen bonding sites at the haemoglobin are basically replaced by the ^{11}CO and the only two solutes in the blood sample are the methaemoglobin and carboxyhaemoglobin. As the same approach as that in section 3.1.3, we need to find a maximum distance between the absorption spectra of carboxyhaemoglobin and methaemoglobin. At around 570 nm from Figure 3.13, there exists a maximum molar absorptivity for carboxyhaemoglobin and at this wavelength the change in molar absorptivity is greatest for a given change in concentration. That is, the measurement of concentration is most sensitive at this wavelength. We also need to find an isosbestic point in order to decide the total amount of haemoglobin present in the blood sample. At around 520 nm from Figure 3.13, there exists an isosbestic point which can be used as the calculation of total amount of haemoglobin. By using the above two wavelengths, we can build a set of equations below and determine the concentrations.

$$^{570}A = l\,(^{570}\varepsilon_c c_c + {}^{570}\varepsilon_m c_m) \tag{3.7}$$

$$^{570}A = l\ {}^{520}\varepsilon(c_c + c_m) \tag{3.8}$$

Where ^{570}A is the absorbance at 570 nm for this blood sample, ^{520}A is the absorbance at 520 nm for this blood sample, l is the pass length of the transmitted light through this sample, $^{570}\varepsilon_c$ is the molar absorptivity at 570 nm for the carboxyhaemoglobin, $^{570}\varepsilon_m$ is the molar absorptivity at 570 nm for the methaemoglobin, $^{520}\varepsilon$ is the same molar absorptivity at the isosbestic point shown at 520 nm. c_c is the concentration of carboxyhaemoglobin and c_m is the concentration of methaemoglobin. As the absorbance A can be easily found from the scale of a spectrophotometer, we can easily solve this set of equations and find c_c and c_m.

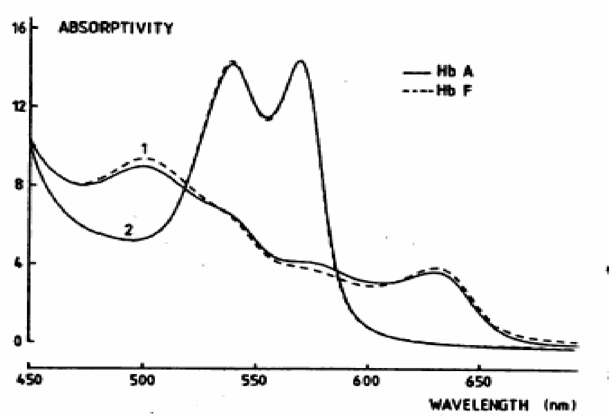

Figure 3.13: Absorption spectra of HbA (Adult) and HbF (Fetal): 1 is the methaemoglobin, 2 is the carboxyhaemoglobin. Taken from [Zij91]

A spectrophotometer is a very sensitive and expensive instrument which is not available in our lab. However the method introduced here should be helpful to this study. In Reference [Bre03], three methods were described to determine the concentration of carboxyhaemoglobin. The three methods were Maehly's spectrophotometric method [Mae62]; a gas chromatographic method with a thermal conductivity detector (GC-TCD) [Dam94]; and the Oximeter [Yuk98] which is a special automated spectrophotometer. Although the purpose of these three methods described above was to investigate the carboxyhaemoglobin in post-mortem blood samples, they are also suitable for examining the ^{11}CO saturation rate in our study provided that the appropriate blood sample preparations can match the requirements of these three methods.

3.2.5 A preliminary result for the imaging of labelled red blood cells

A preliminary visualization image (Figure 3.14) was acquired by the PET imaging system. We can regard the labelling vial as a small animal in which one of the organs was filled with ^{11}CO gas. As no other red cells were in any part of this vial except the bottom and we had expelled the remaining ^{11}CO gas after shaking this vial, basically the left red spot of the intensity image which can be seen below (Figure 3.14) reveals that the red cells had indeed absorbed the ^{11}CO gas. This was an acceptable result. However, a more sophisticated labelling system with a more efficient shaking or rolling apparatus and with some necessary sensors should be considered carefully in the future.

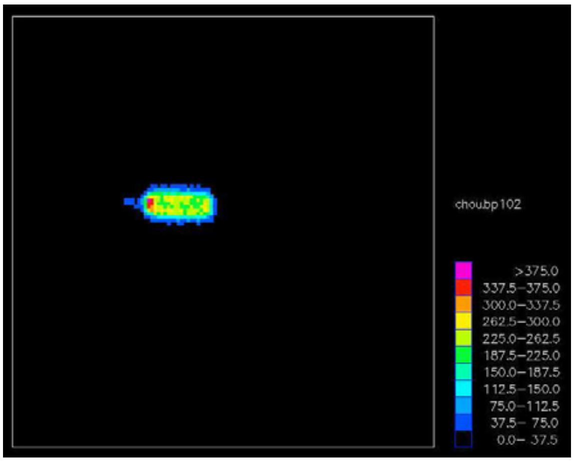

Figure 3.14: A preliminary result for the labelling

3.3 Methods proposed to isolate a single labelled RBC

After obtaining the labelled red cells, we needed to isolate a single labelled red cell. As the size for a red cell is only around 7~12 µm, a specific technology to isolate it is normally used. During the isolation operation, the most important thing to guard against is the death of labelled red cells. The goal is to acquire a single living labelled red cell with enough activity to be tracked. If all labelled red cells die before they are isolated, the following isolation operation will be meaningless, for a dead labelled red cell does not function well to reserve the radioisotopes of ^{11}C in its haemoglobins. The following proposed methods are only conceptual for future reference.

3.3.1 Traditional method

The dilution method can probably be used in the separation of labelled red cells. For example, men have on average 5.4×10^6 red cells per 1 µL blood. If we dilute the labelled 1 µL blood with a 10^6 fold saline solution, on average a concentration of 5.4 labelled red cells per litre can be reached. A micro-pipette then may be used to aspirate one drop from this dilute solution. The weakness of this separation method is that it sometimes aspirates nothing because of the problem of statistical distribution. We do not know where the average 5.4 labelled red cells are in the one litre solution.

A commercial micromanipulator equipped with a pressure device and mounted on a routine research microscope can be used to do the separation. The diameter of the opening of the capillary tip installed on this micromanipulator can be adjusted to the size of the cell of interest. A high performance CCD camera can also be equipped with this micromanipulation system to help the separation operation. This commercial micromanipulator is much more expensive and should normally be operated according to the manufacturer's instructions. However, it is a useful and powerful apparatus for this task.

3.3.2 Laser micromanipulation system

Using a Laser to do the micromanipulation has been possible for some time. Optical tweezers and laser micro-dissection are the two main techniques. For the optical tweezers, the principle is simply described as a schematic below (Figure 3.15). A laser beam is focused through the microscope lens. If the sample of interest is located exactly below the laser's focus, due to radiation pressure, a net force will be exerted on the sample of interest and will pull it upwards. Conversely, if the sample is exactly located above of the laser's focus, a net force will be exerted on this sample and will pull it downwards. By using the radiation pressure of the laser, one can easily pick up a biological cell from a group of cells.

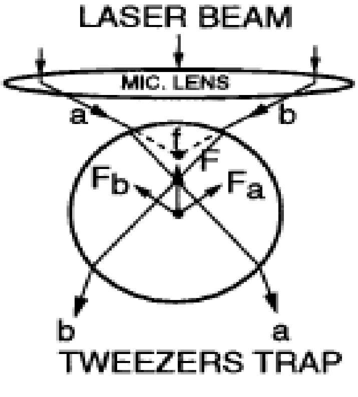

Figure 3.15: Principle of optical tweezers. Taken from [Ash97]

For laser micro-dissection, a simple schematic is shown below (Figure 3.16) to illustrate this technology. A nitrogen laser is focused through the microscope lens to a diameter of several microns or less. The area of interest is ablated by the laser focus. After this ablation, the position of the laser focus is changed to a point below the sample of interest. With a laser beam of increased energy and radiation pressure, the sample of interest is catapulted into a cap [Frö00, Sti03].

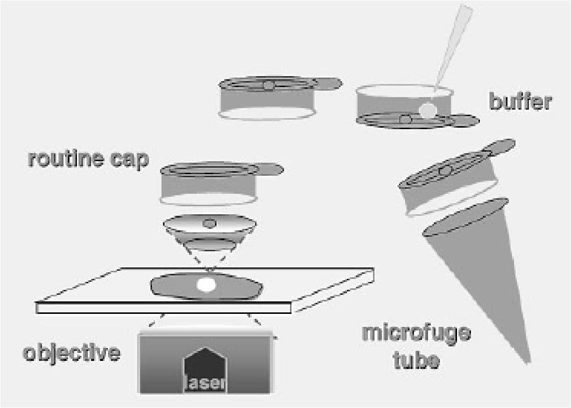

Figure 3.16: A set-up for laser micro-dissection. Taken from [Sti03]

3.3.3 Dielectrophoresis

The principle of the dielectrophoresis technology is shown as a schematic below (Figure 3.17). When a dielectric particle is in an inhomogeneous electric field, due to the polarization effect of the dielectric particle, an interaction between the electric field and the polarized particle will occur. A net force will be exerted on this polarized particle and push it into the area of a higher electric field, so long as the dielectric particle is more polarizable than its surrounding medium. Using this characteristic, one can design a delicate electrode system for picking up a single cell.

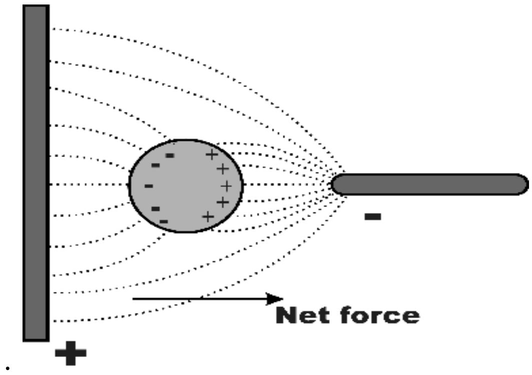

Figure 3.17: Principle of dielectrophoresis. Taken from [Hug99]

The laser micromanipulation system and the dielectrophoresis technology have been the staple methods for separating a single biological particle, which can be smaller than a few μm ([Ash97], [Sti03], [Hug99]). However as they are all expensive and sensitive instruments, only professional biochemical laboratories can afford them. For this feasibility study at the Positron Imaging Centre at Birmingham, they are beyond our means. And, as mentioned above, due to the problem of statistical distribution, the dilution method of isolating cells will be very unfeasible.

3.4 An ideal activity without biological considerations

As described before, ^{11}CO will compete with O_2 and its affinity is 200 times higher than O_2. We can build a simple model to calculate the ideal activity of a red cell labelled with $^{15}O^{15}O$ or ^{11}CO. In this model, I have made the assumption that all the O_2 bonding sites in a red cell have been replaced by the $^{15}O^{15}O$ or ^{11}CO whichever is applicable.

3.4.1 Haemoglobin labelled with $^{15}O^{15}O$ ($^{15}O_2$)

As we know, there are n~2.5×10^8 haemoglobin molecules in one single red blood cell. Each haemoglobin has 4 haems with 4 irons individually and each iron can bind one O_2 molecule. Therefore in a single red blood cell, the number of ^{15}O atom~8n is the most that can be bound. If the requirement of activity for tracking purposes is *X mCi,* we can set the equation below (3.9):

$$X\ mCi=\lambda N\ \ (N=8n\sim2\times10^9) \tag{3.9}$$

where λ is the decay constant (unit=s^{-1}) and N is the number of the radioactive ^{15}O. By inserting the relations of $\lambda = \ln2/t_{1/2}$, where $t_{1/2}$ is the half-life, and $N=8n=2\times10^9$ into equation (3.9), we reach equation (3.10) and find the X value (3.11).

$$X\times10^{-3}\times3.7\times10^{10}=(\ln2/t_{1/2})\times8n\quad ,t_{1/2}=122.24\ \ seconds \tag{3.10}$$

$$X\sim0.3 \tag{3.11}$$

We can find that activity X is equal to *0.3* mCi in a single red blood cell if all the binding sites are fully bound by $^{15}O_2$ molecules.

3.4.2 Haemoglobin labelled with ^{11}CO

When ^{11}CO is inhaled, it combines with the oxygen carrying haemoglobin to form carboxyhaemoglobin. ^{11}CO will compete with O_2 to bind the original positions of O_2. If we assume the concentration of ^{11}CO is so high that all the O_2 bonding positions are replaced by ^{11}CO and assume the requirement of activity for the tracking purpose is *X mCi,* we obtain the equation below (3.12) :

$$X\,mCi=\lambda N\ (N=4n\sim10^9\,) \tag{3.12}$$

where λ is the decay constant (unit=s^{-1}) and N is the number of the radioactive ^{11}C. By inserting the relations of $\lambda = \ln2/t_{1/2}$, where $t_{1/2}$ is the half-life, and $N=4n=10^9$ into equation (3.12), we can have an equation (3.13) and find the X value (3.14).

$$X\times10^{-3}\times3.7\times10^{10}=(\ln2/t_{1/2})\times4n\quad ,t_{1/2}=1223.1\ \ seconds \tag{3.13}$$

$$X\sim0.015 \tag{3.14}$$

We can find that the activity is equal to 0.015 mCi in a single red blood cell if all the bonding sites are fully bound by ^{11}CO molecules. What we have obtained from sections 3.4.1 and 3.4.2 is all based on the assumption that all the irons in the haemoglobins are fully bound by $^{15}O_2$ or ^{11}CO when they act with haemoglobins in a single red blood cell. This assumption is ideal and not duplicated in practice. The estimated activities we have acquired from sections 3.4.1 and 3.4.2 should be reduced to a reasonable level in an authentic biological environment.

The figure below (Figure 3.18) describes a schematic process for this feasibility study. A container made of lead was used to transport the labelling vial in which the labelled red cells existed in the bottom of the vial and the residue ^{11}CO was expelled. In the future, once a single labelled red cell is obtained with suitable activity, it will be injected quickly into a pipeline system or a phantom for the final tracking purpose.

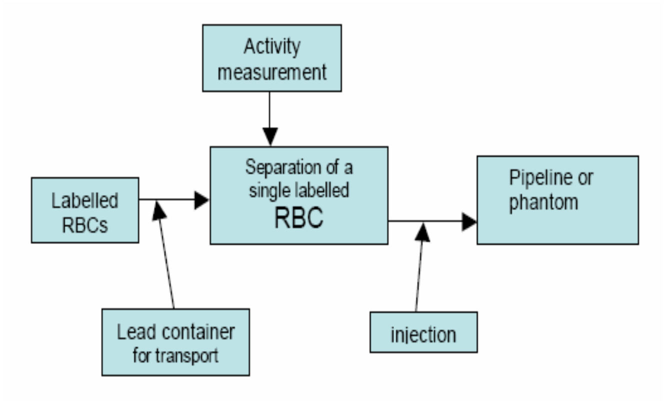

Figure 3.18: Flow process for a single labelled RBC to carry out tracking

3.5 Summary

This chapter mainly deals with the related experiments and concepts of labelling red cells. The fundamental properties of red cells and haemoglobin and the characteristics of bonding between O_2 and haemoglobin and between CO and haemoglobin are described. A conceptual spectrophotometric method is introduced in sections 3.1.3 and 3.2.4 to estimate the possible concentrations of oxyhaemoglobin and carboxyhaemoglobin. In section 3.1.4, Figure 3.6 illustrates the probable relationship between the concentration of HbO_2 or HbCO and the bonding time. In section 3.2.1, a simple manual labelling set-up was described. Due to the limited capability of our pumping system (only 0.1 mbar) and the poor pressure meter (only a few mbar) used in this labelling system, we could only extend the pumping time and avoid leakages in the labelling system if we wanted to reduce possible contamination by CO or other chemical forms originally existing in the labelling system.

After finishing the transportation of ^{11}CO into the labelling system (the maximum activity we could receive in the storage vial was 1 mCi.), we could estimate the SA value in the ^{11}CO storage vial which was inserted into an ionization chamber. The mole number of gas in the storage vial was found to be $\sim 1.4\times10^{-3}$ (using the volume of storage vial $\sim 7\times10^{-5}$ m^3, pressure$\sim$500 mbar, temperature$\sim$298 K) and the SA was calculated as 1 mCi/1.4×10^{-3} mole$\sim$0.714 μCi/μmole. However as the labelling system did not function to separate the carrier gas with the transported ^{11}CO, a great deal of N_2 was mixed together with the ^{11}CO in the storage vial, destroying the accuracy of the estimated SA value.

As mentioned in section 3.2.2, the labelling process was closely related to the collision probability between the ^{11}CO molecules and the red cells. A higher collision probability meant that the concentration of HbCO was higher. In our labelling set-up, the factors to affect the labelling efficiency included the flow rate of ^{11}CO into the labelling vial (this affected the collision times per second), the concentration of red cells in the saline solution (this affected the total collision area), the temperature in this solution (this affected the solubility of ^{11}CO) and the pH value in the solution (this affected the dynamic activity of the red cells). In addition to these factors, because so much N_2 had been mixed with the ^{11}CO in the labelling system, it seriously reduced the SA value in the storage vial and seriously affected the labelling efficiency in the labelling vial. Therefore a powerful ^{11}CO trapping technique (we used only a simple storage vial) in the labelling system should be adopted in order to separate the carrier gas N_2. As mentioned in section 3.1.4, one can probably also consider a whole blood thin film exposed under the ^{11}CO gas with high SA. As no solution is used, this method may raise the collision probability. Since we were using a bubbling method to do the labelling, a high flow rate of ^{11}CO with high SA was always an ideal requirement. If the number of living red cells in the labelling saline solution can be controlled (and thereby the concentration), we can estimate how much activity in the storage vial should be reached (and thereby adjust the activity of the trapped ^{11}CO in the CPS). This can also benefit the following isolation for a single labelled red cell.

Likely methods of detecting the activity of labelled red cells in the labelling vial are proposed in section 3.2.3. By using an ionization chamber, a measured activity value for the labelled red cells was found at～30 µCi. In section 3.2.1, as the maximum activity we could receive in the storage vial was～1 mCi, the labelling efficiency can be found to be equal to 30 µCi/1 mCi～3% which was poor. Compared with the theoretical maximum activity of a single labelled red cell～15 µCi estimated in section 3.4.2, the activity of labelled red cells was apparently too low. However, as described in section 1.5, the experimental SA of produced ^{11}CO is normally less than 1% of 9200 Ci/µmole (theoretical SA of pure ^{11}CO). Hence the expected maximum activity of a labelled red cell should be equal only to～0.15 µCi. Based on the experimental activity of labelled red cells in our experiment～30 µCi, under the assumption of a perfect labelling of cells, one can divide 30 µCi by 0.15 µCi and acquire a number～200 which can probably define the average number of red cells in the solution. However in real experimental conditions, the number of red cells obviously greatly exceeds 200 (we did not investigate the concentration of red cells in the labelling vial due to the lack of instruments). In any case, using the PEPT technique, with some adjustments of energy windows and distance between the detectors, a tracer with an activity much less than 0.15 µCi can still be tracked despite the maximum velocity of a tracer needs to be much lower.

Figure 3.14 is the only preliminary visualized result from the test of this simple labelling set-up. The colour level of the image gives firm evidence that under this simple manual labelling set-up, the red cells absorbed the produced ^{11}CO. In section 3.3, several methods to isolate the labelled red cells are proposed as possible choices for future reference. A theoretical maximum activity of a single labelled red cell is estimated in section 3.4. This theoretical activity calculation of a single labelled red cell considers only the pure physical process. However in a biological system, conditions are not the same. Although Figure 3.14 provides encouraging evidence, this simple labelling set-up cannot provide any other quantitative analyses and therefore a sophisticated labelling system with some sensitive sensors should be developed in the future.

Chapter 4

Ideas related to tracking a single labelled RBC, discussion and suggestions for future work

If we can acquire a single labelled red cell with enough activity, the steps in the future should be to design and build an in vitro flow system for the single labelled red cell to flow in it. Here we should bear in mind that if we can simulate the in vitro conditions for a blood vessel as similar as possible, it would be beneficial for the labelled red cell. To understand some fundamental properties of the structure of the blood vessel and the physical and chemical phenomena of blood flow in the blood vessel would be helpful for the design and building of the simulated in vitro flow system. The way in which the blood flows in the blood vessels should be understood first.

To predict accurately how blood flows is not easy. The geometry of the arterial system is complex, with branches and bends which disturb the smoothly-flowing blood in the blood vessels. The wall of the artery can also become deformed by the force of the blood, which may in turn affect the flow inside the vessel. If we want to study the blood flow and blood vessels, Ultrasound and MRI are probably the most popular techniques. Ultrasound is used to monitor the bulk flow rate of blood flow while MRI (magnetic resonance imaging) has the power to offer a three-dimensional geometry of the vessels. Unfortunately for the study of complex flow patterns within the vessel, they cannot be observed by Ultrasound or MRI.

But, using the PEPT technique, we can understand the flowing roadmap for a single labelled red cell in the blood vessels and the velocity changes for a single labelled red cell at different positions in the circulation system. To understand the discrepancies in velocity can also help us sometimes determine where blood vessel disease is more likely, since disturbances in the blood flow can play an important role in the early stages of atherosclerosis.

In the future, if possible, we will try an in vitro test first. A pipeline system will be built to simulate the real blood flow. After the pipeline system becomes mature and the in vitro test can be verified as successful, we can begin to consider an in vivo test either in a small animal or in a human being. In order to simulate the blood flow in a human body, we need to understand several things about the circulation system, blood vessels and the blood itself.

4.1 The circulation system

The body's circulatory system has three distinct parts: pulmonary (lungs) circulation, coronary (heart) circulation, and systemic circulation (the rest of the system). The pumping action of the heart is similar to what happens when water is squirted out of a bottle which is held under water. When the bottle is squeezed, water is forced, or ejected, out of the bottle. When the bottle is allowed to re-expand, water is drawn back into it. This squeezing and expanding are what the heart does.

The atria contract and squeeze blood into the ventricles. The ventricles then contract and squeeze blood out of the heart. Each time the chambers of the heart contract, they then relax and expand while they fill with blood. This cycle of contraction and relaxation happens some 70+ times a minute, or about 104,000 times a day. Over the course of an average lifetime, the heart can beat up to 2.5 billion times. This is an amazing amount of work for such a small organ. On average, about 5 litres of blood are continually travelling through the circulatory system in the human body.

There are three varieties of blood vessel in the body: arteries, veins, and capillaries. The largest artery of the body is the aorta; the smallest arteries are called arterioles. The largest vein of the body is the vena cava; the smallest veins are called venules. In its circulation, the blood will flow through the heart, the aorta, the arteries, the arterioles, the capillaries, the venules, the veins, the vena cava and finally back to the heart.

4.1.1 The layers of a normal blood vessel

To simulate a normal blood vessel, we must first understand its structure. In the normal blood vessel, the intima is the innermost layer, which is in direct contact with the blood. It consists primarily of endothelium cells, which are very important in preventing thrombosis (blood clotting). In order to prevent thrombosis, these endothelium cells can produce specific substances which regulate the diameter of the blood vessels by acting on the underlying layer, which has a muscular structure called the media. The media is the middle layer of the blood vessel; consisting primarily of muscle cells. These muscle cells contract and relax in order to change the diameter of the blood vessels and to help control the blood flow and blood pressure. The adventitia is the outside layer of the blood vessel, and it is composed of loose connective tissue, which supports the other two inner layers. The role of the adventitia is purely mechanical. A schematic below (Figure 4.1) can help to realize the structure of blood vessels.

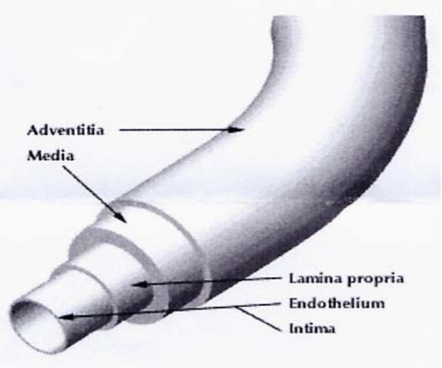

Figure 4.1: Layers of a normal blood vessel. Taken from [Mac88]

4.1.2 The size of blood vessels

Normally the sizes of arteries and veins are from 1 to 15 mm in diameter, the arterioles are from 20 to 50 µm in diameter, the venules are from 30 to 40 µm in diameter and the capillaries are from 5 to 10 µm in diameter. The diameter of a vertebral artery is normally from 2 to 3 mm, the diameter of the common carotid artery (adult) is about 6 mm and the diameter of the common carotid artery (newborn) is about 2.5 mm. Table 4.1 summarizes the average sizes of different blood vessels.

	Aorta	Artery	Arteriole	Vena cava	Vein	Venule	Capillary
size	25 mm	4 mm	30 µm	30 mm	5 mm	35 µm	6 µm

Table 4.1: Average sizes of blood vessels. Data from [Nic90]

4.1.3 Blood pressure

Blood pressure is the pressure of the blood flowing through the blood vessels against the vessel walls. It depends on the blood flow (how much blood is pumped by the heart) and the resistance of blood vessels to the blood flow. If the pressure is high, the heart must work much harder to maintain an adequate blood flow to the body. Figure 4.2 below indicates the different pressures in the different human blood vessels.

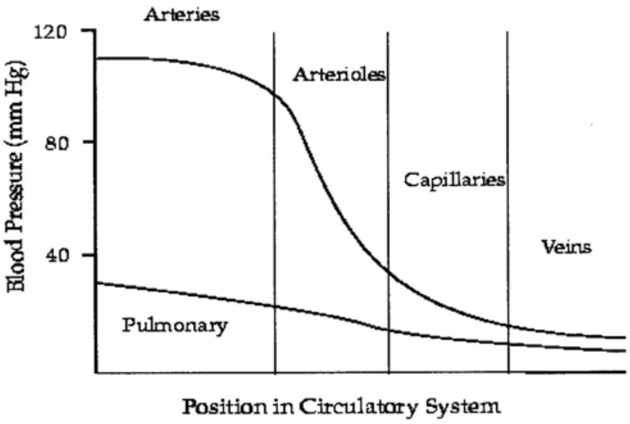

Figure 4.2: Blood pressure in circulatory system. Taken from [Nic90]

As mentioned above, the heart can beat more than 100,000 times a day. Each time it beats, a surge of blood is pumped from heart into arteries to increase the pressure in arteries. In between the heartbeats, the pressure in the arteries decreases. This is why blood pressure is normally reported as two numbers, for example, 120/80. The first higher number (systolic) is the pressure of the blood against the artery walls when the heart contracts (e.g.,120). The second lower number (diastolic) is the pressure of the blood against the artery walls when the heart relaxes between the heartbeats (e.g.,80).

4.1.4 Pulsatile flow

The pulsatile flow is a periodic, rhythmic change in blood-flow velocity over time, due to cardiac beating. Pulsatile flow is found in arteries and in veins close to the heart. In contrast to the laminar flow with a constant, smooth propagation, the pulsatile flow in arteries tends to be disturbed with a flattening of the velocity profile during the systole and a more parabolic velocity profile during the diastole.

4.1.5 Blood flow rate

A schematic (Figure 4.3) and the formulae (4.1~4.3) below describe the fluid flow in a simple pipe. The wall of the pipe is not at all flexible. A mass conservation law (4.1) is applied to this simplified pipe model. M_1 and M_2 mean the mass, A_1 and A_2 mean the cross-section, D means the fluid density, v_1 and v_2 mean the velocity and t means the time. The final formula (4.3) matches the common physical principle of physical systems. Formula (4.3) implies that the velocity of fluid in a pipe will increase if the cross-sectional area is constricted. However, this is unfortunately not the case in the human blood vessel.

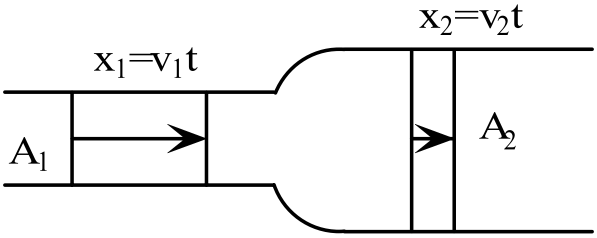

Figure 4.3: Fluid moving through a pipe.

$$M_1 = M_2 \tag{4.1}$$

$$DA_1v_1t = DA_2v_2t \tag{4.2}$$

$$A_1v_1 = A_2v_2 \tag{4.3}$$

Ideally blood would be better transported rapidly in large vessels and much more slowly in capillaries, but this runs counter to the flow principle above. In fact, the vertebrate blood system contains a preponderance of capillaries. That is, the total cross-sectional area in the capillary beds greatly exceeds the cross-sectional area at any other point in the system. It is for this reason that blood flows slowly through capillary beds. The speed of blood flow in the aorta is close to 30 cm/s while the speed of blood flow in a capillary is less than 1 cm/s.

How does the blood flow around the body? The blood flows through the blood vessels in the body because of pressure differences at different parts of the system. The rate of flow between any two points in the system is proportional to the pressure difference between these two points, and the direction of flow is always from the point of highest pressure to the point of lowest pressure. Darcy's law (4.4, below) is traditionally used to explain the reason for the flow of blood in the blood vessels. One can also insert the resistance R (formula (4.6)) into formula (4.4) and obtain the Hagen-Poiseuille law which is related to the voluminal laminar flow of incompressible uniform viscous liquid. This Hagen-Poiseuille law can be used as an approximate description of blood flow. Nevertheless, the Hagen-Poiseuille law is basically only accurate for Newtonian fluids (blood fluid is not a Newtonian fluid). Newtonian fluid is a fluid in which there is a linear relationship between the velocity gradient and the viscous force or the viscous shear stress. In other words, a Newtonian fluid has a constant viscosity at all shear rates at a constant temperature and pressure. Non-Newtonian fluids are fluids in which the viscosity changes with the applied shear force. Specifically, a non-Newtonian fluid may not have a well-defined viscosity.

$$Flow\ rate = K(P_1 - P_2) \tag{4.4}$$

$$K = \frac{1}{R} \tag{4.5}$$

$$R = \frac{8lu}{r^4 \pi} \tag{4.6}$$

In formula (4.4), P_1 and P_2 are two pressures of two points in the system, coefficient K is a proportionality constant that quantifies the efficiency with which the pressure difference is translated into fluid flow. K must be always less than 1. As we can see from formula (4.5), K is also a measure of the degree of resistance R (formula (4.6)) in the system. In formula (4.6), the parameter l means the length of the vessel, u means the fluid viscosity and r is the radius of the vessel. This resistance R is a function of the cross-sectional area of the vessel, the length of the vessel, the nature of the vessel wall (e.g., whether it is smooth) and the properties of the fluid moving through the vessel (especially the viscosity).

The blood fluid is not Newtonian and its flow can be described as laminar only in the smaller vessels; elsewhere it is turbulent. For this reason, the Hagen-Poiseuille law can only be an approximate description of the blood flow. From the measurements of Ultrasound, the blood flow rate through the internal carotid artery is about 180 ml/min and about 380 ml/min in the basilar artery. The hydrodynamics of blood flow in the blood vessels are complex and some critical questions still remain unresolved.

4.2 Computational Fluid dynamics (CFD)

Using CFD, a user can build a computational model which represents a system or device to be studied. CFD is the software to predict what will happen under a certain set of variations. The user provides a set of boundary conditions, and the software produces the user outcomes. Instantly, the user can predict how the experimental design will perform and test many variations until an optimal result is reached. All of this can be done before any physical experiments are performed. CFD software will provide users with images and data which predict the performance of an actual physical experiment.

For the purpose of this research, if the CFD software can be utilized to predict the flow condition of a single labelled red cell in the designed pipeline system, we can thereby build a virtual prototype on the computer for the pipeline system. After putting certain variations related to physical, biochemical and material parameters into this model, we can predict the performance of the flow system by the images and data obtained from the calculation of CFD. We can also improve the experimental design and operation by the prediction result of CFD. There are many phenomena that can be witnessed only through CFD and it offers researchers a deeper insight into their designs.

CFD has become an important tool in nearly every branch of fluid dynamics from the study of turbulence, multiphase flows and weather prediction to aerospace propulsion. By computational methods, the governing equations which describe fluid flow, such as the set of Navier-Stokes equations, continuity and conservation equations, can find numerical solutions through CFD. There are two benefits of using CFD. Firstly, we can model physical fluid phenomena which cannot be easily simulated or measured in physical experiments. Secondly, it allows us to investigate physical fluid systems more cost effectively and more rapidly than physical experimental procedures do.

4.3 In Vitro study

In in vitro study, a simple pipeline system will be designed to simulate the real blood vessels in a human body. As mentioned above, those concepts related to simulating real blood vessels in vitro must be noted when a pipeline system will be built. There are several considerations listed below for future in vitro tests: (1) The structure of the pipeline system. As we want only to make the labelled red cell flow successfully in the pipeline, it is not necessary to have a complex pipeline structure. A simple downstream structure is basically enough for our tests; (2) Similarity. The material used to form the pipeline should be as similar as possible to a blood vessel. If the red cell adheres easily to the inner surface of the pipeline, apparently this pipeline material being used is unsuitable. Silicon tubing is normally used to simulate blood vessels; (3) Parameters. When a red blood cell is flowing in the pipeline, we must make sure that the related physical parameters (temperature, pressure) in and surrounding the pipeline are similar to those for the blood vessel. A red blood cell can be alive and flow well in the pipeline if the inner and outer surroundings are similar to its former environment. The use of a suitable solution flowing in the pipeline should also be considered carefully. Saline solution is normally used as an alternative to blood; (4) The pump. Using a suitable pulsatile pump to drive the fluid in the pipeline and to control the velocity of the fluid is an important issue. Normally a commercial cardiovascular pump can be used to drive the fluid in the pipeline system. To put it simply, if the red blood cell can misread the pipeline as a real blood vessel in a human body, we have created in the pipeline system a suitable environment for this red cell.

4.3.1 The simulated pipeline system

We can simulate the blood flow in an arterial blood vessel in the human body. A simple flow system is designed conceptually below for tracking purposes.

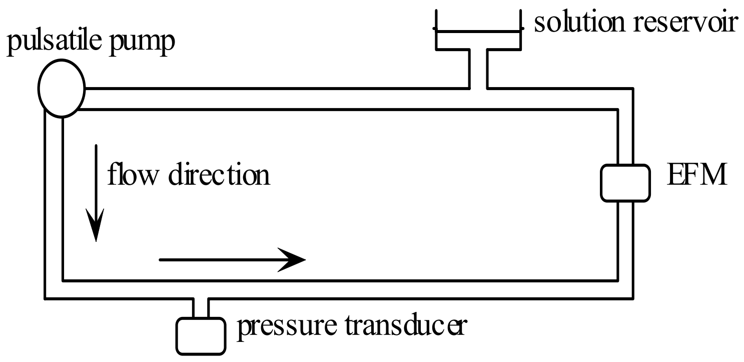

Figure 4.4: A simple flow system.

Figure 4.4 shows a simple conceptual design of a physiological blood flow circuit used to stimulate the pulsatile blood flow in an arterial blood vessel. As a conceptual design, a rectangular silicone tube whose bore can go down to 1 millimeter will be used to simulate an arterial blood vessel whose diameter is normally between 1 and 15 millimeters. A pulsatile syringe pump is used to generate pulsatile flow. By altering the pumping frequency, we can adjust the mean flow rate in the tubing. The pressure in the circuit is monitored using a pressure transducer. Physiological pressures are maintained by varying the height of the fluid reservoir. For the fluid used in the tubing, we can use saline, artificial blood or real blood. Using the electromagnetic flow meter (EFM), we can measure the precise instantaneous and mean flow rate. The EFM can provide the standard measurement of the flow rate which can be compared with the measured result from the PEPT technique. The single labelled red blood cell whose average size is nearly 7.7 µm can be injected into the system from the solution reservoir using the injection syringe.

4.3.2 Tracking

After obtaining a single labelled red blood cell with enough activity and building up a suitable pipeline system, this in vitro test will have the following experimental process: (1) The pipeline system will be set up between the two detectors of the ADAC Forte PET camera. The tracer’s course in the pipeline system must be confined within the field of view to make sure that the PET camera can detect most gamma-rays from the tracer. (2) The test should be repeated and tried with different experimental parameters, such as different fluid speeds, different tracer activities or different geometries of camera. (3) The experimental data can be received from the tracking program under UNIX. Using the tracking program, we can find the tracer's time-position relationship in the pipeline system. By comparing the data from each test, we can find an optimal set of parameters for the tracking process and eventually can track the single labelled red cell successfully.

4.4 Discussion and suggestions for future work

Due to the limited capability of our pumping system (0.1 mbar) and the poor pressure meter used (a few mbar), we cannot ensure the precise vacuum level in the target, in the CPS system and in the labelling system. We can only extend the pumping time and avoid all possible leakages in the whole process. A highly powerful pumping system and a highly sensitive pressure meter are crucial in future experiments in order to decrease the contamination from CO_2, CO and other chemical forms originally existing in the system.

The CPS system was basically stable. Nevertheless we did not investigate the conversion efficiency of zinc powder in the oven for reducing $^{11}CO_2$ to ^{11}CO and the absorption efficiency of NaOH for unconverted $^{11}CO_2$. The references [Roe04], [Zei97] in section 2.3.6 provide other and better reduction methods for reducing $^{11}CO_2$ to ^{11}CO. Due to the experimental limitations in situ, we did not measure the activity of trapped $^{11}CO_2$ (a spiral stainless steel in LN_2) and the trapped ^{11}CO (in an unsuitable aluminum reservoir). However, a theoretical estimation for the activity and production yield of the produced $^{11}CO_2$ in the target has been given in sections 2.1.6 and 2.3.3.

The trapping techniques for $^{11}CO_2$ and ^{11}CO were important. As mentioned in section 2.3.4, in the reference [Moc95], a solid-phase reversible method was employed to provide a trapping efficiency of more than 99% for the produced $^{11}CO_2$. And as described in section 2.3.6, in the reference [Zei97], a silica trap cooled with liquid argon was employed to trap the ^{11}CO, while in the reference [Hos02], a carbon molecular sieves cooled with a dry ice/isopropanol bath was employed to trap the ^{11}CO. A higher trapping efficiency can reach a higher concentration of the final product. The above-mentioned methods to trap the $^{11}CO_2$ and ^{11}CO are suitable for future reference.

We encountered many problems with the storage, activity measurement, purity investigation and transportation of ^{11}CO in situ. The problem with the storage of ^{11}CO was that some ^{11}CO molecules can be deposited on the inner surface of this aluminum reservoir and thereby reduce the useful produced activity. Furthermore, the size of the aluminum reservoir which we used was so big that many uncertainties in situ were created in measuring the activity directly by using a scintillation detector. A better way of avoiding this problem is to use a small silica trap which can be inserted into an ionization chamber. To calculate the SA value, one can release the ^{11}CO gas from the small silica trap (which is removed from the liquid argon) into an evacuated vial of known volume. Due to the trapping problems with ^{11}CO (no suitable trapping technique for ^{11}CO was used) and the lack of a radio-GC, I was not able to investigate the purity of produced ^{11}CO and to measure specific activity ($^{11}C/^{12}C$ ratio). However, as mentioned in section 2.4.6, in other work [Zei97], researchers reached the specific activity～15 Ci/μmole for $^{11}CO_2$ and～8 Ci/μmole for ^{11}CO. The purity of produced ^{11}CO in their work was found to be～0.09%. The carrier gas used to promote the flow of ^{11}CO into the labelling system was justified but the timing for using the carrier gas (N_2) was still not resolved. Following all the problems with the ^{11}CO production, the maximum activity to be found from the storage vial of ^{11}CO in the labelling system (the storage vial was inserted into the ionization chamber) was 1 mCi and the SA value was found to be equal to～0.714 μCi/μmole. However as the labelling system did not function to separate the carrier gas from the transported ^{11}CO, a great deal of N_2 was mixed with the ^{11}CO in the storage vial, making the estimated SA value lose accuracy.

Dr. David Parker and I built only a simple manual labelling set-up which can be regarded as a preliminary prototype (please see section 3.2.1). In section 3.2.3, a measured activity value for the labelled red cells was found of～30 μCi. Compared with the theoretical maximum activity of a single labelled red cell～15 μCi estimated in section 3.4.2, apparently the activity of labelled red cells was too low. In section 3.2.1, as the maximum activity we could receive in the storage vial was～1 mCi, the labelling efficiency can be found to be equal to 30 μCi/1 mCi～3%, which was poor. However as described in section 3.2.2, if some factors which influenced the labelling process could be improved, the labelling efficiency should increase. An image shown in Figure 3.14 represents only the preliminary result that some ^{11}CO gas had been absorbed into the red cells. This preliminary labelling set-up only served to investigate the possibility of labelling red cells under our practical apparatus. It was difficult to make other quantitative analyses with this simple manual set-up. A novel and sophisticated labelling system with some sensitive sensors should be developed in the future. For the isolation of red cells, the whole description in section 3.3 is only conceptual as no related instruments can be used in situ.

As mentioned in section 3.4.2, if all the bonding sites contain ^{11}C in a red cell, a theoretical maximum activity～15 μCi can be reached. However this maximum would require an SA of 9200 Ci/μmole (theoretical SA of pure ^{11}CO) and perfect labelling of the cell. As described in section 1.5, the experimental SA of produced ^{11}CO is normally less than 1% of 9200 Ci/μmole based on the measurements from other research groups. With the low SA of produced ^{11}CO, the expected maximum activity of a labelled red cell should be equal to only 15 μCi × 1%～0.15 μCi. Assume we acquired a SA value for the produced ^{11}CO～18 Ci/μmole. Given perfect labelling, this would give (18/9200)x15 μCi～30 nCi, which was the expected maximum activity of a labelled red cell. Under the current PEPT technique, a tracer with 0.3 mCi can normally give approximately 13000 events per second. Hence a tracer with 30 nCi can give

$13000\times(30\times10^{-9})/(0.3\times10^{-3})\sim1.3$ events per second from the ADAC Forte. However by adjusting the energy windows and the distance of the detectors, we might increase this to 20 events per second which should still be able to track a labelled red cell with a maximum velocity of 0.3 cm/s. ($v\sim(\sigma fR)/b^{3/2}$ in section 1.2.2)(in a capillary, the blood speed is less than 1 cm/s)

I began working for a PhD in April 2002. Due to the influence of the building of the MC40 cyclotron from 2002 to 2004 at Birmingham, this study was delayed. I had leave of absence from June 2005 until 1st January 2006. I chose also to change my student registration status from PhD to MPhil on 1st January 2006. From my point of view, this feasibility study needs a long period of experimental work (at least two years) in order to set up the related techniques and gain some meaningful and reliable data. But because only a short period of experimental work was done, there is not much measurement data shown in this study. In it, I concentrated on testing the target chamber and the CPS system. I did not try to maximize the yield in the target because we already had plenty of activity in the aluminum reservoir (of trapped ^{11}CO) for the following trials. It appears to have been converted efficiently to ^{11}CO (although the conversion efficiency was only 50% [Iwa81]) and the trapping was also efficient (although the trapping method used for ^{11}CO was unsuitable.). I had run first attempts at labelling red cells. Figure 3.14 also shows some success in getting RBC to absorb ^{11}CO.

On the basis of this original research work, I would like to suggest that in future experiments one should try to improve the ^{11}CO production system, including the vacuum level in the whole system, the method for reducing $^{11}CO_2$ to ^{11}CO, the trapping techniques for $^{11}CO_2$ and ^{11}CO and a sophisticated instrument be obtained for purity investigation. If the SA of the produced ^{11}CO can be raised, then in theory a labelled red cell with a higher activity can be reached as well. One should also try to create an effective labelling method with a high labelling efficiency and try to find a suitable isolation technique. If the CFD can be utilized in the future, it can reveal some important information on the design of an in vitro blood flow system and on the fluid flow within it. I hope that this feasibility study will be of use to someone who wants to focus on this issue.

References

[Ash97] Arthur Ashkin, Proc. Natl. Acad. Sci. USA, Vol.94, pp.4853-4860, May 1997 Physics

[Bar96] G. Barbiellini, M. De Denaro, L. Gregori, S. Pieczuro,G. Tromba and A. Rindi, Nucl. Instru. Meth. Phys. Res., A373, pp.165-167, 1996

[Bid80] G. T. Bida, T. J. Ruth, A. P. Wolf, Radiochimica Acta, Vol.27, pp.181-185, 1980

[Boh06] http://www2.austin.cc.tx.us/%7Eemeyerth/bohr.htm

[Bre03] Cornelia Brehmer, Peter X. Iten, Forensic Science International, Vol.133, pp.179-181, 2003

[Cas78] V. R. Casella, D. R. Christman, T. Ido, A. P. Wolf, Radiochimica Acta, Vol.25, pp.17-20, 1978

[Cla75] J. C. Clark, P. D. Buckingham, Short-lived Radioactive Gases for Clinical use, Butterworths, USA, 1975

[Das94] Ashok Das, Thomas Ferbel, Introduction to Nuclear and Particle Physics, John Wiley & Sons, Inc., 1994

[Dam94] J. Van Dam, P. Daenens, J. Forensic Sci., Vol.39, pp.473-478, 1994

[Eij02] Carel W E van Eijk, Phys. Med. Biol., Vol.47, R85-R106, 2002

[Ery02] http://www.tau.ac.il/~inter05/eryt.htm,2002

[Fan06] X. Fan, David Parker, M. D. Smith, Nucl. Instru. Meth. Phys. Res., A558, pp.542-546, 2006

[For64] R. E. Forster, Handbook of Physiology. Section 3: Respiration, pp.827-837, 1964

[Fre98] Robert A. Freitas Jr., Artificial Cells, Blood Substitutes, and Immobil. Biotech. Vol.26,pp.411-430,1998

[Frö00] Jürgen Fröhlich, Helmut König, FEMS Microbiology Reviews, Vol.24, pp.567-572, 2000

[Glo02] http://metallo.scripps.edu/PROMISE/GLOBINS.html, 2002

[Hes87] Sven-Johan Heselius, Petter Malmborg, Olof Solin, Bengt Långstrôm, Appl. Radiat. Isot., Vol.38, pp.49-57, 1987

[Hos02] Eric D. Hostetler and H. Donald Burns, Nucl. Med. Bio., Vol.29, pp.845-848, 2002

[Hug03] J. M. B. Hughes, D. V. Bates, Respiratory Physiology & Neurobiology,Vol.138, pp.115-142, 2003

[Hug99] Michael Pycraft Hughes, Seventh Foresight Conference on Molecular Nanotechnology, 1999

[Iwa81] Ren Iwata, Tatsuo Ido, RADIOISOTOPES, Vol.30, pp.28-30, 1981

[Jac74] W. W. Jacobs, D. Bodansky, D. Chamberlin, D. L. Oberg, Physical Review C, Vol.9, No.6, 1974

[Kar88] Joel S. Karp, David A. Mankoff and Gerd Muehllehner, Nucl. Instru. Meth. Phys. Res., A273, pp. 891-897, 1988

[Kno00] Glenn Knoll, Radiation Detection and Measurement 3^{rd} Edition, John Wiley and Sons, 2000

[Lap03] S. Lapi, T. J. Ruth,A. Zyuzin,J. M. Dauria, Nucl. Instru. Meth. Phys. Res.,B204,pp.444-446,2003

[Led05] K. W. D. Ledingham, Nuclear Physics A, Vol.752, pp.633-644, 2005

[Mac88] Raymund Machovich, Blood Vessel Wall and Thrombosis: Vol.1, CRC Press, 1988

[Mae62] A. C. Maehly, Methods of Forensic Science, Vol.1, pp.539-593, 1962.

[Moc95] Bruce H. Mock, Michael T. Vavrek and G. Keith Mulholland, Nucl.Med.Bio.,Vol.22, pp.667-670, 1995

[Nap03] J. Nappi, Am. J. Health Syst. Pharm., Vol.60, S4-S8, 2003

[Nic04] Nichiporov D, Luckjashin V, Kostjuchenko V, Appl. Radiat. Isot., Vol.60, pp.703-716 , 2004

[Nic90] Wilmer W Nicholas, Michael F O'Rourke, Donald A McDonald**,** McDonald's Blood Flow in Arteries: theoretic, experimental, and clinical principles, Philadelphia: Lea & Febiger, 1990

[Noz81] T. Nozaki, M. Iwamoto, Radiochimica Acta, Vol.29, pp.57-59, 1981

[Par02] D. J. Parker, R. N. Forster, P. Fowles, P. S. Takhar, Nucl. Instru. Meth. Phys. Res., A477, pp.540-545, 2002

[Par93] D.J. Parker, C.J. Broadbent, P. Fowles, M.R. Hawkesworth and P.A. McNeil, Nucl. Instr.and Meth. A 326, Vol.592, 1993

[Pow03] J. Powell, J. P. ỚNeil, Joseph Cerny, Nucl. Instru. Meth. Phys. Res., B204, pp.440-443, 2003

[Pow00] J. Powell, R. Joosten, C. A. Donahue, etc., Nucl. Instru. Meth. Phys. Res.,A455, pp.452-459, 2000

[Pro02] http://metallo.scripps.edu/PROMISE/1BBB.html, 2002

[Ree92] Robert Blake Reeves and Hae Kun Park, Respiration Physiology, Vol.88, pp.1-21, 1992

[Roe04] Dirk Roeda, Christian Crouzel, Frédéric Dollé, Radiochimica Acta, Vol.92, pp.329-332, 2004

[Saj86] M. Sajjad, R. M. Lambrecht, A. P. Wolf, Radiochimica Acta, Vol.39, pp.165-168, 1986

[Sti03] Monika Stich,Stefan Thalhammer,Renate Burgemeister,Gabriele Friedemann,Susanne Ehnle, Carsten Lüthy, Karin Schütze, Pathol. Res. Pract., Vol.199, pp.405-409, 2003

[Van83] T. Vandewalle, C. Vandecasteele, Int. J. Appl. Radiat. Isot., Vol.34, pp.1459-1464, 1983

[Wah02] R. L. Wahl, J. W. Buchanan, Principles and Practice of Positron Emission Tomography, Lippincott Williams and Wilkins, 2002

[Wei74] M. Weissbluth, Hemoglobin: Cooperativity and Electronic Properties, Springer-Verlag, 1974

[Wol52] L. Wolfenstein and D. G. Ravenhall, Phys. Rev., Vol.88, pp.279-282, 1952

[Yuk98] N. Yukawa, T. Suzuoka, T. Saito, A. R. W. Forrest,M. Osawa, S. Takeichi, Forensic Sci. Int.,Vol. 94, pp.211-215, 1998

[Zei97] S. K. Zeisler, M. Nader, A. Theobald and F. Oberdorfer, Appl. Radiat. Isot., Vol.48, pp.1091-1095, 1997

[Zie85] J. F. Ziegler , J. P. Biersack and U. Littmark,The Stopping and Range of Ions in Solids, ISBN: 008021603X, Pergamon Press, New York, 1985

[Zij91] W. G. Zijlstra, A. Buursma and W. P. Meeuwsen-van der Roest, Clin. Chem.,Vol.37, 38, 1991